Universidade do Minho
Escola de Engenharia

Konrad Józef Krakowiak

Assessment of the mechanical microstructure of masonry clay brick by nanoindentation

Março de 2011

Assessment of the mechanical microstructure of masonry clay brick by nanoindentation
Konrad Józef Krakowiak
UMinho | 2011

Universidade do Minho
Escola de Engenharia

Konrad Józef Krakowiak

Assessment of the mechanical microstructure of masonry clay brick by nanoindentation

Tese de Doutoramento em Engenharia Civil

Trabalho efectuado sob a orientação de
Professor Doutor Paulo B. Lourenço,
Universidade do Minho
Professor Doutor Franz-Josef Ulm,
Massachusetts Institute of Technology

Março de 2011

Acknowledgements

The research reported in this thesis has been carried out at the Civil Engineering Department of University of Minho, Portugal, and at the Civil and Environmental Engineering Department of Massachusetts Institute of Technology, United States. This research was supported by the Portuguese Foundation for Science and Technology (FCT) under grant SFRH/BD/39232/2007, since October 2007.

I would like to express my deepest gratitude to my supervisor Prof. Paulo Lourenço for his guidance and patience along these years. Since the first time we met, back in 2003 as a student of Erasmus-Socrates program, he has provided continuous support of my ideas and development. Also, I would like to thank to Prof. Franz-Josef Ulm for the warm welcome in his research group as well as valuable and challenging discussions.

I am also grateful to Prof. Robert Gajewski of Warsaw University of Technology and Prof. Júlia Lourenço University of Minho, who has given me the first opportunity to study abroad during my Master Course and supported me also during the doctoral course.

I would like to give special thanks to Dr. J. P. Castro Gomes, Centre of Materials and Building Technologies (C-MADE), University of Beira Interior for making feasible the Mercury Intrusion measurements, as well as Dr. G. P. Souza for helpful guidance and advices which helped me in better understanding the complex world of ceramics. Part of this work could not be achieved without the help of Dr. Nicholas Randal from CSM Instruments and Dr. Matthieu Vandamme from Université Paris-Est, École des Ponts ParisTech–UR Navier, who have provided the naval brass data set reported in Chapter IV. Additionally, I would like to acknowledge the help of my colleagues Dr. Luca Sorelli and Dr. Alberto Ortega for valuable discussions.

Finally, I would like to dedicate this work to all my family, for their support, especially to my wife Joanna, who has provided as much work as I did for this thesis to be finished, being continuous support for our children and family life in my absence.

Abstract

The work presented in this thesis aims to implement the recent advances in the material science into the field of structural clay products applied to masonry constructions. The experimental analysis carried out by the author is focused on the detailed description of the heterogeneous microstructure of the fired clay brick, as a function of its composition and processing conditions. Multi-field methods of investigation have been combined, from standard mechanical tests carried out on bulk material on the macro-scale to novel nanoindentation techniques, which infers the mechanical properties of the solids on the nano- and micro-scales. Moreover, the complex interplay between the different components of this heterogeneous solid is traced with Scanning Electron Microscopy methods or Mercury Intrusion Porosimetry. The existing hierarchical ordering of fired brick microstructure is framed in the multi-level model, where the building blocks are classified and described with reference to the type of morphology present and mechanical characteristics.

The statistical indentation method, originally developed for cement based materials is extended to the field of structural ceramics. Such an experimental analysis of mechanical phase properties is carried out with the aid of Gaussian Mixture Modeling, which together with Maximum Likelihood concept and Expectation-Maximization algorithm, provides a robust and efficient deconvolution strategy. This deconvolution technique is validated on Ordinary Portland Cement, brass alloy and investigated fired brick. The relation between the characteristic scale of depth-sensing measurement and the mechanical characteristics inferred from the bulk of composite material is presented. Additionally, Buckle's rule-of-thumb is approached with a probabilistic model of biphasic composite materials, which represent idealized microstructures.

The mechanical properties of the 'glassy' matrix of the fired brick are investigated in the depth-sensing experiment. Different regimes of the indentation force are considered along the experimental campaign. The relation between the morphology of the 'glassy' matrix, its composition and measured indentation modulus, elastic modulus and indentation hardness is studied. Additionally, the composite 'polycrystalline-amorphous' nature of the matrix of the brick is corroborated and documented in detail. Mechanical properties of other mechanically active phases incorporated within the microstructure of the fired clay brick e.g. quartz, rutile etc. are assessed and reported.

Resumo

O trabalho apresentado nesta tese tem como objectivo a aplicação dos avanços recentes na ciência dos materiais aos produtos cerâmicos estruturais usados nas construções de alvenaria. A análise experimental realizada pelo autor está focada na descrição detalhada da microestrutura heterogénea do tijolo de barro cozido, em função da sua composição e condições de processamento. Foram combinados métodos de investigação multi-campo, desde ensaios mecânicos padrão realizados no material ao nível da macro-escala, até novas técnicas de nano-indentação que inferem as propriedades mecânicas dos sólidos ao nível das escalas nano e micro. Adicionalmente, a complexa interacção entre as diferentes componentes deste sólido heterogéneo é caracterizada com recurso aos métodos de Microscopia Electrónica de Varrimento ou Porosimetria por Intrusão de Mercúrio. O ordenamento hierárquico da microestrutura existente nos tijolos cozidos é enquadrado num modelo multi-nível, onde os elementos são classificados e descritos com referência ao tipo de morfologia presente e às características mecânicas.

O método de indentação estatística, originalmente desenvolvido para materiais cimentícios, é alargado ao campo da cerâmica estrutural. Esta análise experimental das propriedades mecânicas da fase é realizada com o auxílio de um Modelo de Mistura de Gauss que, juntamente com os conceitos de máxima verosimilhança e algoritmo de Maximização da Expectativa, fornece uma estratégia de deconvolução robusta e eficiente. Esta técnica de deconvolução é validada em Cimento Portland corrente, em liga de latão e nos tijolos cozidos investigados. É apresentada a relação entre a escala característica na medição da profundidade e as características mecânicas inferidas a partir da massa de material compósito. Adicionalmente, a regra empírica de Buckle é abordada com um modelo probabilístico de materiais compósitos bifásicos, que inclui microestruturas idealizadas.

As propriedades mecânicas da matriz ‘vítrea’ do tijolo cozido são investigadas no ensaio com medição da profundidade. Consideram-se diferentes regimes da força de indentação ao longo da campanha experimental. É estudada a relação entre a morfologia da matriz ‘vítrea’, composição e módulo de indentação medido, módulo elástico e dureza de indentação. Adicionalmente, a natureza do compósito ‘policristalino-amorfo’ da matriz do tijolo é corroborada e documentada em detalhe. As propriedades mecânicas das outras fases mecanicamente activas incorporados na microestrutura do tijolo de barro cozido, por exemplo quartzo e rútilo, são avaliadas e descritas.

Contents

I. Introduction

I.1. GENERAL CONTEXT

The development of mankind and growth of civilization have been closely tied to man's ability to make use of materials. This history began with wood in a distant past continued with stone, and around 24,000 years ago ceramics were introduced.[1] Since then, mankind had the ability to transform the plastic mass of clay into a stiff and durable solid. The first ceramic crafts were simple objects such as figures (22,000 BC, Moravia, Czech Republic)[1] or primitive earthenware used in the daily tasks. However, the need of a secure shelter, able to protect Man against attacks and climate, has driven him to apply fired clay as a construction material. The oldest fired bricks used for housing have been found in Knossos (Crete) and dated back to around 4300 BC.[1] The potential of ceramics used as a construction material has been appreciated ever since remote ages.

Nowadays, fired clay brick is a commonly used material, which together with cement or lime mortar makes masonry load bearing walls, pillars, infill panels and so on. Fired brick possesses several important characteristics, which have made it attractive in the construction of housing and other structures. Brick can be crafted as a durable solid, with high stiffness and load bearing capacity, and is able to sustain severe thermal and environmental conditions, while providing good sound and heat isolation properties, not mentioning the architectural aesthetics. However, the way in which the brick material performs is governed by its composition and internal microstructure.

From this point of view, fired clay ceramics belong to the group of composite materials, which possess a high level of heterogeneity with hierarchical ordering of the microstructure. The most prominent feature of such material system is the microstructural disorder, reflected in the spatial variability of the composition, in diverse properties and geometrical forms of the incorporated solid phases[2,3] as well as in inherently porosity. It is the microstructural disorder which ultimately defines the macroscopic properties.

Such a feature allows the brick to exhibit its attractive properties, but also leads to a significant scatter and uncertainty in properties, such as the elasticity modulus, the compressive strength or the irreversible expansion. Structural design rules, as an example, account for the variability of properties using characteristic values and a partial safety factor. The recent developments in materials science aim at a better understanding of the interplay between factors like composition of the material, processing of the material and its properties. Progress in experimental analysis and analytical tools has driven material engineers towards a better representation of the microstructure at multiple length scales.[4,5] Such advances refer to the direct observation of the material morphology as well as the quantification of mechanical properties at different length scales. The effect of material heterogeneity and the material constituents on the overall brick performance at the macro-scale may be traced, what opens venues in the optimization of the material performance and in tailoring its properties to special requirements.

This thesis follows this recent approach and contributes to the implementation of material science paradigm into the field of structural masonry. Recent developments, originally from the science of cement based materials, are transferred to the field of building ceramics and applied to study the fundamental blocks of fired clay brick material. The hierarchical ordering of brick microstructure is described and arranged in a comprehensive multi-scale model. The link between composition, processing and properties is inferred and quantified at the sub-micron scale from nanoindentation experiments. The intrinsic mechanical properties of the brick constituents are measured and linked to the local morphology and composition. The work presented here also produces advances in understanding statistical indentation techniques, which represent novel and promising methods for inferring the mechanical phase properties in multi-component materials at different length scales.

I.2. INDUSTRIAL CONTEXT AND RESEARCH MOTIVATION

Next to concrete and steel, clay brick is the most used construction material on our planet. During the last decade the world-wide clay brick production per annum has stand at 24 billion units in Europe, 218 billion in Asia, 9 billion in North America and 5 billion in Africa, South America and Oceania (see Figure I.1(a-b)).[6,7] This ubiquitous presence of masonry brick comes at a non-negligible price for the environment, because significant amounts of carbon dioxide (CO_2) are released into the atmosphere at the production stage. Approximately 0.25 tons of carbon dioxide is released per each ton of structural clay products.[8,9,10] More than

90 % of this amount originates from combustion of fossil fuels, e.g. natural gas or petroleum coke, in the kiln during the thermal treatment of the green ware. Obviously, this also means that only one-tenth of the CO_2 emission comes from other sub-processes. The CO_2 emission for clay brick is only a quarter of the emission in Portland cement production, as one ton of cement produces one ton of carbon dioxide.[11] However, comparing with concrete, which incorporates up to 15 % of cement (1 ton of cement ≈ 8 tons of concrete), the environmental footprint of fired clay brick is almost the double.

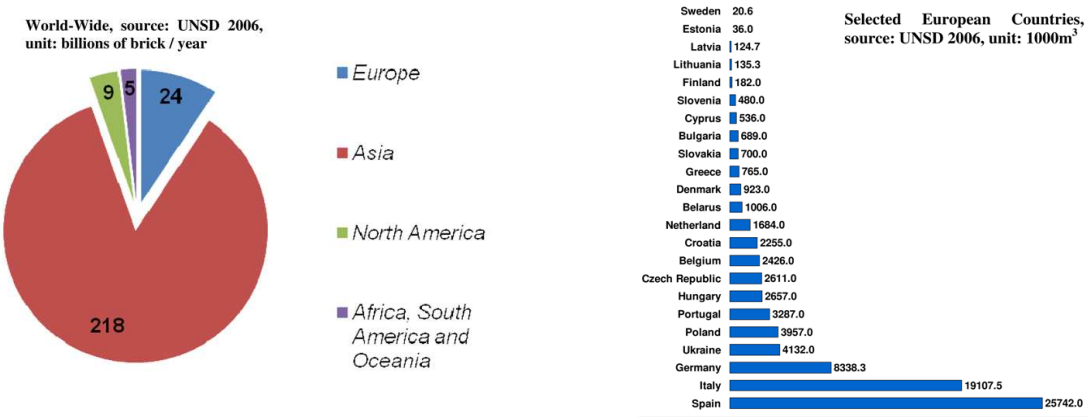

(a) (b)

Figure I.1 Annual production of fired clay brick: a) world-wide brick production (2004) (billions of units), b) brick production in selected European countries (2006), according to United Nations[6] and European Commission statistics[7].

This ecological burden is more pronounced in the present time, when construction materials must conform to higher requirements while satisfying a growing world-wide consumption. In the recent years, the construction industry worldwide has grown steadily, while masonry (either structurally or non-structurally) remains a much used material. The growing requirements of material sustainability, energy efficiency and recyclability (Figure I.2) call for new developments in the field of brick material science. Such developments refer to our understanding of the complex interplay between the composition, processing, microstructure and the properties of the fired brick and masonry construction.

The key challenge for the future appears to be the reduction of the ecological burden of the brick without compromising its properties, such as strength, durability, solidity, fire protection and low maintenance.

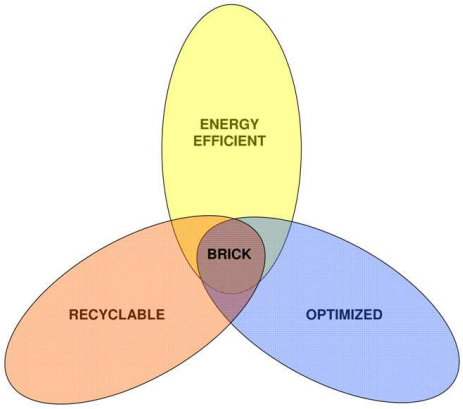

Figure I.2 Schematic representation of the concept of modern building brick and structural ceramics as an energy efficient, optimized and recyclable construction material.

I.3. PROBLEM STATEMENT AND ADOPTED APPROACH

Structural clay products, like brick, represent a complex man-made ceramic material system created upon heating a mixture of clay minerals, filler and flux. For a temperature above the melting temperature of the clay minerals and the flux component ≈950 [°C] a viscous fluid develops leading to consolidation of the green ware.[2] Such a fluid phase may be a mixture of all elements present in the parent materials, however its core is build up from the oxygen, silicon and aluminum. These chemical elements are the principal components of the 'liquid bond', next to alkaline elements like potassium, sodium and other accessories provided by the feldspar flux or present as impurities in the raw materials. The multi-component nature of the melt, together with the heat energy, provides environment and conditions for the crystallization of new phases with different lattice systems and geometrical forms.[3] Upon cooling below the glass transition temperature, the melt solidifies to form a polycrystalline-amorphous matrix ('glassy' phase) of the brick, with high degree of heterogeneity. The 'glassy' phase, which may account for more than half of the total mass of the fired brick,[3,12] provides the bond for the coarse and fine aggregates, and together with the porosity constitute the complex microstructure of a fired clay brick with specific mechanical and physical properties.

This brief description shows in a qualitative way the transformation from the raw materials, via processing, to the final microstructure of the fired brick. The composition-processing-property link is evident (see Figure I.3). Although much has been done in the last decades in the field of ceramics, the conceptual theoretical and experimental framework for

modeling the mechanical properties of structural ceramics, such as brick, has not yet been developed. The lack of such a concept may be attributed to the complexity of this material, as well as to the belief that ‘traditional’ ceramics can be crafted according to generally accepted empirical rules, with no need for advancement and progress in production. In addition, the developments in the science of cement based materials and in design rules for concrete structures effectively replaced masonry as a structural material in many developed countries and hindered innovative applications in the field. Therefore, this work aims at filling an existing gap in masonry science and at implementing the materials science paradigm into the masonry field.

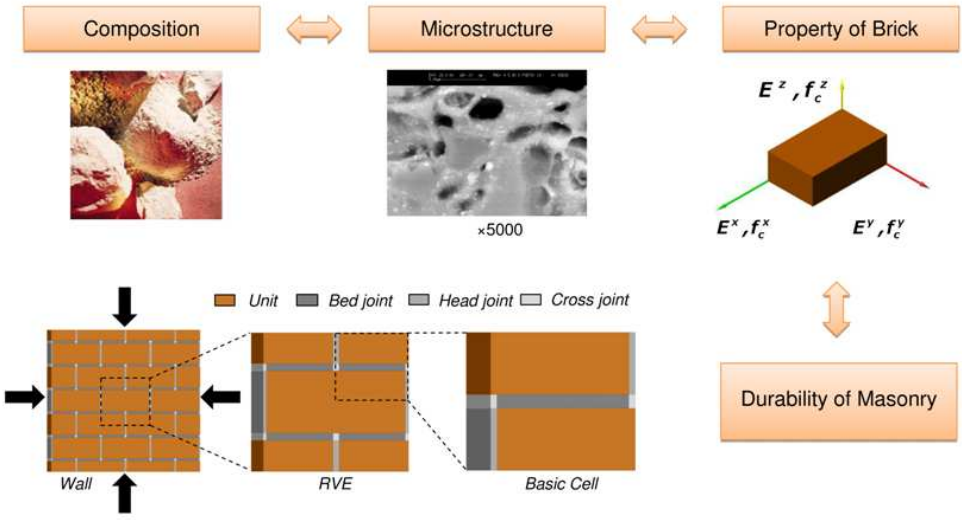

Figure I.3 Implementation of the material science paradigm into the masonry field, the composition-processing-properties link foreseen in the development of sustainable masonry.

The adopted approach includes a combination of experimental investigations and theoretical modeling. The approach is targeted on the detailed description of the brick microstructure at different length scales of observation, starting from ‘nano-scale’, the most basic blocks relevant for brick performance, and concluding at the structural scale of day-to-day applications, namely ‘meso-scale’. Such description identifies the building blocks of the structural ceramics, in the framework of a comprehensive ‘multi-scale’ model, and links the origin of the building blocks to the composition and processing technology of brick. Multi-field techniques are applied, from standard well know tests in the field of material characterization to advanced novel methods at sub-micron scales, where the bulk is constrained in much smaller volumes.

I.4. RESEARCH OBJECTIVES

The approach presented here studies the effect of the composition, processing conditions and microstructural details on the mechanical performance of fired clay bricks used in masonry. A series of objectives is set forth in order to tackle this scientific problem. These objectives are summarized below:

- Objective 1: *Develop a hierarchical model of fired clay brick microstructure, which allows to pin down the effect of composition and processing on the macroscopic performance of brick.* The thermal treatment of the raw mixture of clay, filler and flux provides the fired brick microstructure with large variety, which affects its overall performance. Depending on the temperature applied in the firing stage, as well as the composition and processing, the neo-crystal phases and porosity appear at different material levels with characteristic scales spanning over several orders of magnitude. Therefore, a detailed description of masonry brick within the framework of the multi-scale model allows one to trace the origin of its mechanical performance, and relate it with the green and fired ware composition as well as the manufacturing technology.
- Objective 2: *Extension and validation of the Statistical Grid Indentation (SGI) technique applied to heterogeneous materials with hierarchical ordering of the microstructure.* The current developments in the SGI methods originate from the implementation of nano-technology into the cement-based materials science. SGI provides the experimentalists with the access to the bulk properties at the nano-scale, where the ordinary methods of mechanical testing no longer apply. However, in order to infer the relevant mechanical properties of the phases stochastically distributed in the bulk volume of the multi-phase material, like fired clay brick, multiple depth-sensing experiments must be conducted on the material surface. Therefore, an adequate statistical approach is required in order to give the proper interpretation of the acquired records, to estimate the confidence level of the measured properties and to relate the observations to the local chemical and mineralogical composition.
- Objective 3: *Study of the mechanical performance of the 'glassy' matrix, the principal load bearing phase within the microstructure of the brick.* The composite nature of the 'glassy' bond existing in the structural ceramics is well known. However, the exact mechanical properties of the 'glassy' matrix, as well as the effect of the composition

on its performance, are still essentially unknown. Due to the sub-micron characteristic scale of its bulk and complex distribution over the brick volume, the stiffness and strength cannot be assessed with standard methods of material testing. The nanoindentation method combined with refined statistical tools overcomes this problem and allows to infer *in-situ* the mechanical characteristics of 'glassy' matrix from direct tests at sub-micron scale.

It is hoped, that the answers to the three objectives above are a good step forward to the development of sustainable masonry, with properties tailored to societal needs and environmental requirements.

I.5. THESIS OUTLINE

The structure of the thesis consists of six main parts. In the first part, Chapter I, a general introduction is made, including setting forth the research motivation and objectives. The second part of the thesis, Chapter II, deals with an experimental approach towards the development of the hierarchical model of the brick microstructure. This chapter presents a variety of advanced techniques of experimental mechanics and material characterization applied to extruded clay brick. The outcome of Scanning Electron Microscopy (SEM) coupled with Energy-dispersive X–ray Spectroscopy (EDX), Mercury Intrusion Porosimetry (MIP), preliminary Instrumented Nanoindentation tests and macroscopic strength and durability tests are summarized in a comprehensive 'multi-scale' description of the brick at different observation levels.

The topic of the statistical testing of heterogeneous materials at multiple scales is addressed in Chapters III and IV. In Chapter III, the probabilistic formulation is developed to aid tracing the homogenization effect observed in the experimental grid indentation on heterogeneous solids. The simplified model microstructure of polycrystalline and fiber-reinforced materials are constructed, and the influence of the characteristic length scale of the indentation test on the measured material response is investigated. The focus of Chapter IV is on statistical phase identification in the framework of the multivariate Gaussian Mixture Modeling based on the Maximum Likelihood estimation and Expectation Maximization algorithm. The proposed deconvolution approach is validated on the basis of experimental results representing a broad spectrum of heterogeneous materials, from investigated fired clay brick to ordinary cement paste and naval brass alloy. The inference of the number of phases,

with the highest probability to occur and compatible with the experimental grid indentation data, is outlined.

The methodology refined in Chapter IV is then applied in the experimental study of the mechanical performance of the 'glassy' matrix, addressed in Chapter V. The detailed experimental protocol of depth-sensing technique is presented together with the measured Young's modulus and hardness of the matrix phase. The composite nature of the 'glassy' bond is corroborated. Finally, the mechanical properties of the accessory phases incorporated within the brick microstructure are indentified.

The last part, Chapter VI, summarizes the main findings of this study and discusses briefly future perspectives. Additional information complementing the ideas developed and discussions held in this work are outlined in Appendixes.

I.6. REFERENCES

[1]H. Reh, "Current classification of ceramic materials," pp. 39-62 in Extrusion in ceramics, Engineering Materials and Processes. Edited by F. Händle. Springer-Verlag Berlin Heidenberg (2007).

[2]W. D. Kingery, H. K. Bowen, D. R. Uhlmann, Introduction to ceramics. 2nd Edition, Wiley-Interscience Publication (1976).

[3]Y. Iqbal, W. E. Lee, "Fired porcelain microstructures revisited," J. Am. Ceram. Soc., 82 3584-90 (1999).

[4]G. Constantinides, Invariant mechanical properties of calcium-silicate-hydrates (C-S-H) in cement-based materials: Instrumented nanoindentation and microporomechanical modeling, Doctoral Thesis, Massachusetts Institute of Technology (2006).

[5]Ch. P. Bobko, Assessing the mechanical microstructure of shale by nanoindentation: The link between mineral composition and mechanical properties, Doctoral Thesis, Massachusetts Institute of Technology (2008).

[6]United Nations, Year Book, Industrial commodity statistics, Building bricks made of clay, www.un.org (2003).

[7]European Commission, European Statistics Eurostat: Industry, trade and services. www.ec.europa.eu/eurostat (2006).

[8]European Commission. A green Vitruvius. London: James & James (1999).

[9]Brick Development Association, UK and Ireland, www.brick.org.uk/industry-sustainability.html

[10]Ch. Koroneos, A. Dompros, “Environmental assessment of brick production in Greece”, Build. Envir., 42 2114-2123 (2007).

[11]Stern Report, UK (2006).

[12]J. Martin-Marquez, A. G. De la Torre, M. A. G. Aranda, J. Ma Rincon, M. Romero, “Evolution with temperature of crystalline and amorphous phases in porcelain stoneware,” J. Am. Ceram. Soc., 92 229-234 (2009).

II. Multi-Technique Investigation of Extruded Brick Microstructure

ABSTRACT

Despite the omnipresence of clay brick as construction material since thousands of years, fundamental knowledge about the link between composition, microstructure and mechanical performance is still scarce. In this chapter, we employ a variety of advanced techniques of experimental mechanics and material characterization for extruded clay brick for masonry, that range from Scanning Electron Microscopy (SEM) coupled with Energy-dispersive X–ray Spectroscopy (EDX), Mercury Intrusion Porosimetry (MIP), to Instrumented Nanoindentation, macroscopic strength and durability tests. We find that extruded clay brick possesses a hierarchical microstructure: depending on the firing temperature, a ‘glassy’ matrix phase, which manifests itself at sub-micrometer scales in form of neo-crystals of mullite, spinel-type phase and other accessory minerals, forms either a granular or a continuum matrix phase that hosts at sub-millimeter scale the porosity. This porous composite forms the backbone for macroscopic material performance of extruded brick, including anisotropic strength, elasticity and water absorption behavior.

II.1. INTRODUCTION

Clay brick, whose origin can be traced back to around 4300BC,[1] still finds wide use in today's building industries. Next to concrete and steel, masonry is the most used construction material on Earth. Infill panels, masonry veneer and low-rise structural masonry buildings are common applications of clay brick.[2] However, in contrast to other construction materials (cement-based materials, metallic materials, polymer-based composites etc.), the implementation of the engineering science approach for masonry has lagged behind, creating an increasing gap between wide-spread use and fundamental understanding of masonry. With a focus on linking the mechanical performance and durability of contemporary masonry materials with basic constituents present at different scales, the overall goal of this paper is to contribute to filling this gap.

In order to reach this goal, we present results from an extensive experimental campaign targeted at the detailed characterization of clay brick over seven orders of magnitude (from 10^{-9} [m] to 10^{-2} [m]), which includes elemental and phase composition, microstructure investigations, and mechanical property characterization at nano and macro-scales. The elemental and phase composition is determined with the aid of Energy-dispersive X-ray Spectroscopy (EDX) and X-ray Diffraction (XRD). The extensive use of Scanning Electron Microscopy (SEM) on the polished sections of ceramics allows the capturing of microstructural features, from a scale of tens of nanometers to hundreds of micrometers. Additionally, Mercury Intrusion Porosimetry (MIP) combined with Digital Image Analysis (DIA) of SEM images, proves to be a beneficial mean to characterize pore size distribution, void shape and alignment as well as interconnectivity. Furthermore, the mechanical properties of this heterogeneous material are investigated with the aid of instrumented nano-indentation reinforced with massive grid indentation technique,[3,4] in addition to conventional uniaxial compression tests at macro-scale. These results are synthesized into a multi-scale model of brick, which allows one to pin down the effect of composition and processing on macroscopic material performance.

II.2. MATERIALS

The investigated materials represent two types of solid brick commonly employed in the construction industry; facing brick (labeled B1) and general use common brick (labeled B2). The facing brick is manufactured in a fully automated fashion. It is fired inside a gas fuelled

tunnel kiln for a ~55 [h] firing cycle duration. Maturing of the ware is achieved at 1030 [ºC] for about 5.5 [h]. The second type of brick, B2, is an example of a building ceramic, which has been produced with a more traditional technology. The green ware is dried in semi-open space above running annular kiln of Hoffman type construction. The kiln's chambers are charged with the dried, green brick, which then is fired to the maximum temperature of 950-980 [ºC]. The cycle from cold-to-cold takes 72 [h] with a maturing time of ~7.5 [h]. Both types of investigated brick are shaped with soft extrusion technique (B1-along the height or normal to the bed face, B2-along the length or normal to the head face) to attain standard brick dimensions 24×11.5×6.5 [cm].

Raw materials for the production of bricks B1 and B2 present chemical and mineralogical similarities, with kaolin (*K*) and muscovite (*M*) as the main clay mineral species, together with K-feldspar microcline (*Kf*) and some traces of plagioclase series (*Pf*) in B1, quartz (*Q*) and accessory minerals, such as hematite (*H*), rutile and calcite (*C*) (<3 [wt%] in sample B1), see Table II.1 and Figure II.1.

Table II.1 Chemical composition [wt%] of the raw materials measured with Wavelength Dispersive X-ray Fluorescence (WDXRF).

Sample	Al_2O_3	SiO_2	TiO_2	K_2O	MgO	CaO	Na_2O	Fe_2O_3	LOI
B1	19.74	60.96	0.96	2.25	0.86	1.49	0.35	5.53	7.65
B2	18.61	65.96	0.88	2.14	0.51	0.16	0.25	5.28	6.04

Components with concentration below 0.1 [wt%] are excluded from the table. LOI – loss on ignition.

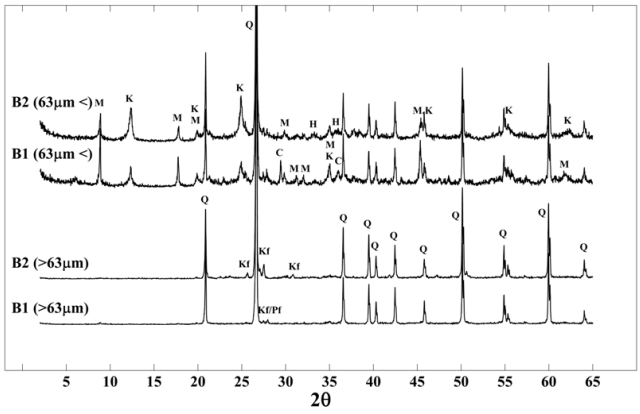

Figure II.1 XRD spectra of B1 and B2 raw materials with phase identification: kaolin (*K*), muscovite (*M*), microcline (*Kf*), plagioclase feldspar (*Pf*), quartz (*Q*), hematite (*H*).

II.3. METHODS AND RESULTS

II.3.1. Phase Identification

The characteristic feature of structural ceramic materials is their complexity with respect to the number of incorporated phases as well as its microstructural arrangement. The first aspect may be quite accurately resolved with the aid of XRD, which is well known in the earth sciences and other fields.[5,6] For this purpose, the samples of investigated materials B1 and B2 have been prepared in the form of powder passing the standard sieve ASTM No.230 as well as polished sections of bulk solids. Six powder samples and three polished samples for each type of brick were investigated in the Bruker D8 Discover diffractometer, with conventional Bragg-Brentano geometry and cupper radiation *CuKα*. The spectra has been collected over *2θ* intervals ranging from 5º to 70º degrees, with step size 0.05º and time step 3 [s]. The phase matching has been carried out using the standard patterns included in the database of The International Center for Diffraction Data (ICDD).

Both types of investigated brick are composed of common phases: *α*-quartz (*Q*), K-feldspar (*Kf*), hematite (*H*) and mullite (*Mu*). Mullite seems to be more abundant in the B1 sample, even if its traces are also recorded in the B2 sample (see Figure II.2). This result is due to the higher temperature applied in the firing of the facing brick, which is above 980 [ºC], considered as the point of formation of γ-Al_2O_3 spinel-type phase (*S*) accompanied by mullite development from melting kaolinite and muscovite clay minerals.[7,8,9,10] Hence, it is not surprising that the muscovite mineral is still easily detected in the B2 sample with the lower processing temperature. The significant amount of the background signal can be attributed to the presence of an amorphous phase, e.g. aluminosilicate glass. The contribution of this non-crystalline solid to the brick microstructure increases with the temperature and spans from around 10 % in weight for brick fashioned at 900 [°C] to as much as 40 % for processing temperature of 1100 [°C]. [11,12]

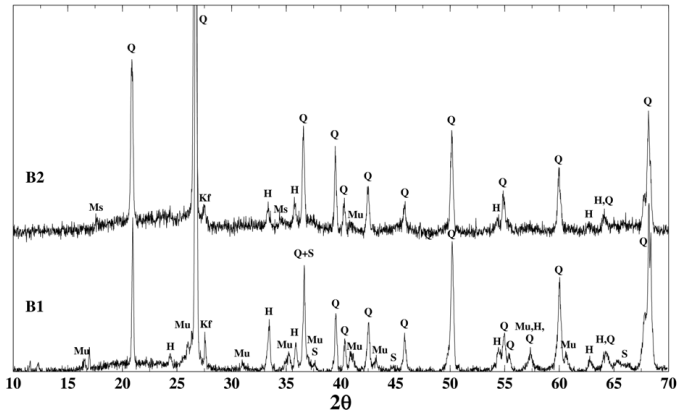

Figure II.2 XRD spectra of B1 and B2 with phase identification: α-quartz (*Q*), K-feldspar (*Kf*), hematite (*H*) and mullite (*Mu*).

The results of this qualitative analysis are supported by the results of EDX elemental mapping on polished sections of bulk samples. Distribution maps of silicon (*Si*), aluminum (*Al*) and other incorporated elements were collected, and the regions close to the theoretical composition of quartz (red), feldspar (dark blue) and hematite (violet) could be identified (see Figure II.3). The 'binding phase' (green and yellow) is a composite of crystals of mullite and spinel-type phase embedded in the glass (sample B1). However, the geometrical forms of these minerals could not be obtained in this analysis, because of the fine character of the crystal structures of sub-micron size as well as the presence of hosting glass. The features of this size are below the spatial resolution limit, which is rarely much better than 1 [μm] in this type of analysis[13] and is implied by the volume of the material probed with the electron beam in EDX coupled to conventional SEM microscope.

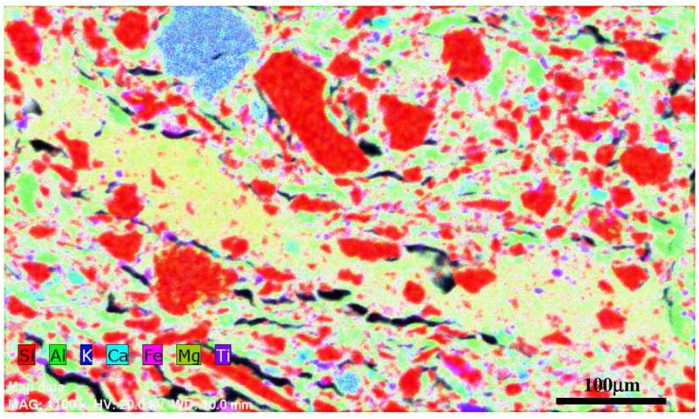

Figure II.3 Typical EDX composite map of elemental composition of fired brick obtained from the tests: quartz (red), feldspar (blue), hematite (violet), aluminosilicate composite matrix (green), pocket of aluminosilicate matrix rich in alkali oxides (yellow).

This phase identification analysis reveals, in a simple manner, how the brick processing temperature can affect its mechanical and physical performance. The mechanical strength and stiffness may be expected to be higher in sample B1, since the relatively weak backbone of the compacted green ware composed of the clay minerals has been transformed into a stronger one made of mullite and spinel crystals mainly wrapped in amorphous glass. In contrast, sample B2 tends to preserve still the original internal structure, since the phase transformation process has not been fully accomplished and a large fraction of clay minerals is still detectable. Coarse particles of quartz and feldspar in both materials tend to be the filler, akin to gravel aggregates in concrete.

II.3.2. Microstructure

Prior to the investigations of the microstructure, a minimum of three samples for each type of brick were cored (along the shortest edge of the brick) from the central part of the solid unit, and the polished sections were prepared. The preparation procedure includes: impregnation under vacuum with low viscosity epoxy resin EpoThin Buehler, coarse grinding on the diamond disc 45 [μm] Apex DGD Buehler, and fine polishing with water based diamond suspensions grade 9 [μm], 3 [μm] and 1 [μm] applied on perforated pad TexMetP Buehler. In the last pass a 0.25 [μm] oil based diamond suspension grade, in exchange with colloidal silica, was occasionally used during a short duration. The surfaces oriented along the length, width and height of the brick were exposed to microscopic examination. A minimum of 12 images for each magnification step (×100≈1238×925 [μm], ×200≈619×463 [μm] and ×400≈310×231 [μm], image resolution 712×484 and 3584×3301 pixels) was acquired on the surface at randomly selected locations, with the Backscattered Electron Detector (BSEM). Qualitative and quantitative analysis of the porous domain was carried out on normalized binary images constructed via the automatic thresholding procedure proposed by Otsu[14,15] and implemented into ImageJ, a non-commercial image analysis package.[16]

Additionally, to resolve the nano-crystals of mullite and other phases existing within the binding matrix of brick B1 and the aggregates of molten clay structures existing within brick B2, chemical etching with 6 % hydrofluoric acid HF was carried out for 1 [min] to 4 [min] prior to SEM imaging.

The experimental micrographs expose, at different length scales of observation, the dominant features of the microstructure of B1 and B2 samples. Both microstructures converge to a common pattern at larger length scales. On the other hand, the building blocks present at the lowest level considered here ($<10^{-6}$ [m]) diverge significantly, preserving only the

chemical similarity. Hence, each material is characterized by a different type of matrix phase (see Figure II.4(a-b) and Figure II.5(a-b)), which hosts larger scale components.

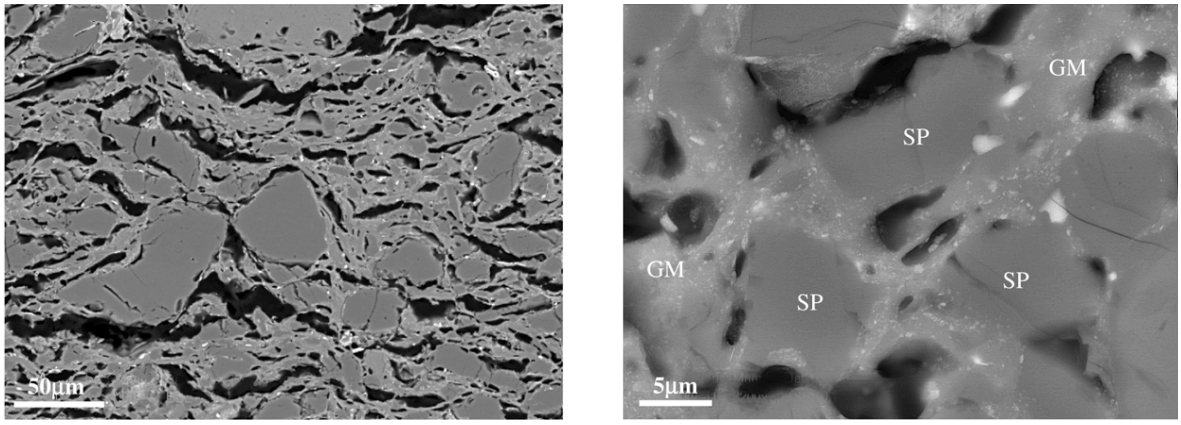

(a) (b)

Figure II.4 BSE-SEM micrographs of the sample B1: a) microstructure in the section with normal vector oriented along the length of the brick (notice, the extrusion axis is parallel to the longer edge of the image), characteristic coarse voids with preferential orientation along the green body extrusion direction, b) detailed view at the composite of silt particles (*SP*), polycrystalline-amorphous 'glassy' matrix (*GM*) and finer porosity.

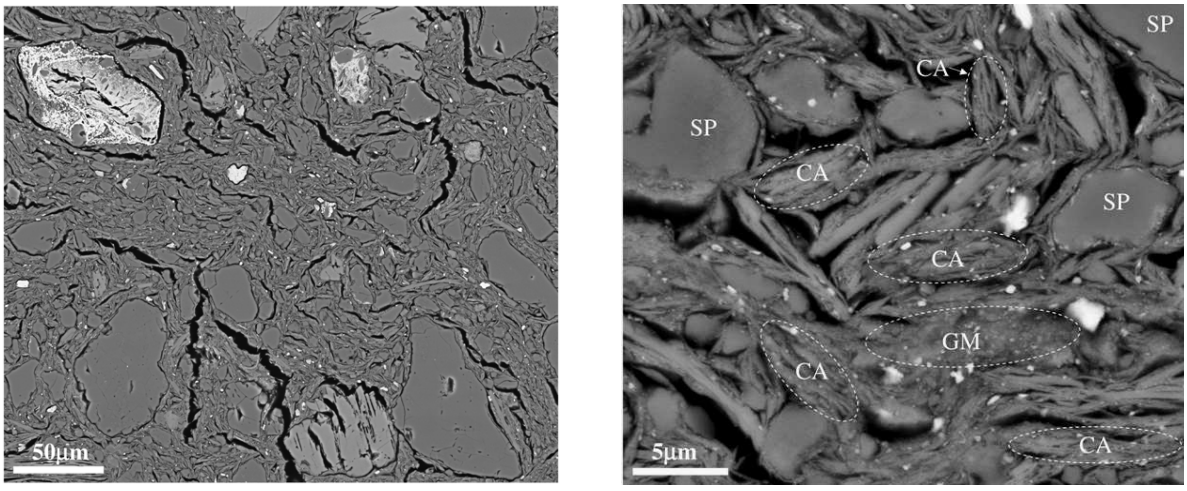

(a) (b)

Figure II.5 BSE-SEM micrographs of the sample B2: a) microstructure in the section with normal vector oriented along the length of the brick (notice, the extrusion axis normal to the plane of the image), microstructure with dominant population of finer porosity and rare coarse voids, b) detailed view at the 'granular' microstructure composed of silt (*SP*), remnants of porous aggregates of clay (*CA*), early developed pocket of the 'glassy' melt (*GM*) and porosity.

More specifically, the matrix of facing brick B1 is a composite of amorphous glass, crystals of primary mullite (*PM*) and occasional acicular forms of secondary mullite (*SM*), spinel-type phase and hematite (*H*) (Figure II.6(a)). The size of incorporated crystals varies from nano- to micrometer depending on mineralogy of raw materials and processing conditions, as revealed in transmission electron studies (TEM) carried out by other researchers.[8,9,17,18,19]

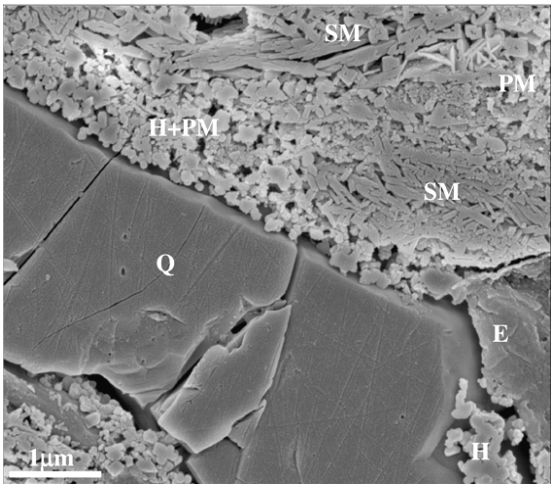

(a)

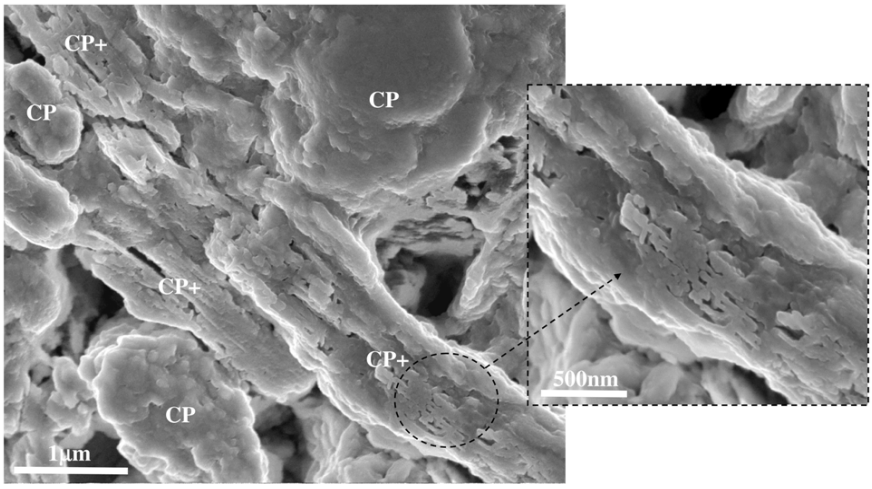

(b)

Figure II.6 Typical detail of investigated microstructures exposed after chemical etching in 6 % hydrofluoric acid (*HF*): a) sample B1 with crystals of mullite (*PM*-primary mullite, *SM*-secondary mullite) and hematite (*H*), quartz (*Q*) and epoxy resin (*E*), etching time 1 [min], b) detailed look at the fraction of large aggregate of remnants of clay particles (*CP*) existing within the matrix of sample B2, regions (*CP+*) with apparent formation of new geometries in nanometers size from clay laths, etching time 2 [min].

In contrast, the main matrix components of the B2 sample are porous complexes of dehydroxylated and partially molten clay particles (Figure II.6(b)), together with rare local clusters of glass reinforced by early developed nano-crystals. The matrix in the B2 sample is reminiscent of the green ware (Figure II.5(b)), while a complete new structure has been developed in sample B1 upon firing (Figure II.4(b)). Otherwise said, there is a clear structural difference in matrix for the brick microstructure as a consequence of the firing process (temperature and duration). This observation suggests that the response of both microstructures (materials) to prescribed physical and mechanical loads is expected to be different, due to the different forms of the matrix present in the two types of clay brick.

The composite matrix phase discussed before is an inherent structural element of the microstructure at larger scales, $10^{-6} < l < 10^{-4}$ [m]. At this level new components of the brick microstructure become relevant, namely micro-porosity and aggregates of silt. The difference in the characteristics of micro-porosity can be directly observed on the SEM micrographs previously shown (Figure II.4(a) and II.5(a)) and can be quantified with the aid of DIA technique, MIP and standard gravimetric and capillary suction methods (Table II.2).

Table II.2 Average porosity [%] measured with water immersion, MIP and DIA (values in brackets represent the coefficient of variation in [%]).

Sample	water immersion[1,2]	MIP[1,3]	DIA[4]
B1	21.7(5.6)	22.1(1.6)	23.1(6.1)
B2	23.4(4.9)	23.5(3.5)	22.0(8.6)

1) apparent porosity, 2) ASTM C67-09,[20] 3) ASTM D4404–84(2004),[21] 4) total porosity, size of the observation window ×100≈1238×925 [μm]. Minimum number of samples per test N_{min}=6.

The volume occupied by the voids in both samples is comparable with slight increase in sample B2, but the pore size distributions curves obtained by DIA exhibit different modality and different location of the modes (see Figure II.7(a)). The porosity in sample B1 exhibits a unimodal distribution with the mode located at d_{eq}≈18 [μm] and a negative skew, where voids tend to concentrate toward larger equivalent diameters (log-normal distribution). The voids of this sample are within an interval of 1 to 100 [μm]. In contrast, the porosity domain within the microstructure of sample B2 exhibits higher variability of voids with respect to the assumed equivalent diameter. In this case, a clear bimodality is encountered, which represents two families of pores separated by one order of magnitude in size, $d_{eq,I}$≈3 [μm] and $d_{eq,II}$≈30 [μm].

In addition, the entire pore distribution is inscribed within a significantly larger domain. Pores with diameters of hundreds of nanometers seem to occupy a non-negligible fraction of the total porosity. According to this analysis, sample B1 represents a coarser and more uniform porosity distribution, while a more refined structure with larger variation is observed for sample B2.

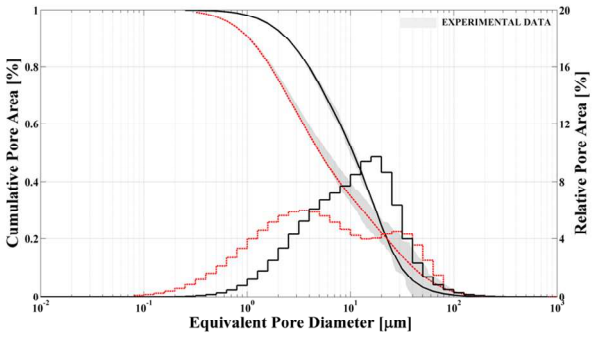

(a)

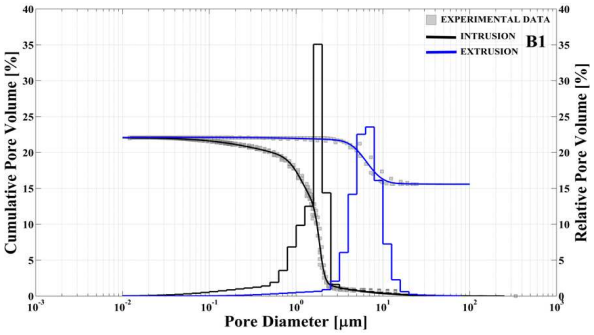

(b)

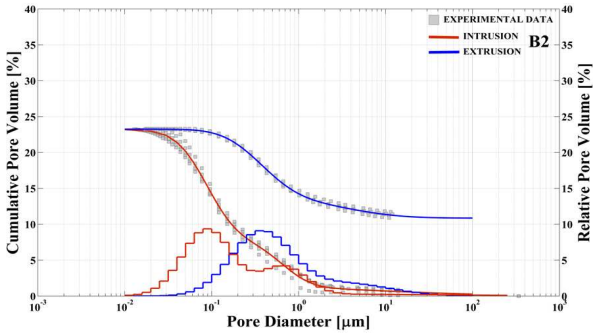

(c)

Figure II.7 Experimental cumulative distribution of the pore size measured with: a) DIA based on high resolution micrographs (B1-black, B2-red), b-c) MIP carried out in the single intrusion-extrusion cycle on the facing brick B1 and common building brick B2. The solid lines represent the fit with the univariate mixture model of two log-normal components obtained with Matlab®. The correction for the compressibility of the system penetrometer-mercury-sample not applied.

This significant difference between the microstructure of the investigated bricks at the intermediate material scale is confirmed by mercury intrusion investigation (Figure II.7(b-c)). Carried out in low and high pressure regimes with AUTOPORE IV 9510, Micromeritics, six specimens of each sample with an average dried mass of 7.5 [g] and volume 3.6 [cm^3] were studied on the single intrusion-extrusion cycle up to the maximum pressure of 100 [MPa] and

an equilibration time of 10 [s]. The MIP results on intrusion confirm the difference in modality for the two samples, as well as the tendency of B1 sample towards a coarser porous domain than the one incorporated within B2 brick. Similar observation is given by the MIP drainage results, although the bimodality becomes less apparent in this case for brick B2. Despite the qualitative good agreement of MIP and DIA analysis, there exists an evident discrepancy between them, due to the different location of the modes. The peaks obtained on intrusion cycle, as well as the entire distribution, tend to shift towards smaller diameters.[22] Such a bias, which is also referred to as the 'ink bottle effect', occurs when the void to be filled with intruding mercury encounters narrow throats, leading to the misrepresentation of the pore as having the diameter of its throats, see Abell et al.[23] for a description of this phenomenon in complex microstructures of cement-based materials.

The last feature of the micro-porosity domain to be discussed here, at observation scale $10^{-6} < l < 10^{-4}$ [m], is the preferential orientation along one specific direction. This effect has been observed more pronounced in the B1 sample under the SEM microscope (see Figure II.4(a)) and may be attributed to the technology of brick shaping by extrusion at the green stage. In this process, the plastic mass is forced through a die that is placed in the end of the pressure head of the extruder, leading to the development of interlaminar tangent stresses. These stresses provoke alignment of the irregular particles along streamlines and the occurrence of laminations in the green ware (Figure II.8). Simultaneously, the air pockets present within the plastic body, due to the insufficient vacuum inside the de-airing chamber, adopt a scalene ellipsoidal form with dominant axis aligned with the extrusion direction.

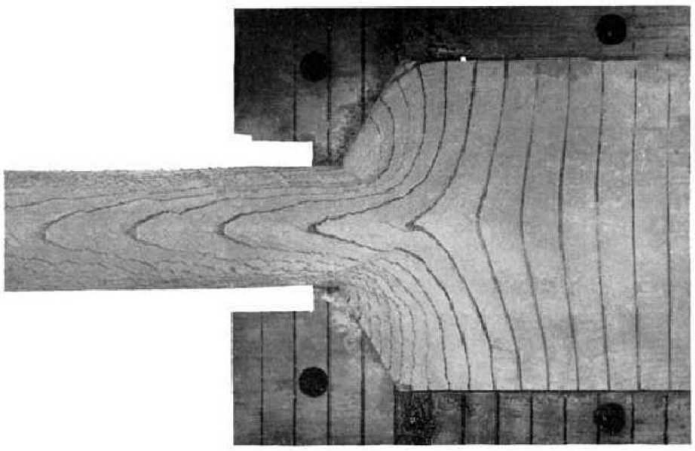

Figure II.8 Slip-lines and laminations within the plastic mass during processing in the piston extruder, adapted from Bartusch and Händle[24] with kind permission of Springer Science & Business Media.

The results from water absorption experiments by capillary action, carried out independently for each different direction, corroborate the microstructural signature related to the extrusion technique (Figures II.9). In this setup each cylindrical core ϕ=2.5 [cm] and h=5.0 [cm] (six cores for each direction) are brought in contact with water through its bottom face, and the mass of absorbed water is monitored over time.[20]

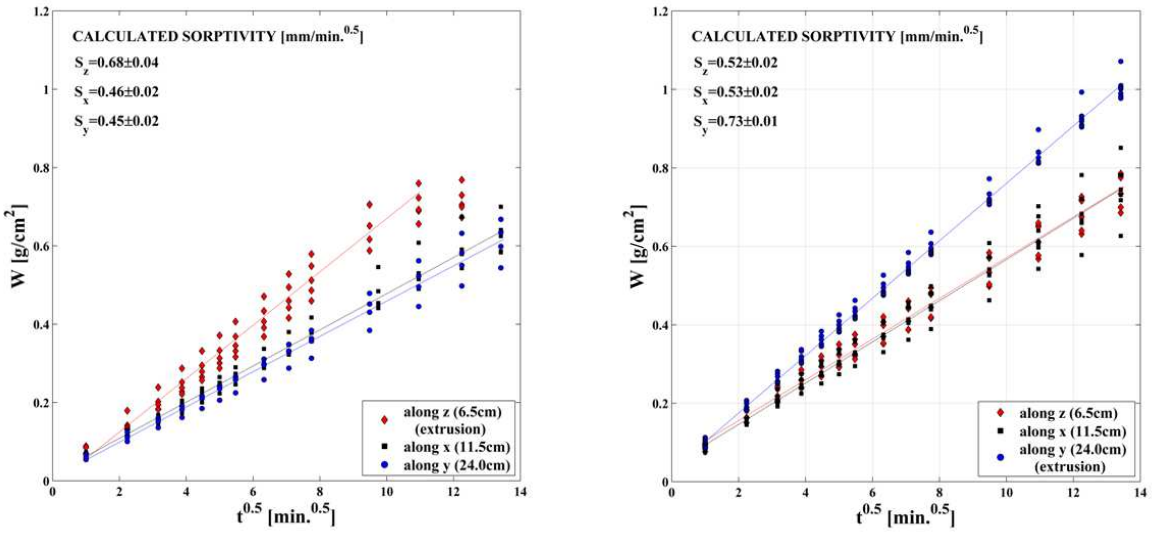

(a) (b)

Figure II.9 Capillary water uptake: a) B1, b) B2. The axes are oriented according to the width (X), length (Y) and height (Z) directions. Note that the extrusion directions are Z for B1 and Y for B2. The apparent, small positive W-intercept at $t^{1/2}$=0 due to unsealed sides of the specimens.[25]

The weight change behavior of both samples shows a significant difference with respect to the orientation (see Figure II.9(a-b)): samples cored along the direction of extrusion present the highest sorptivity ($S_z/(S_y,S_x)\approx1.5$ for B1, $S_y/(S_x,S_z)\approx1.4$ for B2) and significantly diverge from the two other groups, in which the trend in water absorption appears to be quite similar ($S_x/S_y\approx1$ for B1, $S_x/S_z\approx1$ for B2). The movement of water within the system of micro-voids is considerably facilitated along the extrusion direction. Such phenomena may occur if the microstructure of the material exhibits an aligned porosity with enhanced interconnectivity or a laminar microstructure (see Figure II.4(a) and Figure II.8). Features of this type effectively increase the rate of water movement along direction of the alignment (see Figure II.10(a-b)).

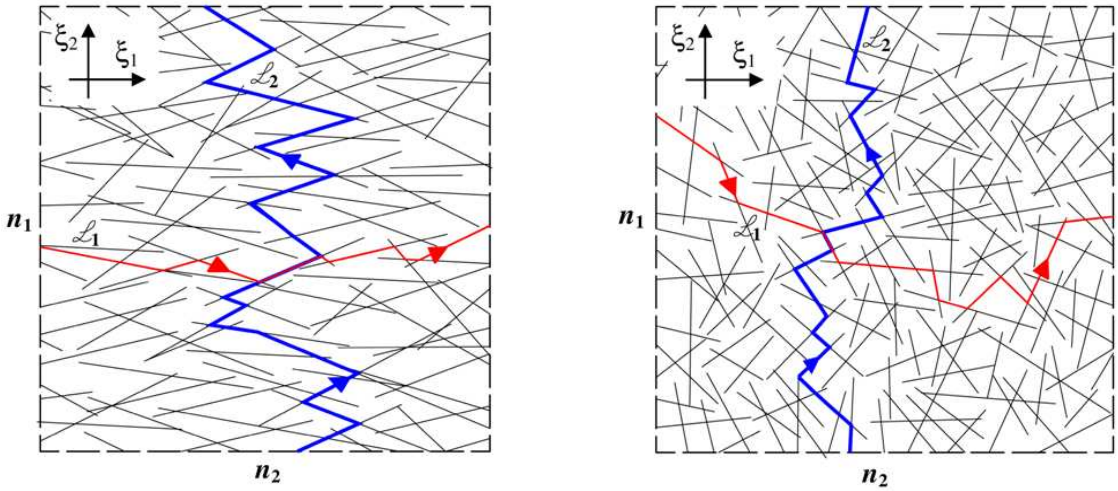

(a) (b)

Figure II.10 Simplified 2D scheme of the model material with capillary voids and suction of the water for two different orientations ξ_1, ξ_2 (capillary tube with uniform section model): a) material with preferential orientation of the voids, the length of the average path $\mathscr{L}_1 < \mathscr{L}_2$, the average number of capillary inlets $n_1 > n_2$, b) no alignment, distributional isotropy $\mathscr{L}_1 \approx \mathscr{L}_2$, $n_1 \approx n_2$.

Finally, at larger scales, $l > 10^{-4}$ [m], SEM images confirm features identified previously by other researchers,[26,27] namely the presence of coarse aggregates associated with inherent fissures as well as discontinuities at the interface of coarse aggregates and 'glassy' matrix, together with large meso-voids (cracks). The cracks have been attributed to the volume contraction during phase transformation of quartz from its β-form to the more stable at room temperature α-form, while the discontinuities at the boundaries have been considered to result from the mismatch in thermal expansion coefficients between quartz and composite of 'glassy' matrix, silt grains and micro-porosity.

II.3.3. Mechanical Performance

Following the analysis of phase composition and microstructural features, the effect of composition and microstructure on the mechanical performance of the investigated brick samples is addressed using a combination of classical macroscopic strength tests and nanoindentation tests.

Macroscopic compressive strength $f_{c,i}$ and modulus of elasticity E_i of both materials in three directions $i=X,Y,Z$ (see Table II.3) were obtained by standard compression tests on

cylindrical samples with a height to diameter ratio of two (*h/D=2*). A minimum of 12 tests was carried out in each direction according to the procedure adopted from.[28] Note that it is normal practice to report the macroscopic compressive strength of brick, which is a basic and much used material property for mechanical characterization, even if the values in different directions are not usually reported.

Table II.3. Average Young's Modulus and Compressive Strength measured at macro-scale. Note that the extrusion directions are *Z* for B1 and *Y* for B2 (values in brackets represent the coefficient of variation in [%]).

Sample	E_X[1]	E_Y[1]	E_Z[1]	$f_{c,X}$[2]	$f_{c,Y}$[2]	$f_{c,Z}$[2]
B1	5.4(11.6)	6.2(10.7)	8.0(5.6)	64.2(11.2)	65.3(18.7)	82.8(13.7)
B2	2.4(7.7)	3.8(3.9)	2.0(17.5)	44.2(10.4)	56.2(10.5)	42.6(8.0)
BR[3]	---	10.4(3.6)	12.7(4.4)	---	51.0(12.0)	56.8(6.4)

1) [GPa], 2) [MPa], 3) Brick reference reported by Oliveira et al.[29].

As expected, the results show that facing brick type sample B1 has significantly higher mechanical properties than the common brick B2 (Table II.3). For instance, the maximum strength capacity of B2 is ≈56 [MPa], compared to a strength capacity of ≈83 [MPa] for B1, which are values within the expected range for solid clay brick. Due to the high strength, both materials exhibit rather brittle failure at the strength limit.

A similar trend is observed for the modulus of elasticity, although reported values may be somewhat reduced due to the compliance of the experimental setup. In agreement with results reported by Oliveira et al.,[29] the highest strength and modulus are found along the axis aligned with the direction of green body extrusion. The performance of both materials in directions perpendicular to the extrusion direction is quite similar. This suggests that extruded bricks exhibit at macroscopic level (at least) transverse isotropic elastic behavior characterized by five elastic constants.[30]

The macro-scale mechanical behavior is inherently linked to microstructure and constituent properties at nano- and micro-scale. In order to quantify this link, the best experimental technique able to assess mechanical properties at the smallest and intermediate material scales is instrumented indentation,[31] employed in form of massive grid indentation technique.[32] This testing procedure, which originates from the traditional hardness measurement developed by Brinell,[33] is based on the continuous monitoring of the load and

displacement of the hard probe as it is driven and withdrawn from the material at discrete locations of a grid $l_x \times l_y$ that spans a specific region on a material surface $L_x \times L_y$ (Figure II.11(a-c)). The obtained load-displacement diagrams (Figure II.11(a)) allow the determination of the material hardness H_i and indentation moduli M_i (Figure II.11(b)) at each location (Figure II.11(c)), based on the contact area at maximum load and initial unloading stiffness.[34,35]

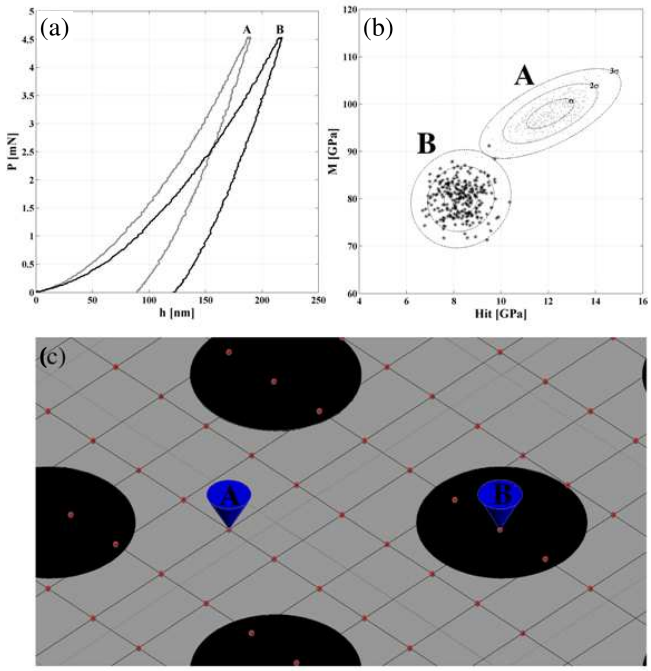

Figure II.11 Assessment of the mechanical properties by instrumented indentation with massive grid concept: a) indentation curves on the fictitious biphasic material, b) deconvolution of experimental data, c) the scheme of the experimental grid $l_x \times l_y$ on the surface of the material.

In case of composite materials, the *i-th* node record of hardness and indentation modulus, $\boldsymbol{x}_i=[H_i;M_i]$, may belong to one $j=1\ldots n$ of n mechanically active phases G_n with average properties $(\bar{H}_j;\bar{M}_j)$. Hence, the statistical analysis (deconvolution) that is carried out on the grid dataset (Figure II.11(b)) aims at estimating the number of statistically significant phases, as well as their vectors of mean properties with covariance matrices $\boldsymbol{\varphi}_j=[\boldsymbol{\mu}_j,\boldsymbol{\Sigma}_j]$ and associated fractions π_j. Recent literature reports a variety of deconvolution strategies applied for this purpose.[4,32,36] We employ here a multivariate mixture model to identify the number of phases and phase properties. Based on the Finite Gaussians Mixture Model (FGMM) (Eq. II.1 and

Eq. II.2),[37,38] the estimation of the parameters is carried out according to the Maximum Likelihood (ML) function, via the Expectation Maximization (EM) algorithm,[39] with the aid of non-commercial program called EMMIX developed by Peel and McLachlan.[38,40]

$$f(\mathbf{x};\boldsymbol{\psi}) = \sum_{j=1}^{n} \pi_j f_j(\mathbf{x};\boldsymbol{\varphi}_j) \qquad \text{II.1}$$

$$\sum_{j=1}^{n} \pi_j = 1,\ \pi_j \geq 0 \qquad \text{II.2}$$

The applicability and efficiency of this experimental approach and statistical analysis technique with reference to clay brick is briefly presented next and discussed on the basis of results (Figure II.12(a-d)) selected from the experimental campaign on facing brick B1.

The porous samples were impregnated with epoxy resin prior to indentation testing. This resin impregnation was employed in order to facilitate the preparation of a smooth surface by the polishing process, and to be able to identify porosity by contact experiment due to a significant lower hardness of the solidified epoxy resin (H≈0.3 [GPa]) compared to the hardness of the 'glassy' matrix, quartz and other incorporated phases. However, this mismatch in hardness and required prolonged polishing time may provoke a rounding of edges of hard phases or their removal, which may entail some ill-conditioned measurements. A fine statistical analysis is required to identify and isolate such tests from the overall analysis.

The qualitative picture regarding the phases within the investigated region in this particular analysis is given by the BSEM micrograph (Figure II.12(a)). Three main components can be distinguished (confirmed by EDX analysis), namely silt aggregates (quartz), 'glassy' matrix and porosity filled with hardened epoxy resin. Each of the components has distinct mechanical properties. However, while the hardened epoxy resin and quartz may be considered as homogeneous phases at this scale, the 'glassy' matrix developed within facing brick B1 is a composite material, in which fine nano-crystals of mullite and other accessory minerals are incorporated and are bonded by aluminosilicate glass.[17,18,41,42]

In the chosen experimental setup the indentation mesh spans a region $L_x \times L_y$=60×54 [μm] and includes $N \times M$=41×37 indentation points. The indentations with Berkovich diamond tip are force controlled, with a maximum force of P=2.25 [mN] provoking penetration depths between ≈130 [nm] for hard grains and ≈700 [nm] for soft epoxy filling the pores. The CSM nanoindentation tester equipped with the temperature and moisture controlled enclosure has been used. The statistical deconvolution of the data in the form 'as received' (including abnormal measurements) is presented in the form of a scatter diagram in the H-M plane

together with simultaneous allocation of data into statistically significant groups (Figure II.12(d)). Using a Bayesian Information Criterion (BIC),[43] it is possible to identify a minimum value of BIC for seven normal components.

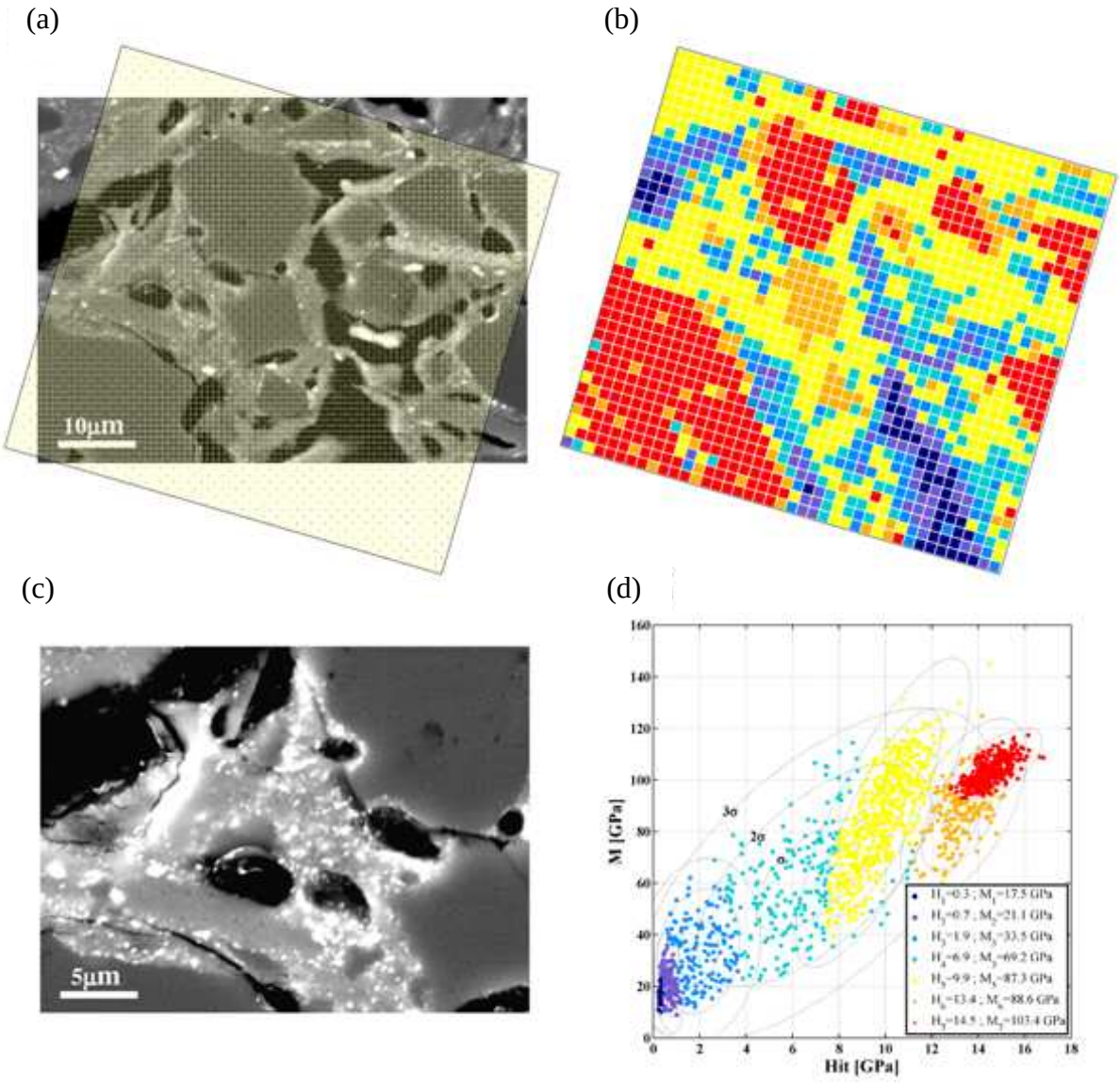

Figure II.12 Massive Grid Indentation on sample B1: a) BSEM micrograph of local microstructure with outline of the grid $N \times M$ = 41×37, l_x = l_y = 1.5 [μm], P = 2.25 [mN], $\dot{\tau}_{loading}$ = $\dot{\tau}_{unloading}$ =5 [mN/min], t_{dwell} =5 [s], b) probabilistic map of mechanical phases, c) indentation imprints, d) deconvolution with Gaussians Mixture Modeling.

The first four clusters have mean hardness and indentation moduli significantly lower than the rest. Such statistically significant phases are associated with indentation on pores filled by epoxy. In contrast, the remaining three clusters represent indentations on (i) the bulk ‘glassy’

matrix, H_5=9.9 [GPa], M_5=87.3 [GPa], and (ii) different aggregates of quartz, H_6=13.4 [GPa], M_6=88.6 [GPa] and H_7=14.5 [GPa], M_7=103.4 [GPa]. This hypothesis is validated by the microstructural phase map shown on BSEM image and its statistical reproduction based on a cluster analysis of the indentation data, subjected to direct comparison (Figure II.12(a-b)). According to this analysis, the aggregates of quartz are properly recognized (red and orange) as well as the group of indents that represent the binding matrix (yellow). Additionally, it is noticed that the experimental records allocated to the first four groups are linked to pores intruded by epoxy. In turn, this group may also include some abnormal measurements (imperfect contact detection, fracture etc.), which in general fall in the lower range of measured quantities.

To confirm the initial conclusions, a filtering of experimental data was carried out with respect to the possible deviations from continuous load-displacement curves $P \propto h^m$,[34] which typically point to degenerated measurements, such as fracture under the indenter, soft-on-hard behavior or other anomalies (Figure II.13(a-c)). The filtered dataset was then deconvoluted again using the described cluster algorithm (Figure II.13(d-e)). The following main observations may be drawn: the group of records with the lowest hardness and modulus is enlarged leading to a shift in the vector of mean properties H_1=0.3→0.4 [GPa] and M_1=17.5→20.0 [GPa], and the families G_2 and G_3 previously indentified are absent in the deconvolution of the filtered data set. Hence, the data of these two groups establish a statistically significant set, which was identified in the original analysis. Moreover, next to the rare events on grains of quartz and matrix, the set of ill conditioned indentation events includes mostly the ones located within the void domain in close proximity (boundary zone) of the 'glassy' matrix or quartz (see Figures II.12(b) and Figure II.13(d)). The latter groups do not experience significant alterations in mean properties as well as allocation of the records upon data filtering.

The experimental indentation modulus of the quartz phase obtained from this analysis appears to be very close to the stiffness values reported in the literature for single crystal of quartz (C_{33}≈106 [GPa] and C_{11}≈87 [GPa]).[44] The first of the mean values M_6≈87 [GPa] associated with the quartz phase approaches C_{11} and is around 10 % higher than Young's modulus in this direction E_{11}≈79 [GPa], while the second M_7≈103 [GPa] is just slightly lover than C_{33}, but becomes equal to E_{33}≈103 [GPa]. Additionally, the average value of both means is in close proximity of the Voight-Reuss-Hill average E_{pol}≈99 [GPa].[44] However, it must be emphasized at this point that the indentation modulus M for crystal materials is considered to

represent some average of elastic constants, which additionally depends on the orientation of the indented surface with respect to the material axes.[34,45] Therefore, it does not correspond directly to any of the referred stiffness values.

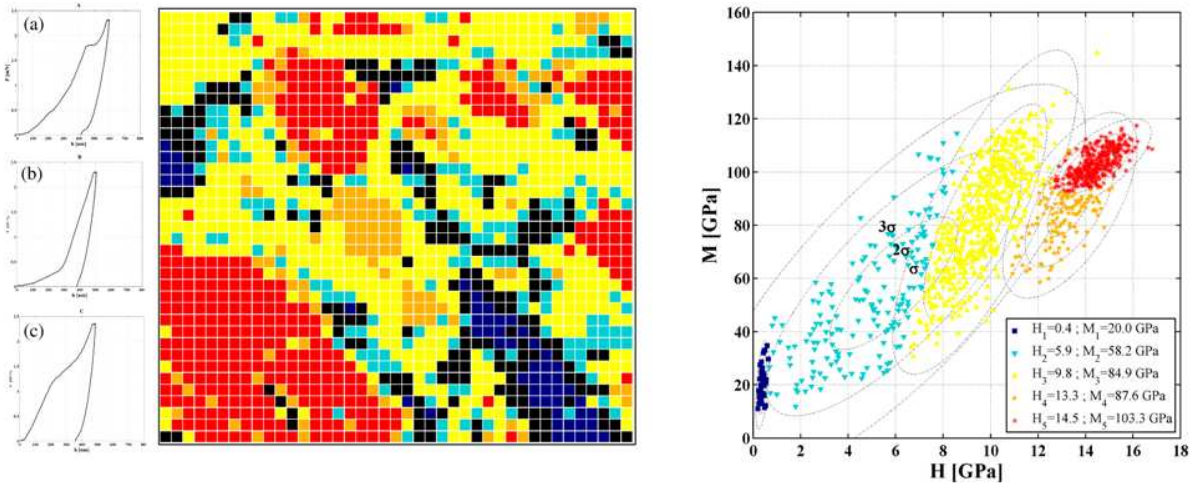

(d) (e)

Figure II.13 Filtering of experimental data: a,b,c) examples of abnormal load displacement curves, d) map of the identified phases with location of abnormal measurements (black phase), e) deconvolution of the grid dataset free of degenerated records.

The measured hardness of quartz is consistent with literature hardness $H_{(001)}$≈13÷14 [GPa].[34] Estimated mechanical properties of the 'glassy' matrix, H_3≈10 [GPa], M_3≈85 [GPa], are larger than values reported for soda-lime-silica glass (H≈6 [GPa], E≈70 [GPa]→M≈74 [GPa])[34] and fused silica (H≈8 [GPa], E≈72 [GPa]→M≈74 [GPa])[34]. On the other hand, comparing with the properties of aluminosilicate glass (H_V≈6 [GPa]→H≈6.5 [GPa], E≈89 [GPa]→M≈94 [GPa])[33] the hardness of matrix is still significantly higher, but its stiffness appears to be lower. These enhanced mechanical properties may be attributed to the presence of nano-crystals within the 'glassy' matrix as well as to the multi-component character of incorporated glass.[17,41] It is known that the incorporation of alkali oxides or iron, as well as reduction in silica content within the matrix may alter hardness and modulus of glass, e.g. basaltic glass (H≈8.6 [GPa], M≈97 [GPa]).[46,47]

Finally, it is worth mentioning that the resultant indentation (see Figure II.12(c)) depth h≈200 [nm] on the 'glassy' matrix phase activates an interaction volume of a characteristic size d=3h-5h=0.6-1.0 [μm].[48] Hence, d appears to be between three and five times larger that the nano-crystals of primary mullite, hematite and spinel, for which the maximum size of

observed crystals in sample B1 seems to be $d_0^1 \approx 200$ [nm], up to two times larger than the size of acicular crystals of secondary mullite $d_0^2 \approx 500$ [nm]. The secondary type is occasionally observed within large pockets of the 'glassy' matrix rich in alkaline impurities, causing excessive growth of this needle shaped form. Studies carried out by other researchers[17,41,42] confirm this observation, and specify the limiting size of primary mullite derived from kaolinite and muscovite clay as being <100 [nm], and as being <1 [μm] for secondary mullite. Given this size, it is unlikely that nanoindentation operated to a depth $h \approx 200$ [nm] will be able to actually probe 'pure' properties of primary or secondary mullite, as well as glass, but rather a composite response that may include effects of fine-scale porosity.

II.4. DISCUSSION

The complexity of clay brick microstructure requires the use of a multi-technique approach to identify the link between chemical and mineralogical composition, microstructure and mechanical performance. The results presented in this paper provide new insight into the multi-level and multi-component morphology of these silica and alumina rich ceramic material systems, which can be associated with distinct materials scales (Figure II.14), as detailed next.

II.4.1. Level "0" (<10^{-6} [m])

A good starting point for the multi-scale structure of brick is the 'glassy' matrix phase, which manifests itself at sub-micrometer scales in form of neo-crystals of mullite, γ-Al_2O_3 spinel-type phase and other accessory minerals. Such crystals, qualitatively identified with XRD, may reach hundreds of nanometers in size. As the SEM microscopy study on chemically etched sections revealed, these crystals are present in different geometrical forms, from cubic structures like in case of primary mullite and hematite, to acicular forms in the case of secondary mullite. These crystals are hosted by an amorphous phase and form a nano-composite with chemical and mechanical similarity to aluminosilicate glass with addition of alkaline oxides, as revealed by EDX analysis and instrumented grid indentation. Such a composite tends to develop upon the application of temperatures significantly above 950 [°C] and is present in the microstructure of the facing brick type B1. For lower temperatures, dehydroxylated muscovite was still observed in the diffraction spectra of B2 brick, which suggests that the phase transformation was not completed. Further studies of this

material based on SEM micrographs confirm this hypothesis, exposing significant fraction of residual, partially molten clay particles assembled in aggregates, next to the initial ‘glassy’ melt. So observed clay aggregates within B2 sample tend to form ‘grains’ defined here as ‘grains type A’, whereas the early developed polycrystalline-amorphous matrix in the regions of high chemical potential are specified as ‘grains type B’ (Figure II.14).

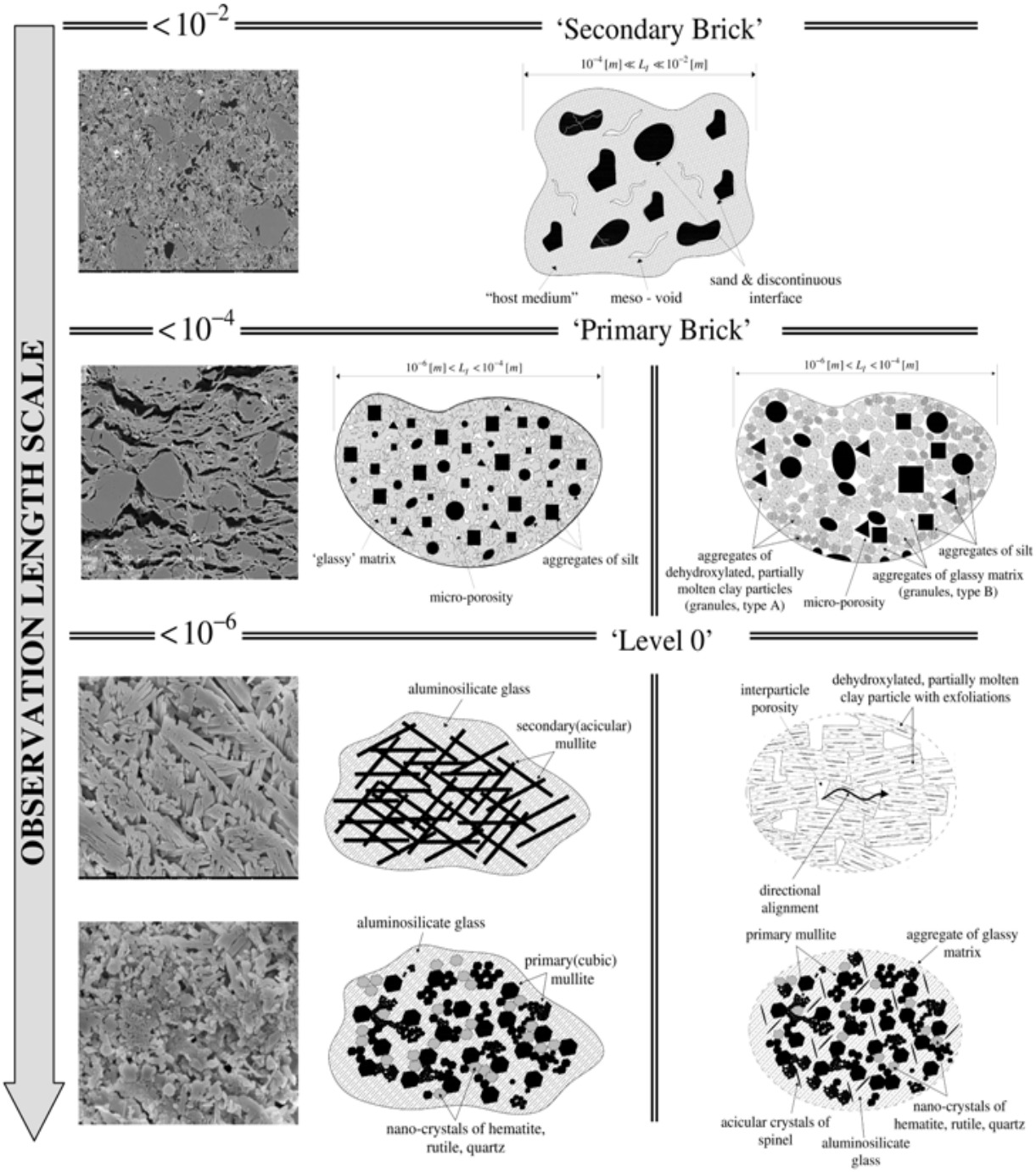

Figure II.14 Hierarchical think-model of facing clay brick B1 (T≈1050 [°C] (left)) and common brick B2 microstructures (T≈950 [°C] (right)).

II.4.2. Level "I": Primary Brick (<10^{-4} [m])

At sub-millimeter scale, matrix and porosity form a porous composite material whose behavior drives much of the macroscopic performance of clay brick materials. We therefore coin this scale as the "Primary Brick" scale. Depending on processing temperature and level "0" morphology, the structure of the "Primary Brick" may possess either a disordered granular morphology or a continuous matrix morphology with pore inclusions: the granular morphology is characteristic of brick B2, composed of level "0" grains (type A and B) and silt particles; a continuous matrix morphology is characteristic of the high-temperature fired facing brick B1, which possesses a continuous polycrystalline-amorphous binding matrix with silt and pore inclusions. These two morphological forms are inherently related to the porosity that dominates this scale, and which, according to results of MIP, DIA and gravimetric methods, may occupy up to one-third of the bulk material.

MIP and DIA results indicate that the micro-porosity spans a large range of scales from hundreds of nanometers to tens of micrometers, with modes clearly defined. A broad pore distribution is present in sample B2, which was produced at a temperature close to the melting temperature. The clear modes in the pore-size distributions are indicative of a coarse porosity development that can be attributed to the proximity of the firing temperature and the melting temperature. On the other hand, a significant fraction of fine voids is also found reminiscent of an inter-granular porosity incorporated between the remnants of clay particles.

Another important feature, which is encountered in this morphology, is the preferential orientation of voids, which are rarely spherical. This feature of the porosity is attributed to the extrusion technique employed to shape the brick at its green stage. In fact, forming of the material in the extruder tends to align irregular particles and to alter the form of originally spherical voids. As a result, the coarse porosity that builds up on the expense of smaller void coalescence tends to align along the extrusion direction, which affects physical and mechanical properties at macro-level. This alteration has been independently demonstrated in water absorption tests and macro-mechanical tests, in which the capillary water uptake, the Young's modulus and the strength, measured along the different material axes, show strong evidence of a macroscopic anisotropic behavior.

II.4.3. Level "II": Secondary Brick (<10^{-2} [m])

The top level of the proposed hierarchical material description is defined by the "Secondary Brick" structure, which is common for both materials B1 and B2. At this sub-centimeter scale, the "Primary Brick" composite hosts fractured grains of coarse sand,

discontinuous interface and possibly meso-voids. The discontinuity at the interface of the sand particles can be attributed to the thermal mismatch between host matrix and sand (mostly quartz) grains.

II.5. CONCLUSIONS

It has been demonstrated, that extruded clay brick is a complex ceramic system with a hierarchical microstructure. The multi-scale nature of this composite can be dissected into three scales: *Level "0"* ($<10^{-6}$ [m]), "*Primary Brick*" ($<10^{-4}$ [m]) and "*Secondary Brick*" ($<10^{-2}$ [m]). Depending on the brick firing temperature, the level "0" represents the nano-composite of 'glassy' matrix or assembly of dehydroxylated, partially molten clay aggregates and initial melt. The 'glassy' matrix tends to develop in the brick fired at temperatures significantly above melting temperature of the raw clay minerals. This temperature assures the formation of the amorphous binding phase, as well as crystallization of primary and secondary mullites, hematite and other accessory minerals in the nanometers size, as revealed by XRD and SEM micrographs studies. These crystal phases tend to enhance the hardness of the 'glassy' matrix; but it leaves the measured elastic properties in close proximity to that of the aluminosilicate glass, as demonstrated by instrumented grid indentation technique. The structure of "Primary Brick" is defined at sub-millimeter scale, where matrix, silt and porosity form a porous composite, whose behavior drives much of the macroscopic mechanical and physical performance of extruded brick. Depending on both, the morphology at level "0" and the processing temperature, the structure of the "Primary Brick" exhibits either a granular morphology or continuous matrix morphology with pore inclusions. The granular morphology with finer micro-porosity prevails when the firing temperature approaches the melting temperature, whereas the continuous morphology with coarser voids is inherent to bricks fashioned at significantly higher temperatures. Due to shaping technology of the green brick by extrusion, the micro-porosity exhibits a preferential orientation along the extrusion direction. Therefore, the water suction along this specific path is significantly enhanced compared to the other two orthogonal directions. A similar trend has been observed for the modulus of elasticity and strength, and suggests that extruded brick at macroscopic level follows (at least) transverse isotropy. The top level in the proposed hierarchical description represents the structure at sub-centimeter scale of "Secondary Brick". The fractured coarse aggregates of sand, as well as peripheral cracks at the interface of the coarse

particles and the composite represented by “Primary Brick” are the main microstructural features at this material scale.

The results of the multiscale technique thus applied to brick shed new light on the complex interplay at multiple scales between composition, processing and macroscopic performance of masonry materials. This should make it possible, in the close future, to fine tailor this omnipresent construction material for specific use and performances.

II.6. REFERENCES

[1]H. Reh, “Current classification of ceramic materials,” pp. 39-62 in Extrusion in ceramics, Engineering Materials and Processes. Edited by F. Händle. Springer-Verlag Berlin Heidenberg (2007).

[2]P. B. Lourenço, Computational strategies for masonry structures, Doctoral Thesis, Delft University of Technology (1996).

[3]G. Constantinides, Invariant mechanical properties of calcium-silicate-hydrates (C-S-H) in cement-based materials: Instrumented nanoindentation and microporomechanical modeling, Doctoral Thesis, Massachusetts Institute of Technology (2006).

[4]F.-J. Ulm, M. Vandamme, C. Bobko, J. A. Ortega, K. Tai, C. Ortiz, “Statistical Indentation Techniques for Hydrated Nanocomposites: Concrete, Bone and Shale,” J. Am. Ceram. Soc., 90 2677-2692 (2007).

[5]G. W. Brindley, G. C. Brown, Crystal structures of clay minerals and their X-ray identification, Mineralogical Society of Great Britain & Ireland (1984).

[6]V. K. Pecharsky, P. Y. Zavalij, Fundamentals of powder diffraction and structural characterization of materials, Springer (2005).

[7]G. W. Brindley, M. Nakahira, “The Kaolinite-Mullite reaction series: III, the high temperature phases,” J. Am. Ceram. Soc., 42 319-324 (1959).

[8]B. Sonuparlak, M. Sarikaya, I. A. Aksay, “Spinel phase formation during 980°C exothermic reaction in the Kaolinite-to-Mullite reaction series,” J. Am. Ceram. Soc., 70 837-42 (1987).

[9]K. Srikrishna, G. Thomas, R. Martinez, M. P. Corral, S. de Aza, J. S. Moya, “Kaolinite-mullite reaction series: a TEM study,” J. Mater. Sci., 25 607-612 (1990).

[10]S. G. Barlow, D. A. C. Manning, “Influence of time and temperature on reactions and transformations of muscovite mice,” Br. Ceram. Trans., 98 122-126 (1999).

[11]M. Dondi, M. Marsigli, I. Venturi, “Microstructure and mechanical propoerties of clay bricks: comparison between fast firing and traditional firing,” Br. Ceram. Trans., 98 12-18 (1999).

[12]G. Cultrone, E. Sebastián, K. Elert, M. J. de la Torre, O. Cazalla, C. Rodriguez-Navarro, “Influence of mineralogy and firing temperature on the porosity of bricks,” J. Eur. Ceram. Soc., 24 547-564 (2004).

[13]A. J. Garratt-Reed, D. C. Bell, Energy-dispersive X-ray analysis in the electron microscope, Microscopy Handbook 49, Taylor & Francis (2005).

[14]N. Otsu, “A threshold selection method from grey level histograms,” IEEE Trans. Syst. Man Cybern, SMC-9 62-66 (1979).

[15]M. Sezgin, B. Sankur, “Survey over image thresholding techniques and quantitative performance evaluation,” J. Electron. Imaging, 13 146-65 (2004).

[16]W. Burger, M. J. Burge, Digital image processing: an algorithmic introduction using Java,”Texts in Computer Science, Springer (2007).

[17]C. Rodriguez-Navarro, G. Cultrone, A. Sanchez-Navas, E. Sebastian, “TEM study of mullite growth after muscovite breakdown,” Am. Mineral., 88 713-24 (2003).

[18]C. J. McConville, W. E. Lee, “Microstructural development on firing illite and smectite clays compared with that in kaolinite,” J. Am. Ceram. Soc., 88 2267-2276 (2005).

[19]K. Devineau, B. Devouard, F. Villieras, F. Faure, J.-L. Devidal, A. Kohler, “Evolution of product phase assemblabes during thermal decomposition of muscovite under strong disequilibrium conditions,” Am. Mineral., 91 413-424 (2006).

[20]ASTM C67-09 Standard test methods for sampling and testing brick and structural clay tile, American society for Testing and Materials (2009).

[21]ASTM D4404-84 Standard test method for determination of pore volume and pore volume distribution of soil and rock by Mercury Intrusion Porosimetry, American society for Testing and Materials (2004).

[22]O. Delbrouck, J. Janssen, R. Ottenburgs, P. Van Oyen, W. Viaene, “Evolution of porosity in extruded stoneware as a function of firing temperature,” Appl. Clay Sci., 8 187-192 (1993).

[23]A. B. Abell, K. L. Willis, D. A. Lange, “Mercury Intrusion Porosimetry and image analysis of cement-based materials,” J. Colloid and Interface Sci., 211 39-44 (1999).

[24]R. Bartusch, F. Händle, “Laminations in Extrusion,” pp. 205-231 in Extrusion in Ceramics, Engineering Materials and Processes. Edited by F. Händle. Springer-Verlag Berlin Heidenberg (2007).

[25]Ch. Hall, W. D. Hoff, Water transport in brick, stone and concrete, Spon Press (2002).

[26]Y. M. Ito, M. Rosenblatt, L. Y. Cheng, F. F. Lange, A. G. Evans, "Cracking in particulate composites due to thermomechanical stress," Int. J. Fract., 17 483-91 (1981).

[27]S. R. Braganca, C. P. Bergmann, H. Hübner, "Effect of quartz particle size on the strength of triaxial porcelain," J. Eur. Ceram. Soc., 26 3761-68 (2006).

[28]ASTM C39/C39M-09a, Standard test method for compressive strength of cylindrical concrete specimens, American society for Testing and Materials (2009).

[29]D. V. Oliveira, P. B. Lourenço, P. Roca, "Cyclic behaviour of stone and brick masonry under uniaxial compressive loading," Mater. Struct., 39 219-27 (2006).

[30]W. F. Hosford, Mechanical behavior of materials, Cambridge University Press (2005).

[31]A. Fischer-Cripps, Nanoindentation, Springer Verlag, New York (2003).

[32]G. Constantinides, K. S. R. Chandran, F.-J. Ulm, K. J. Van Vliet, "Grid indentation analysis of composite microstructure and mechanics: Principles and validation," Mater. Sci. Eng. A-Struct. Mater. Properties Microstruct. Process., 430 189-202 (2006).

[33]I. J. McColm, Ceramic Hardness, Plenum Press, New York (1990).

[34]W. C. Oliver, G. M. Pharr, "An improved technique for determining hardness and elastic modulus using load and displacement sensing indentation experiments," J. Mater. Res., 7 1564-83 (1992).

[35]W. C. Oliver, G. M. Pharr, "Measurements of hardness and elastic modulus by Instrumented Indentation: Advances in understanding and refinements of methodology," J. Mater. Res., 19 3-20 (2004).

[36]M. Vandamme, F.-J. Ulm, F. Fonollosa, "Nanogranular packing of C-S-H at substochiometric conditions," Cem. Concr. Res., 40 14-26 (2010).

[37]D. M. Titterington, A. F. M. Smith, U. E. Makov, Statistical analysis of Finite Mixture Distributions, Wiley Series in Probability and Mathematical Statistics, John Wiley & Sons (1985).

[38]G. J. McLachlan, D. Pell, Finite Mixture Models, Wiley Series in Probability and Statistics, Wiley-Interscience Publication (2000).

[39]A. P. Dempster, N. M. Laird, D. B. Rubin, "Maximum likelihood from incomplete data via the EM algorithm," J. Roy. Stat. Soc. B Met., 39 1-38 (1977).

[40]EMMIX code webpage, http://www.maths.uq.edu.au/~gjm/emmix/emmix.html.

[41]Y. Iqbal, W. E. Lee, "Fired porcelain microstructures revisited," J. Am. Ceram. Soc., 82 3584-90 (1999).

[42]W. E. Lee, G. P. Souza, C. J. McConville, T. Tarvornpanich, Y. Iqbal, "Mullite formation in clays and clay-derived vitreous ceramics," J. Eur. Ceram. Soc., 28 465-71 (2008).

[43]G. Schwartz, “Estimating the dimension of the model,” Ann. Statist., 6 461-64 (1978).

[44]P. Heyliger, H. Ledbetter, S. Kim, “Elastic constants of natural quartz,” J. Acoust. Soc. Am., 114 644-50 (2003).

[45]J. J. Vlassak, W. D. Nix, “Measuring the elastic properties of anisotropic materials by means of indentation experiments,” J. Mech. Phys. Solids, 42 1223-1245 (1994).

[46]N. Lonnroth, Ch. L. Muhlstein, C. Pantano, Y. Yue, “Nanoindentation of glass wool fibers,” J. Non-Cryst. Solids, 354 3887-95 (2008).

[47]C.-C. Lin, L. Liu, “Composition dependence of elasticity in aluminosilicate glasses,” Phys. Chem. Miner., 33 332-46 (2006).

[48]F.-J. Ulm, M. Vandamme, H. M. Jennings, J. Vanzo, M. Bentivegna, K. J. Krakowiak, G. Constantinides, Ch. P. Bobko, K. J. Van Vliet, “Does microstructure matter for statistical nanoindentation techniques?,” Cem. Concr. Compos., 32 92-99 (2010).

III. Homogenized Material Response and the Distribution of the Indentation Modulus as a Geometrical Probability Problem. An Approach to Buckle's Rule of Thumb for Heterogeneous Materials

ABSTRACT

It this work the probabilistic approach is formulated in order to model the homogenization effect observed in the experimental grid indentation on heterogeneous solids. For this purpose, the simplified model microstructures of polycrystalline and fiber-reinforced materials are considered. Following the probabilistic partitioning of the region occupied by the bulk, the discrete distributions of the effective modulus are constructed. The influence of the characteristic length scale of the indentation interaction volume on the measured material response is investigated. The statistical homogenization and phase separation is discussed on the basis of results gathered from proposed analytical approach and Monte-Carlo simulations. Finally, the Buckle's principle for heterogeneous materials is validated.

III.1. INTRODUCTION

Recent developments in theoretical and experimental material science open new venues in the engineering and the design of complex material systems. Rapid advances of the measuring devices provide experimentalists with the access to the very refined structures of solids, whose characteristic scales differ by several orders of magnitude from the bulk observed at ordinary scale. Therefore, engineering of new high-tech materials, or commonly applied materials, is no longer restricted to the macro-level, but may be initiated at the smallest material scales, where the basic chemo-mechanical components can be identified. Such a micro-mechanics based approach becomes efficient and suitable to study heterogeneous materials (whether man-made, geological or biological) with different application purposes. Examples include omnipresent clay brick, concrete or wood as well as advanced composites, such as superconducting wires (Figure III.1) and fiber reinforced ceramic composites (Figure III.2).

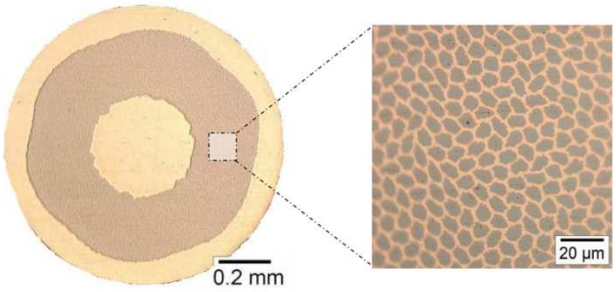

Figure III.1 Binary metal-matrix metal-filament composite *Nb-Ti*/*Cu* superconducting (SC) wire used for the fabrication of accelerator magnet coils in Large Hadron Collider (LHC), image adopted from Scheuerlein et al..[1]

The mentioned examples represent a quite broad spectrum of materials, even if they have one feature in common: the hierarchical ordering of the microstructure. Due to this fact, the bulk solid may be broken down to the material blocks representing specific morphologies. Each of such blocks is associated with a unique length scale $\mathscr{l}$, which in the mechanical sense manifests itself by different mechanical performance (stiffness and strength). To identify such material levels and link them to *in vivo* mechanical performance of the bulk, the combination of microscopy techniques and experimental mechanics is required. For this purpose, the implementation of the nano-science into material engineering science led to the development of the instrumented indentation method. This experimental method provides unprecedented

access to micro-mechanical properties of small material volumes, which could not be achieved in conventional tests as the common uniaxial compression or uniaxial tension tests.

The idea of the instrumented indentation method is simple: by pushing the hard probe of the indenter, the volume of the bulk beneath becomes deformed in a way governed by the mechanical properties of the solid. The indentation modulus, as well as the material hardness, are calculated on the basis of the *P-h* (indentation force-indentation depth) experimental curve.[2] The properties obtained are considered to represent the average quantities from the volume of the bulk activated by the probe, the so-called interaction volume. Therefore, the properties are valid at the length scale corresponding to the size of the interaction volume $d \approx 3h\text{-}4h$.[3] By changing the indentation depth *h*, the properties from the different material levels may be extracted, and all existing blocks can be properly classified in the mechanical sense. On the other hand, probing the material at different indentation depths, from macro toward micro and nano-scale, allows continuous monitoring of the variation of the considered material parameters. As a consequence the homogenization process (or upscaling) within the heterogeneous solids can be observed directly in the test. However, in order to fulfill the goal of identifying the structural blocks and measure the inherent properties at some well defined material scale, the proper choice of the suitable indentation depth is required.

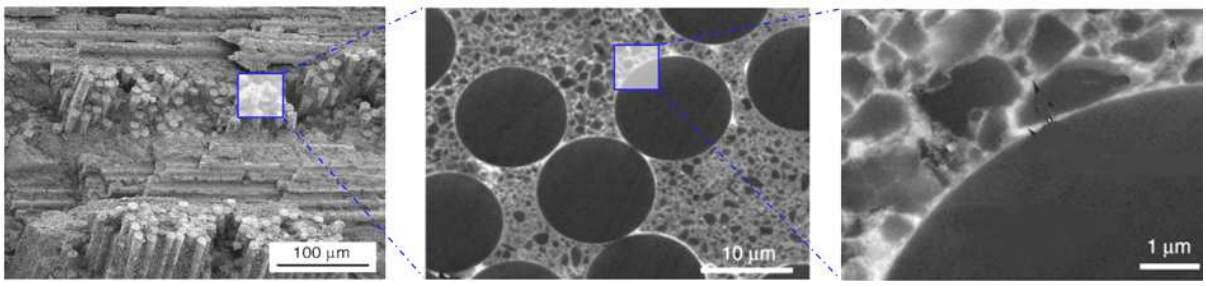

Figure III.2 Hierarchical microstructure of the continuous-fiber ceramic composite, adopted from Zok.[4]

Heterogeneous material, by definition, represents a complex system, where the features of diverse origins, forms and size may be incorporated with different volume fractions. Therefore, to minimize the interference of the other structural blocks in the measured parameters, and to be certain that the parameters are inherent characteristics of the identified phase, this choice is of crucial importance.

A common approach to this problem is the rule known as 1/10 or Buckle's rule of thumb originally proposed for the system of a thin film on a substrate.[5] This principle, extended further to heterogeneous materials, states that in order to assess the inherent phase properties,

the indentation depth h should be at most 1/10 of the characteristic size of the microstructure D.[6] Above this limit, and when the mismatch in the phase properties of the substrate E_s and of the film E_f is significant $E_s / E_f \notin [0.2;5]$, the interference is likely to occur and the composite response may prevail. This hypothesis has been extensively used in the instrumented indentation of multi-scale and multi-component materials providing satisfactory results.[7] However, to the knowledge of the author, its analytical proof has lacked behind, except in the case of a thin film on a substrate.[8,9] Therefore, the work presented here contributes to fill this gap and validates the 1/10 principle for the case of heterogeneous solids, in the framework of linear elasticity and probability theory. To achieve this goal, the real indentation experiment on a composite material has been discretized to a form that provides a relatively clear and simple mathematical description.

Accordingly, the interaction volume is modeled as a cubic form with characteristic size d, the composite materials represent idealistic heterogeneous solids and the effective elastic modulus follows the law of mixture. Under these assumptions, the partitioning in the probabilistic sense is carried out on the domain of the bulk. Each of such subsets represents the location of the interaction volume of size d, for which the random variable E_{ff} takes the values in the prescribed limits. At transient given d value, varying from the size approaching zero to the scale of the representative cell D (analogy with the observation window), the discrete distribution of probability masses is calculated. The evolution of the discrete probability distributions with respect to the characteristic length of the interaction volume describes the homogenization effect in the statistical sense and in the framework of the proposed methodology. Likewise, in the real experiment, the separation of the phases or convergence towards a unified material response may be reproduced. Therefore, the relation between the characteristic length scale D and the indentation depth h permits to evaluate the Buckle's principle applied to model microstructures. The analytical approach presented next is strengthened with the results of a Monte-Carlo simulation, which provides access to the homogenization (separation) at scales much above the scale of the Representative Elementary Volume (REV) for multi-phase materials.

III.2. MODELS FOR HETEROGENEOUS MATERIALS

The two adopted model microstructures represent commonly encountered morphologies in composite materials. The checker-board model (Figure III.3(a)) is an idealization of the

polycrystalline type solid, while the fiber reinforced composite material has been approached with the fiber-board model (Figure III.3(b)).

It is known that polycrystalline materials, e.g. metals, by definition are made up of grains 'stuck' together by grain boundaries. Grains come in diverse shapes and sizes, which are strongly affected by the processing conditions and elemental composition.[10] Due to this complexity, severe simplifications have been done regarding the size, as well as the shape of the grains, so that the problem is treatable in the context of this work. Therefore, each phase is considered isotropic, the grains have cubic form and the grains are distributed in a periodic manner providing equal volume fractions. The second model represents a biphasic composite material with the fibers embedded in the continuous matrix. In this fiber-matrix morphology both constituents are assumed isotropic, and the case of perfect interface bond is considered. Embedded fibers feature a common circular section and the same direction of alignment. As a result of the assumptions made, the randomness of the heterogeneities in both morphologies became suppressed, creating deterministic microstructures.

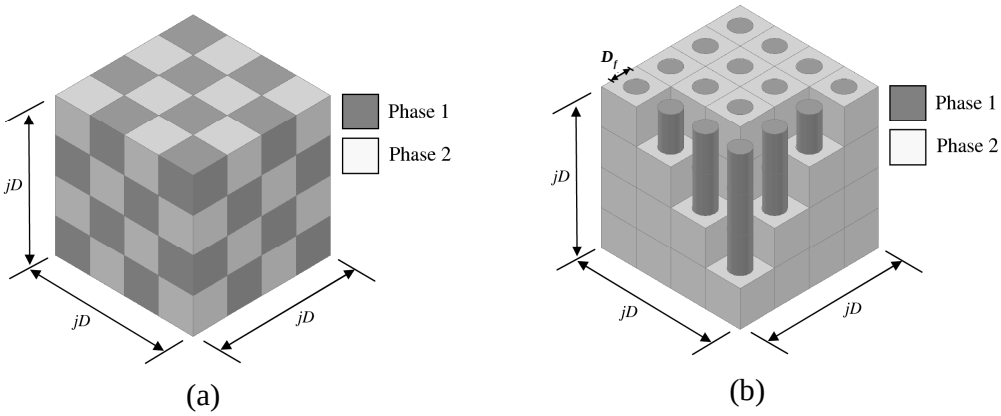

Figure III.3 Investigated model microstructures: a) idealization of the polycrystalline morphology represented by a checker board model, b) idealization of the fiber reinforced composite morphology represented by a fiber-board model. Note that the cell considered has *j* times the size of a characteristic length *D*.

III.3. DEFINITION OF THE EXPERIMENTAL PROCEDURE

The virtual indentation experiment is carried out on the material model defined on the fixed region $\mathcal{R}_0 = \mathcal{R}_1 + \mathcal{R}_2$ in $\mathcal{R}^3$ Euclidean space, which may be finite or infinite and is occupied by a continuously distributed, biphasic composite material (Figure III.4(a)). Both incorporated phases, which occupy $\mathcal{R}_1$ and $\mathcal{R}_2$ respectively, are considered isotropic and

linear elastic, however with distinct stiffness properties $\boldsymbol{L}_1=(3K_1,2\mu_1)$ and $\boldsymbol{L}_2=(3K_2,2\mu_2)$, where the subscripts *1* and *2* indicate the phases. The symbolic notation for fourth-order isotropic stiffness tensors $\boldsymbol{L}$ (Eq. III.1) in terms of bulk $K=E/3(1-2\mu)$ and shear $\mu=E/2(1+\nu)$ moduli has been adopted.[11] The division of the body volume among the phases follows the condition $c_1+c_2=1$, where c_i stands for the volume fraction of *i-th* phase.

$$\mathbf{L} = 3K\mathbf{I}^h + 2\mu\mathbf{I}^d \Rightarrow \mathbf{L}(3K, 2\mu) \qquad \text{III.1}$$

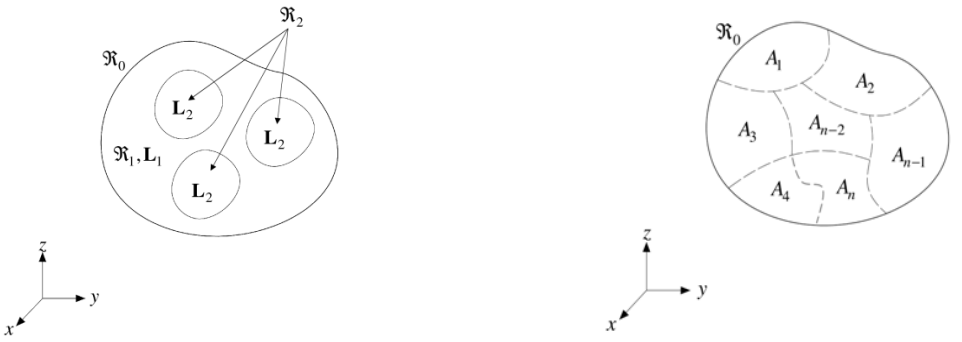

(a) (b)

Figure III.4 Model of a biphasic material (a), division of $\mathfrak{R}_0$ into discrete sets of the points in $\mathfrak{R}^3$ Euclidean space (b).

The trial of statistical experiment $\mathfrak{D}$ includes three stages. In the first stage a random point $O(x,y,z)$ is drawn from the region $\mathfrak{R}_0$. Next, the fictitious indentation interaction volume is placed in a way that its center is located at $O(x,y,z)$. The interaction volume is assumed to be of cubic form with the characteristic length scale d. Finally, the volume fraction c_1 of *Phase 1* bounded within the interaction cube is estimated and used for the calculation of the effective modulus of elasticity E_{eff} according to the Voigt upper bound solution (Eq. III.2). These two random variables are the outcomes of a single trial of the experiment. In order to construct the relative frequency diagram of the later random variable, which is one of the main objectives of this study, the experiment $\mathfrak{D}$ is repeated sufficiently large number of times $N\rightarrow\infty$, and the gathered results are sorted into the user specified mutually exclusive intervals, bins. The adopted procedure tends to mimic the real indentation experiment, in which the independent measurements are taken in the nodal points of a large indentation grid.

$$E_{eff} = c_1E_1 + c_2E_2 \qquad \text{III.2}$$

This strategy has been applied in the virtual indentation study based on 3D images of an idealized two-phase material as well as in images of hardened cement paste (HCP) acquired

by focused ion beam nanotomography (FIB-nt).[12] However, in the present research work, rather than using a computer code like in the mentioned reference, an alternative procedure, which leads to an analytical solution is proposed and is used to study the homogenization effect in the grid indentation technique.

The procedure to follow relies on the concept of partition of region $\mathfrak{R}_0$ into the finite number of subsets $\mathcal{A}_1, \mathcal{A}_2, \ldots, \mathcal{A}_m$, where $m \geq 3$ is a odd natural number (Figure III.4(b)). Such a partition $\mathcal{H}=[\mathcal{A}_1, \mathcal{A}_2, \ldots, \mathcal{A}_m]$ is considered to be a collection of mutually exclusive subsets $\mathcal{A}_i$, meaning that any two arbitrary sets within $\mathcal{H}$ have no common element, and theirs union equals $\mathfrak{R}_0$ (Eq. III.3).[13]

$$\mathcal{A}_1 + \mathcal{A}_2 + \ldots + \mathcal{A}_m = \mathfrak{R}_0 \qquad \mathcal{A}_i \mathcal{A}_j = \{\varnothing\} \;\; i \neq j \tag{III.3}$$

A subset $\mathcal{A}_i$ of $\mathcal{H}$ includes all elementary events ω (points $O(x,y,z) \in \mathfrak{R}_0$), such that the experimental realization of the random variable $C(\omega)$ falls into the corresponding interval l_i or is constant $C(\omega)=c_0$, if $l_i=\{c_0\}$ where $c_0 \in \langle 0;1 \rangle$ (Figure III.5). In other words, the material that occupies $\mathfrak{R}_0$ is divided into the regions $\mathcal{A}_i$, such that the volume fraction c_1 of *Phase 1* within the interaction volume of size d whose center $O(x,y,z) \in \mathcal{A}_i$, varies within related interval l_i or may be independent from the location, if $C(\{\omega\} \in \mathcal{A}_i) = const.$.

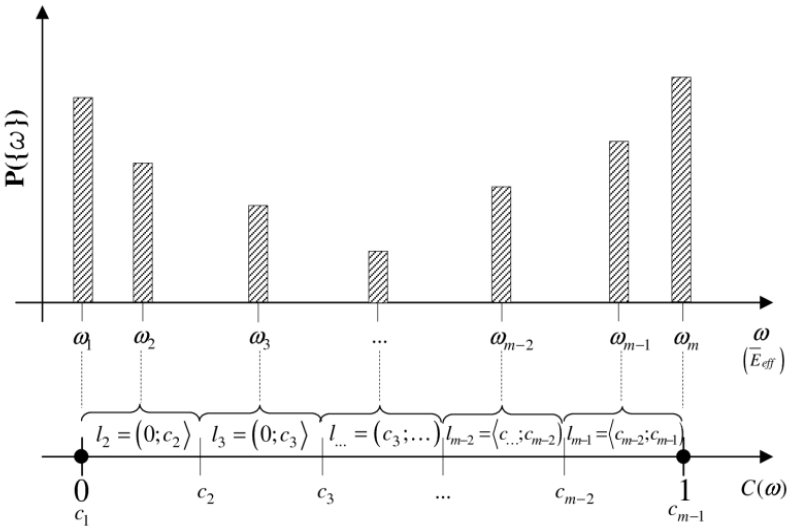

Figure III.5 Division of the domain of the random variable $C(\omega) \in \langle 0;1 \rangle$ into finite intervals with boundary values and distribution of probability masses $P(\{\omega\})$.

As a way of illustration of this concept, the partitioning of checkerboard material (Figure III.6(a)), as well as uniaxial fiber reinforced composite (Figure III.6(b)), are presented. In these two working cases the original material domains $\mathfrak{R}_0$ have been discretized into five subsets $\mathscr{H}=[\mathscr{A}_1,\mathscr{A}_2,\mathscr{A}_3,\mathscr{A}_4,\mathscr{A}_5]$. The first $\mathscr{A}_1=\{O\in\mathfrak{R}_0|C(\omega)=0\}$ and the last $\mathscr{A}_5=\{O\in\mathfrak{R}_0|C(\omega)=1\}$ sets represent the locations of the interaction volume, which is composed of pure *Phase 2* (c_1 = 0, white) or pure *Phase 1* (c_1 = 1, gray). As a consequence, the measured effective modulus within each of these regions is independent on the position and receives the value $E_{eff} = E_2$ in $\mathscr{A}_1$ and $E_{eff} = E_1$ in $\mathscr{A}_5$. The remaining subsets of $\mathscr{H}$ correspond to the locations of the interaction cube such that the volume fraction c_1 varies in the prescribed limits, l_2=(0;1/3⟩, l_3=(1/3;2/3⟩ and l_4=⟨2/3;1), respectively. Automatically, according to the definition of the effective modulus (Eq. III.2) the following intervals for measured effective moduli have been defined (Eq. III.4) for $\mathscr{A}_2,\mathscr{A}_3,\mathscr{A}_4$ subsets.

$$\{l_2^E, l_3^E, l_4^E\} = \{\left(E_2; \tfrac{2}{3}E_2 + \tfrac{1}{3}E_1\right\rangle, \left(\tfrac{2}{3}E_2 + \tfrac{1}{3}E_1; \tfrac{1}{3}E_2 + \tfrac{2}{3}E_1\right), \left\langle \tfrac{1}{3}E_2 + \tfrac{2}{3}E_1; E_1\right)\} \qquad \text{III.4}$$

At this point, it may be easily seen that in order to construct the relative frequency diagrams of random variables c_1 or E_{eff}, i.e. the probability of a random variable being an element of bin l_i shall be calculated. According to the classical definition,[13] the probability $P(\mathscr{L}_i)$ of an event $\mathscr{L}_i$, such that $O(x,y,z)\in\mathscr{A}_i$ or equivalently $C(\omega)\in l_i$, is given by the ratio $P(\mathscr{L}_i)=N_{\mathscr{L}_i} / N$, where N is the number of all outcomes of an experiment and $N_{\mathscr{L}_i}$ is the number of outcomes that are favorable to the event $\mathscr{L}_i$. Obviously, the number of possible outcomes that favor event $\mathscr{L}_i$ is infinite, and the volume V can be used as a measure of infinity. This leads to a probability of $\mathscr{L}_i$, which is the volume fraction $c_1\in l_i$, or effective moduli $E_{eff}\in l_i^E$, measured within the interaction volume of length d,, and whose center is drawn at random from region $\mathfrak{R}_0$ of biphasic material, given by the ratio $P(\mathscr{L}_i)=N_{\mathscr{L}_i} / N$. Here $V_{\mathscr{L}_i}$ is the volume occupied by the subset $\mathscr{A}_i$, and V is the total volume of the composite material.

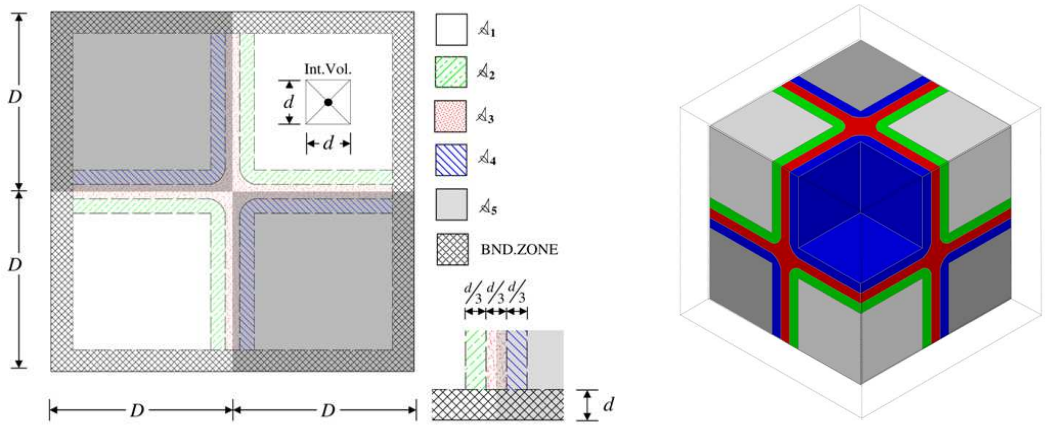

(a)

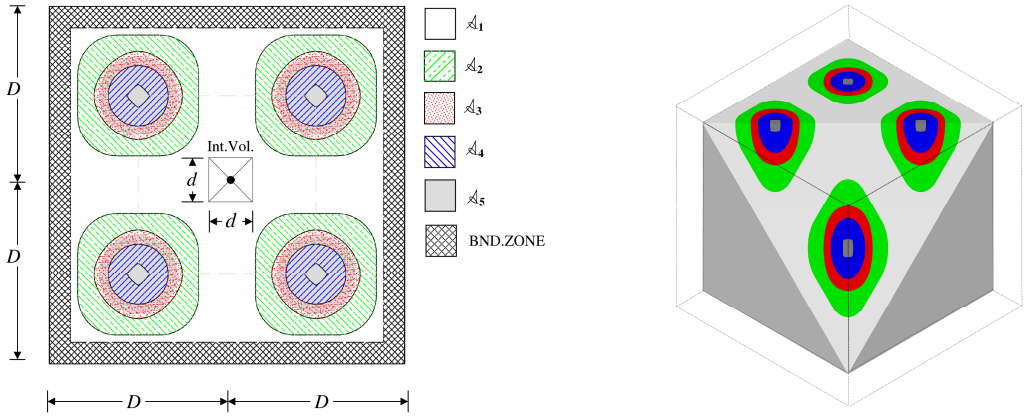

(b)

Figure III.6 Planar and isometric views of the partition scheme of model biphasic materials ($E_2 < E_1$) into five disjoint subsets m=5: a) checker-board material, b) uniaxial fiber reinforced material. Regions labeled $\mathcal{A}_1$ (*Phase 2*, $E_{eff} = E_2$), $\mathcal{A}_2$ ($E_{eff} \in l_2^E$), $\mathcal{A}_3$ ($E_{eff} \in l_3^E$), $\mathcal{A}_4$ ($E_{eff} \in l_4^E$), $\mathcal{A}_5$ (*Phase 1*, $E_{eff} = E_1$).

III.3.1. Cubic Indentation Interaction Volume Assumption

Another simplification in the present study is that the indentation interaction volume is assumed to take the cubic form. This assumption implies that the entire material within the cubic volume exhibits the same strain field. Hence, the elastic modulus follows the law of mixture or Voigt upper bound solution expressed by Eq. III.2. However, it is known from the solutions of theory of elasticity and contact mechanics that the real strain and stress fields, which arise due to contact of the solid with the rigid probe, are far more complex.[14,15]

As an example, the indentation stress fields for conical indentation within the elastic solid are presented below (Figure III.7(a-c)). Based on this solution, it is easily seen that the stress within the interior diminishes gradually into the bulk of the solid and along the radial direction following spherical trajectories.

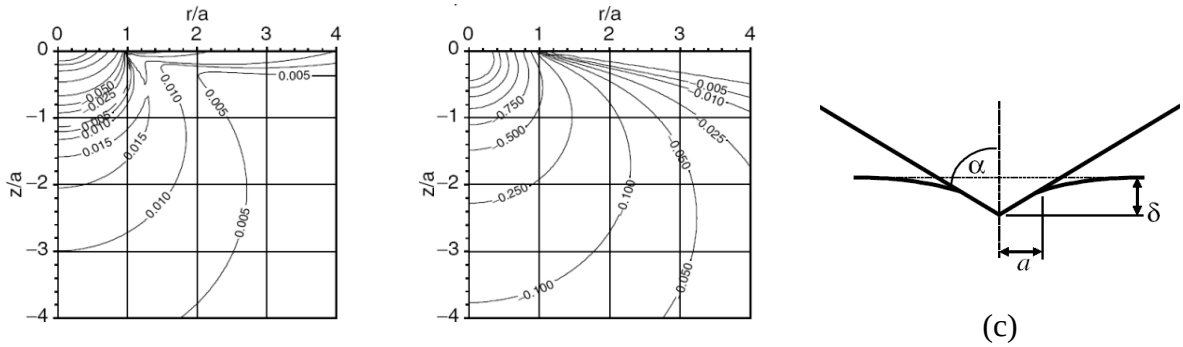

(a) (b) (c)

Figure III.7 Elastic stress fields provoked by the conical indentation on a homogeneous and isotropic solid calculated for Poisson's ratio $\nu = 0.26$, an indention angle α and an indention depth δ: a) σ_1 principal stress trajectories, b) σ_3 principal stress trajectories and c) representation of indentation geometry, adopted from Fischer-Cripps.[14] Radial distance r and vertical distance z are normalized to the contact radius a. The stress is expressed in terms of the mean contact pressure p_m.

The strain and the strain energy fields follow similar trends, suggesting a more realistic representation of the interaction volume in the form of a hemisphere. Additionally, due to variation of the mentioned elastic fields, the material beneath the indenter probe does not contribute to the 'effective' material response in the same way as the material from the lower levels of the exited volume of the bulk.[16] Therefore, a weighting function would be required in order to take this effect into account. Being aware of the nature of the interaction volume and the possible impact of the adopted simplification on the 'effective' response, the cubic form has still been adopted as a first order approximation due to its simplicity.

III.4. ANALYSIS OF EXPERIMENTAL RESULTS

III.4.1. Checkerboard Microstructure

The example of the partitioning of the checkerboard microstructure into five subsets has been pictured on Figure III.6(a). However, a formulation to calculate the discrete probabilities

P_i for arbitrary odd partitions $\mathscr{H}=[\mathscr{A}_1,\mathscr{A}_2,\ldots,\mathscr{A}_m]$, where m=3,5,7,…, is derived next. Consider a checkerboard microstructure with checker size D, such that its total length is jD (Figure III.3(a)). Assuming the number of checkers per edge is an even number j, the volume fraction of each phase is 50 %. Hence, the volume occupied by biphasic material and available for testing with an interaction cube of size d is $V(d)=(jD-d)^3$. The so-called 'testing volume' approaches the total volume $V=(jD)^3$ of $\mathscr{R}_0$ in the limiting case $V = \lim_{d \to 0} V(d)$.

The volume of each phase incorporated into the material model is $V_1(d)=V_2(d)=0.5j^3(D-d)^3$. In the next step, the volume corresponding to each of the sets within partition $\mathscr{H}$ and linked to the composite response is calculated. This fraction of the material may be divided into three structural building blocks (Figures III.8(a-c)). The first block relates to the corner points, which are common for 8 checkers. In this block the portions of the volume corresponding to the subsets $[\mathscr{A}_2,\ldots,\mathscr{A}_{m-1}]$ are enclosed in the cube centered at the corner point with the length of the edge d (Figure III.8(a)). The division of this cubic volume among the influence zones is governed by the bounding surfaces $z=f(x,y)$ given by Eq. III.5(a), whose pictorial representation is outlined on Figures III.9(a-c).

$$z = f(x,y) = (\frac{1}{2} - \alpha)\frac{d^3}{4xy} \qquad \text{III.5(a)}$$

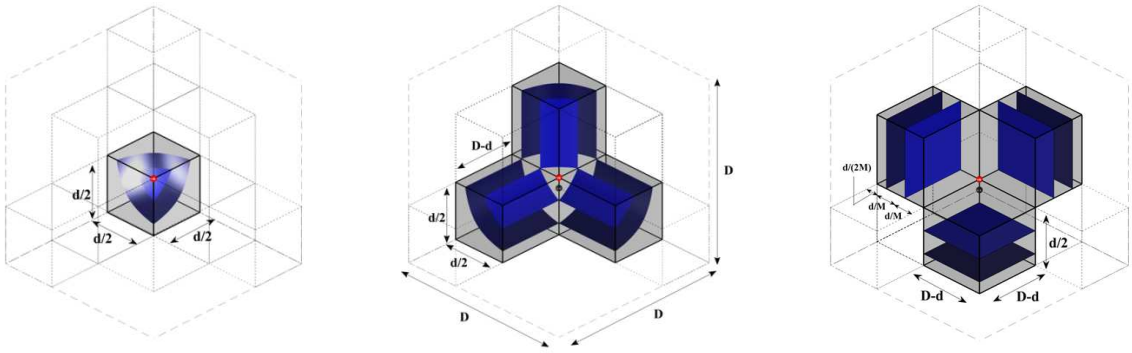

(a) (b) (c)

Figure III.8 Geometrical building blocks of the checker board composite zone partition, with the examples of the boundary surfaces z: a) corner point element, b) line element, c) face element.

The symmetry conditions permit to reduce the problem to one eight of the mentioned cubic volume, which is the sub-volume within a single checker. In the reduced problem, the

function $z=f(x,y)$ is given in the new coordinate system $\{\xi_1,\xi_2,\xi_3\}$ by Eq. III.5(b), with its origin translated from the corner point by the vector $\mathbf{v}=\left[\frac{1}{2}d;\frac{1}{2}d;\frac{1}{2}d\right]$ (see Figure III.9(a-c)), leading to:

$$\xi_3 = f(\xi_1,\xi_2) = \frac{\alpha d^3 - d^2(\xi_1+\xi_2) + 2d\xi_1\xi_2}{d^2 - 2d(\xi_1+\xi_2) + 4\xi_1\xi_2} \qquad \text{III.5(b)}$$

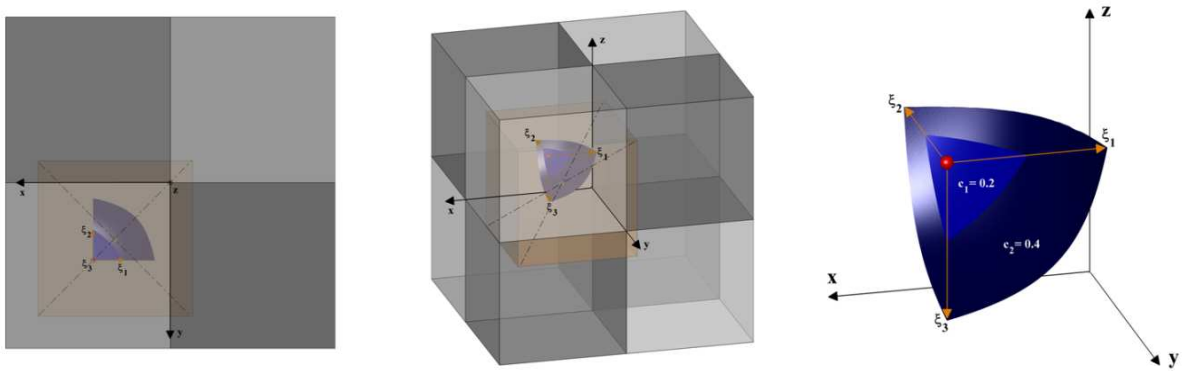

Figure III.9 Schematic representation of the surfaces of the constant volume fraction $z=f(x,y)$, within the 'checkers', seen in different perspectives. Surface $z=f(x,y)$ obtained for j=4, D=32 [μm], d=30 [μm], m=7. the light blue surface represents the locations $O(x,y,z)$ for which c_1=0.2, while dark blue surface corresponds to c_1=0.4.

The volume Q_i bounded by the $f(\xi_1,\xi_2|\alpha)$, and the planes $\pi_{\xi1,\xi2}$, $\pi_{\xi1,\xi3}$ and $\pi_{\xi3,\xi2}$ is given by Eq. III.6(a), where $i=2,3,\ldots,(m-1)/2$ and $M=(m-2)$.

$$Q_i = \iint_{\xi_1,\xi_2} f(\xi_1,\xi_2)d\xi_2 d\xi_1 \quad 0 \le \xi_1 \le \frac{(i-1)d}{M} \quad 0 \le \xi_2 \le \frac{d(\alpha d - \xi_1)}{d - 2\xi_1} \qquad \text{III.6(a)}$$

Based on this integral formula, the composite volumes of this structural block, corresponding to the given partition scheme, are given as:

$$V_i^I = 8N_I(Q_i - Q_{i-1}) \qquad \text{III.6(b)}$$

where $Q_1=0$, $Q_{(m+1)/2}=(d/2)^3$ and $N_I=(j-1)^3$ is a multiplication factor, which corresponds to the total number of corner points shared among eight checkers.

The second building block considered is a line element (see Figure III.8(b)), meaning that it is a sub-volume of the composite zone shared along the common line of four checkers.

Similarly, and due to existing symmetry, the calculations are reduced to the domain of one checker only. Therefore, the areas of the cross-sections of the line element blocks, which correspond to the sub-sets $[\mathcal{A}_2,\ldots,\mathcal{A}_{m-1}]$ are given for $i=2,3,\ldots,(m-1)/2$ as:

$$S_i = \int_{\xi_1} \frac{d(\alpha d - \xi_1)}{d - 2\xi_1} d\xi_1 \quad 0 \le \xi_1 \le \frac{(i-1)d}{M} \qquad \text{III.7(a)}$$

Consequently, the related volumes are calculated as a product of the area of the section and the actual length of the line element and read:

$$V_i^{II} = 4N_{II}(S_i - S_{i-1})(D-d) \qquad \text{III.7(b)}$$

where $S_1=0$, $S_{(m+1)/2}=(d/2)^2$ and $N_{II}=3j(j-1)^2$ is a multiplication factor that corresponds to the total number of edges shared among four checkers.

The last defined component is a face element (Figure III.8(c)). This building block is situated on the surface common for two adjacent checkers. Due to the symmetry, the single domain of the checker may be considered. The unknown volumes corresponding to the given partition of the composite zone are given below:

$$V_i^{III} = 2N_{III}\frac{d}{M}(D-d)^2 \qquad \text{III.8}$$

where $V^{III}_{(m+1)/2}=0.5N_{III}d(D-d)^2/M$ and $N_{III}=3j^2(j-1)$ is a multiplication factor, that corresponds to the total number of planes shared among two checkers.

This last component makes the solution complete, hence the appropriate final volumes may be calculated for each discrete set within the assumed partition by:

$$V_k = \frac{1}{2}(V_k^I + V_k^{II} + V_k^{III}) \qquad \text{III.9}$$

where $k=2,\ldots,(m-1)/2$, $V_1=0.5j^3(D-d)^3$, $V_{(m+1)/2}=(V^I_{(m+1)/2}+V^{II}_{(m+1)/2}+V^{III}_{(m+1)/2})$. The symmetry condition $V_i=V_{m+1-i}$ is adopted in order to resolve the solution for the entire $\mathcal{X}$. Finally, the desired discrete masses of probability that correspond to $[\mathcal{A}_1,\ldots,\mathcal{A}_{m-1}]$ are calculated according to the definition $P(\mathcal{L}_i)=V_{\mathcal{L}_i}/V$. The discrete distributions may be constructed now for any size of the interaction volume d within domain $\langle 0,D\rangle$ given an arbitrary, odd number of discrete intervals m (see Figures III.10(a-c)).

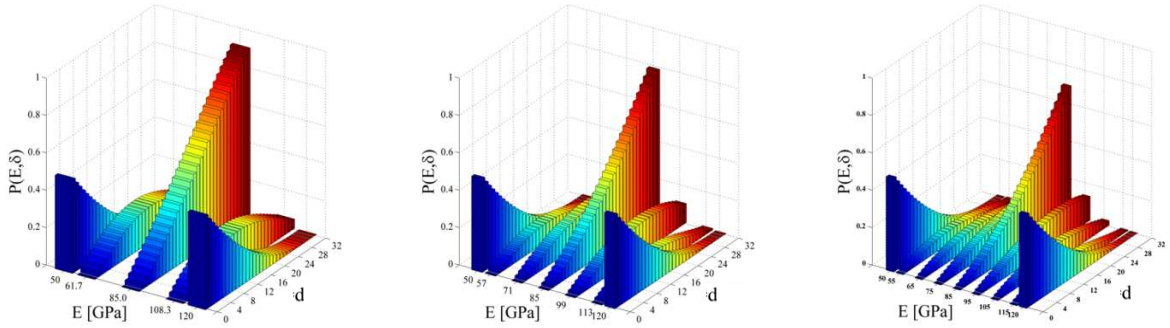

(a) (b) (c)

Figure III.10 Evolution of the discrete probability distribution of elastic modulus with respect to the interaction volume size *d* for checkerboard model for *j=4*: a) *m=5*, b) *m=7* and c) *m=9*. The assumed mechanical properties are: E_1=120 [GPa] for *Phase 1* and E_2=50 [GPa] for *Phase 2*, equal volume fractions $c_1=c_2=0.5$.

III.4.2. Unidirectional Fiber Composite Microstructure

The illustrative example of the partition scheme applied to the uniaxial fiber reinforced composite material has been outlined on Figure III.6(b). In this case, the problem of finding the probability masses corresponding to discrete partition $\mathscr{H}$ is independent of the fiber direction. As a result, the volume fraction may be replaced by the surface fraction in the plane normal to the axis of the alignment and used as an equivalent measure of the probability. Taking into account this simplification, the surface fraction of each subset $\mathscr{A}_i$ corresponding to the assumed partition $\mathscr{H}$ is calculated next.

At the local scale of a single cell (Figure III.11(a)) the subsets $\mathscr{A}_i$ are defined with the aid of the loci $B_{i-1,i}$, where $i=1,\ldots,m$ with *m* being the number of discrete subsets. Each, so defined locus represents the geometrical location of the center *O(x,y)* of the interaction volume *d*, for which the appropriate condition imposed on the bounded volume fractions is satisfied, e.g. loci B_{01} and B_{12} represent outer and inner sets of configurations of points *O(x,y)* whose coordinates satisfy condition c_f=0, where the subscript *f* indicates that the material is the fiber. The first mentioned contour is simply the square with the length of the edge *(D–d/2)*. The basic unit of the locus B_{12} is a composite line with three components: the segment *[0;d]* with the origin $(1/2(D_f+d);0)$, the segment *[d;0]* with the origin $(0;1/2(D_f+d))$ and the segment of the circular arch with radius $D_f/2$ and the center at *(d/2;d/2)* (Figure III.11(b)). The symmetry conditions are employed to complete and close this contour over the entire domain of the cell.

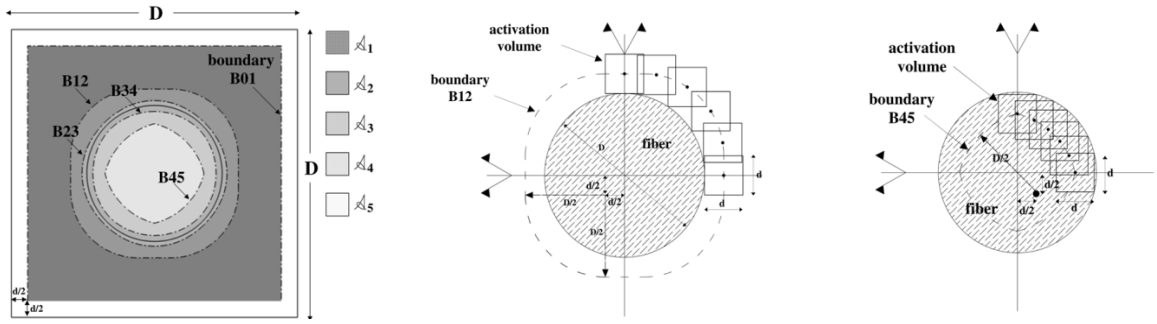

(a) (b) (c)

Figure III.11 Schematic representation of the unitary fiber cell and its partition into the discrete regions and boundaries (a), the pictorial definition of boundaries B_{12} (b) and B_{45} (c).

In the center of the *REV* lays the contour line B_{45}, which is a set of points $O(x,y)$ where c_f=1, meaning that the entire interaction volume is occupied by the fiber material only. In this case, the building block of the segment is a circular arch of radius $D_f/2$ and center at $(-d/2;-d/2)$, bounded in the first quarter of the coordinate system of the unit cell (see Figure III.11(c)). As usual, the conditions of symmetry are used to complete and close this contour line.

The discretization of the composite material response domain into a finite number of sub-regions is linked to the remaining internal contours, which in this particular case are defined as B_{23} and B_{34} (see Figure III.11(a)). These two contours represent the locations of the interaction volume corresponding to the specific proportions of incorporated fractions of the matrix and fiber materials. Therefore, the volume element with a center located at the first locus B_{23} fulfills the condition $c_f=1/3$, while the B_{34} satisfies the condition c_f=2/3 (see Figures III.12(a-b)).

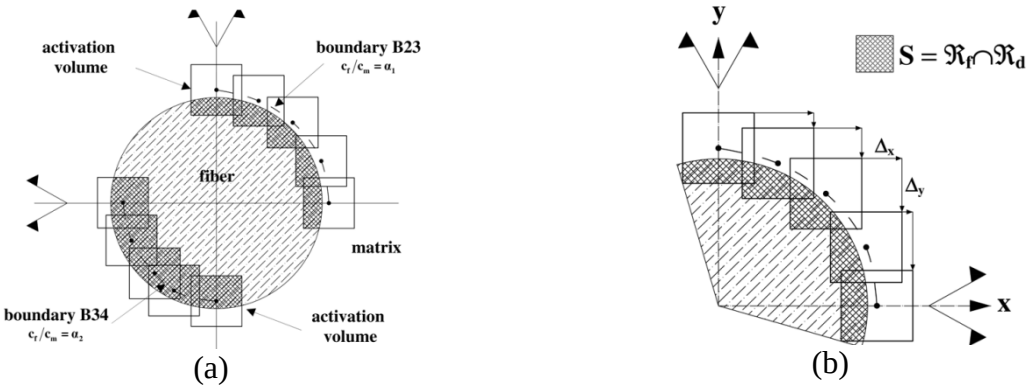

(a) (b)

Figure III.12 Schematic representation of the boundaries B_{23} and B_{34} corresponding to mixture response (a) and definition of translation vector with components (Δ_x, Δ_y) (b).

Such a discretization is a particular case that corresponds to the probability mass distribution with $m=5$, but in case of more refine division (higher number of discrete values) a more general condition for each locus may be defined $c_f=\alpha_i$, where $\alpha_i \in (0,1)$ depends on the division number m.

The calculation of this type of contour lines has been executed within the Matlab® programming environment, for which the appropriate code has been developed. In the first stage the interaction volume of size d is positioned with its center located at the y-axis and one of the edges tangents to the locus of the fiber. The appropriate vector of translation $(0,\Delta_y)$, and as a consequence $O(x,y)$, is found by solving the following equation:

$$\Delta_y \rightarrow S = \alpha_i d^2 \qquad \text{III.10}$$

where S is the area of intersection of the interaction volume region and the fiber (see Figure III.12(b)) and α_i is the given fraction of the fiber material incorporated within interaction volume. For this purpose, both geometrical features have been defined as polygonal regions within the Matlab code, and the problem has been solved with the aid of the mapping toolbox, which allows to perform set operations on polygonal regions (‘*polybool’* function). The equation Eq. III.10 has been solved with build-in numerical solver (‘*fzero’* function*)*. To find additional points of the desired locus, the region of interaction volume is translated by a small increment Δ_x along the x-axis with respect to the last found point. At this new location the required value of the y-translation Δ_y is found as a root of Eq. III.10. Since the problem has also symmetry properties along the axis inclined $\pi/4$ to the main axes, the process of finding the unknown contour is continued until the centre of the interaction volume lays on this symmetry axis. The remaining parts of the loci are constructed using the symmetry conditions.

Having all the necessary boundaries known, the calculation of the area and surface fraction of the appropriate regions $\mathcal{A}_i$ corresponding to the partition $\mathcal{H}$ is executed. The main results of the implemented strategy are presented in two complementary ways. The first one corresponds to the evolution of the assumed partition $\mathcal{H}$ with respect to the interaction volume size d (see Figures III.13(a-f) and III.15(a-c)). The second representation focuses on the distribution of discrete probability mass among the chosen intervals of effective modulus as well as its variation with increasing size of the interaction volume d (see Figures III.14(a-b) and III.16(a-b)).

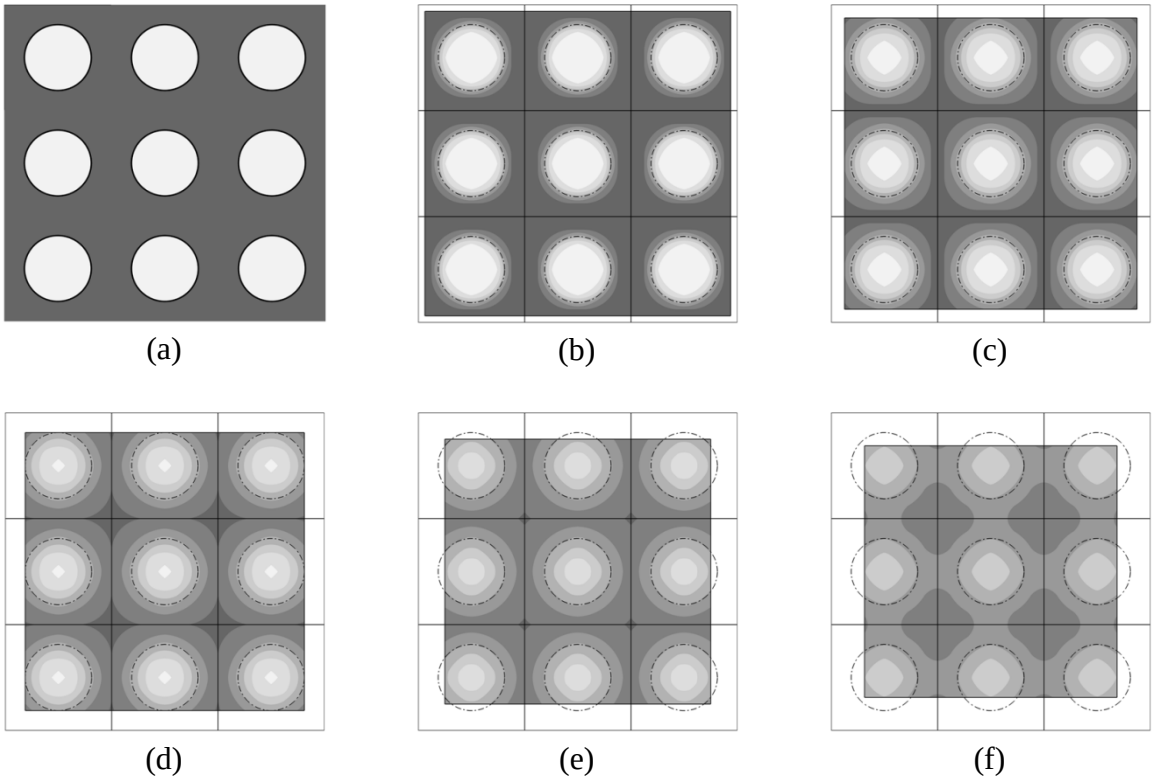

(a) (b) (c)

(d) (e) (f)

Figure III.13 Evolution of the partition (m=7) within the fiber matrix composite board obtained for D_f=25 [μm], D_{cell}=40 [μm] and the number of cells N_x×N_y=3×3, with respect to the size of the interaction volume d [μm]: a) d=0, b) d=5, c) d=10, d) d=15, e) d=20 and f) d=25.

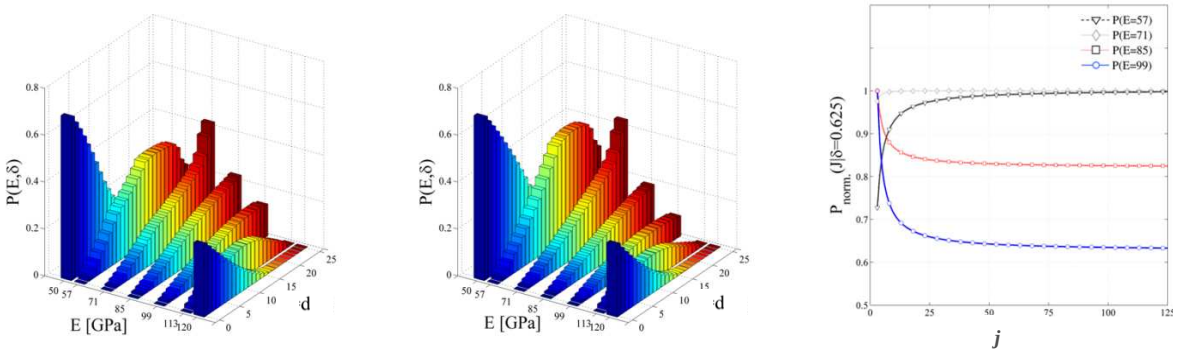

(a) (b) (c)

Figure III.14 Evolution of the discrete probability distribution of elastic modulus with respect to the interaction volume size d for fiber reinforced model (D_f=25 [μm], D_{cell}=40 [μm], m=7): a) N_x×N_y=3×3, b) N_x, $N_y \rightarrow \infty$. Influence of the number of the unit cells j within the investigated domain on the discrete probability values (c). The assumed mechanical properties are: E_1=120 [GPa] for fiber and E_2=50 [GPa] for matrix, equal volume fractions c_1=c_2=0.5.

Two cases of the fiber board configuration are considered. In both configurations the diameter of the fiber is kept constant D_f=25 [μm], but the size of the cell D_{cell} varies from 40 [μm] to 50 [μm]. As a consequence, the resultant volume fractions of fiber are c_f =0.19 and c_f =0.3. The effect of the increasing number of cells on the discrete distribution of the effective modulus is also investigated, and the results are shown on Figure III.14(c) and Figure III.16(b).

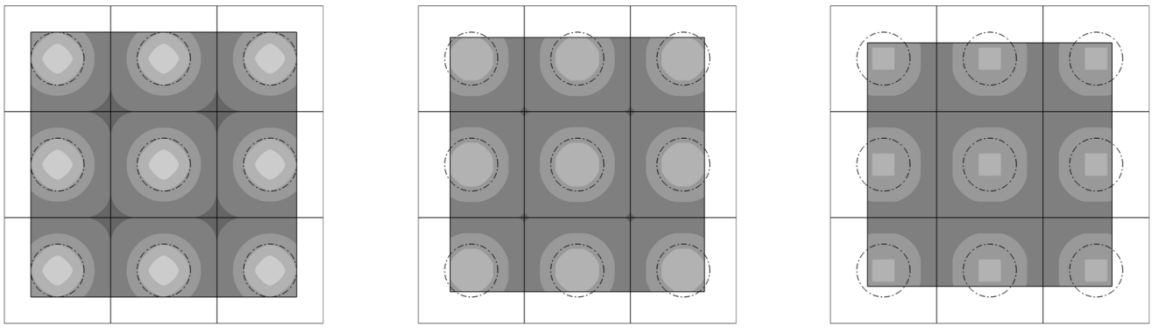

(a) (b) (c)

Figure III.15 Evolution of the partition (m=7) within the fiber matrix composite board obtained for D_f=25 [μm], D_{cell}=50 [μm], and the number of cells N_x×N_y=3×3 with respect to the size d of the interaction volume: a) d=25 [μm], b) d=30 [μm], c) d=35 [μm].

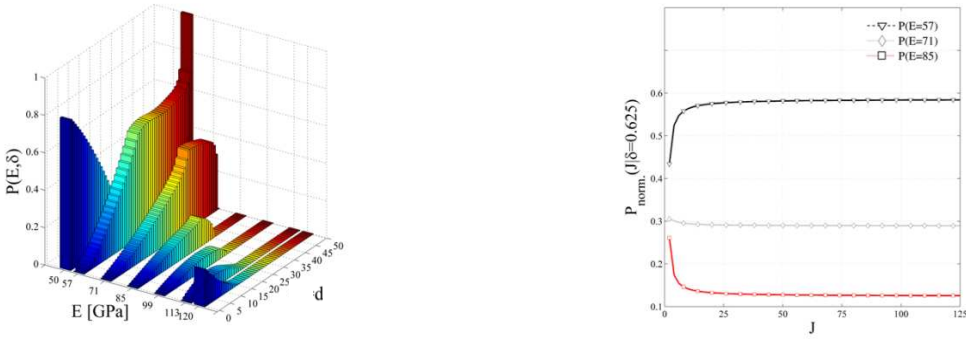

(a) (b)

Figure III.16 Evolution of: a) the discrete probability distribution of elastic modulus with respect to the size of the interaction volume d for fiber reinforced model (D_f=25 [μm], D_{cell}=50 [μ], m=7), b) selected probability masses with respect to the number of cells N_x, $N_y \rightarrow \infty$. The assumed mechanical properties are: E_1=120 [GPa] for fiber and E_2=50 [GPa] for matrix, equal volume fractions c_1=c_2=0.5.

III.5. DISCUSSION

III.5.1. Interaction Volume Size (Indentation Depth) vs. Measured Effective Response

The virtual experimental results gathered with the aid of the applied model give an insight in the relation between the size of the interaction volume *d* and the effective response of the material, defined by Eq. III.2. Hence, the results obtained for the two considered model microstructures follow the same universal principle, which the statistical grid indentation technique applied to the heterogeneous materials relies on; if the indentation depth *h* (related to *d* in the model) is much smaller than the characteristic size of the phases $h<<D$, then the single grid indentation test gives access to the material properties of either *Phase 1* or *Phase 2*.[6]

Therefore, a bimodal distribution of probability masses, and as a consequence the effective material response in the investigated biphasic composite microstructures, must be obtained when the interaction volume size *d* tends to zero. This principle is independent of the type of microstructure probed or the phase properties. The magnitude of the peaks in this limiting case corresponds to the volume fractions of each individual constituent. In opposition to this asymptotic state, the excitation of a larger volume of the bulk by the probe leads to the gradual decrease in the volume of the material, where the pure phase properties may be still attained for an increasing *d* value.

By continuously increasing the ratio d/D, the volume of the bulk with the access to the mixture response starts to prevail, diminishing to zero the chances of obtaining $E_{eff}= E_1$ or E_2. However, the homogenized modulus of elasticity is not attained yet at this point and requires the indentation activation volume to increase further and to approach the size of the Representative Elementary Volume (REV), called here d_{REV}. When *d* approaches d_{REV}, the probability mass accumulates within and around the discrete interval, where the homogenized modulus is included. Upon further increase of *d*, the unimodal distribution with the mode at the center on the mentioned interval dominates, changing ultimately into a single peak and constant probed values. The increase in homogenization material response is inherently related to the change of the dispersion of the results E_{eff} within the obtained experimental distribution. A good picture of this phenomenon is given by the variation of the range of experimental distribution of effective modulus with respect to the characteristic scale of the interaction volume *d* (see Figures III.17(a-b)). This measure of the statistical dispersion is not affected by the type of the distribution of the experimental data. Therefore, it appears to be a

suitable measure of phase homogenization (separation) along different scales as well as for identification of the material blocks with different mechanical properties.

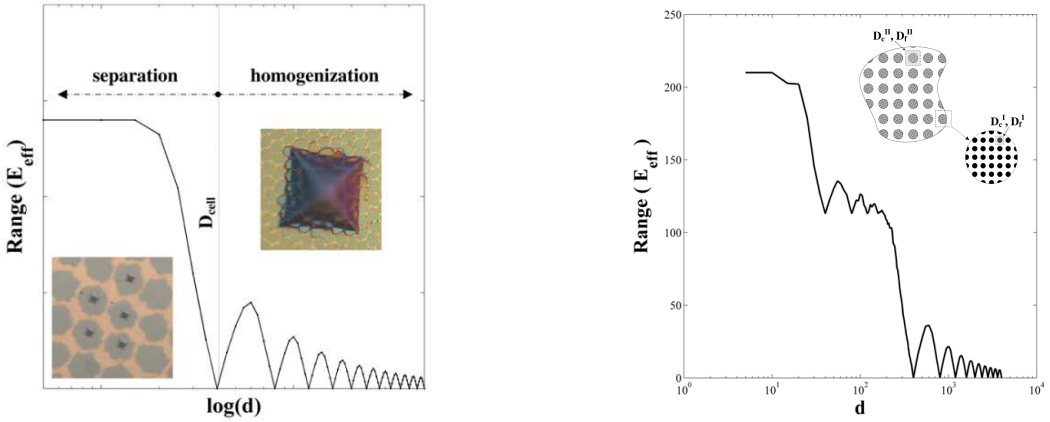

(a) (b)

Figure III.17 Homogenization (separation of scales) for statistical grid indentation on multi-phase materials. Variation of the range of E_{eff}: a) with characteristic scale of interaction volume on biphasic material, b) for multiphase material with double material levels (periodic microstructure, fiber reinforced composite model). Results obtained with a Monte-Carlo simulation in which, for every size d of the interaction volume, N=300 virtual measurements were made at random locations.

As was stated, the trends hold irrespectively of the model microstructure and the mechanical properties. However, the results indicate that the passage, from the bimodality ($d\rightarrow 0$) towards the unimodality ($d\rightarrow d_{REV}$) with transient discrete distributions, depends on the type of the microstructure considered (see Figure III.10(b), Figures III.14(a-b) and Figure III.16(a)). This issue requires further discussion.

Consider the checker board morphology, in which the volume of the material is distributed equally among the both constituents c_1=0.5 and the two adjacent checkers belong to different phases. Under these conditions, for any interaction volume of size d and model partition $\mathscr{H}$ of the mixture response area, the region of the material associated with the central interval $\mathscr{A}_{(m+1)/2}$ corresponds to the highest probability mass, excluding $\mathscr{A}_1$ and $\mathscr{A}_m$ intervals at this point. The result is the direct consequence of the geometrical constrains of this morphology, for which the volume representing this specific interval dominates over the remnants within the composite zone. This trend is independent on the actual size of the interaction cube $d=\langle 0;D\rangle$. However, by increasing d the probability mass accumulates more in

the central interval, leading to a monotonic rise of this peak (homogenization peak; $E_{eff}=0.5(E_1+E_2)$ above the other discrete values. This observation is independent from the number of discrete bins within the partition (see Figure III.10(a-c)). For the size of the interaction volume d equal to 32 times the size of the checker D, the chances of probing *Phase 1* or *Phase 2* are zero. Below this threshold, the experimental distribution spans over the entire domain of the effective moduli.

The characteristic feature of the checker board case was the continuous presence of the homogenized peak, which could be indentified for any transient distribution (for any value of $d=\langle 0;D\rangle$) due to its predominant character in composite class. Moreover, the distribution of the volume fractions of phases is symmetric $c_1=c_2=0.5$, and the characteristic length of the heterogeneity represented by the checker size D is equal for both phases.

Different results are obtained in the second investigated morphology representing uniaxial fiber-matrix composite. In this case, the way the homogenized response peak is complex and appears to depend not only on d but also on the division of volume fractions among the matrix and the fiber within the unit cell. Obviously, the volume fraction of each phase changes automatically with the change in the diameter of the fiber D_f, or equivalently with a change in the size of the cell $D_{cell.}$ Consequently, the chances of probing pure fiber response (*Phase 1*) or matrix (*Phase 2*) diminish to zero for different sizes of the interaction volume, which depends on the cell parameters. According to this, the fiber properties are no longer accessible if d approaches the limit value given as $d_F\approx 0.71D_f$, while for the matrix the threshold is $d_M\approx D_{cell}-0.71D_f$. The first threshold represents the maximum size of the cube inscribed within the circular fiber. The second threshold corresponds to the maximum size of the interaction volume within the domain of the matrix, located at the corner point of the basic cell (central point between four fibers). Additionally, the remaining discrete values must diminish to zero in a way governed by their distance from the interval where the homogenized modulus is located. When the interaction cube reaches the 'critical' size given as $d_{A_i}=\frac{D_f}{2}\sqrt{\frac{\pi}{\alpha}}$, where α stands for the volume fraction corresponding to the upper contour of the discrete subset, the associated mass goes to zero affecting the subsequent distributions to follow.

III.5.2. Sample Size Effect: Asymptotic Analysis

The probabilistic homogenization model formulated in this work assumes that the region occupied by the solid is finite, that the material is periodic and that the number of the unit cells j along the edge is defined. Therefore, the total volume of the sample of material is

$V=(jD)^3$. However, in order to keep the interaction volume within the domain of the material, the actual region of the bulk where the testing cube may be located must be reduced, providing an actual volume $V(d)=(jD-d)^3$, satisfying $V = \lim_{d\to 0} V(d)$. This type of boundary constraint provokes a size effect, in which the discrete probability masses depend on the population of the unit cells incorporated within the virtual volume exposed to testing (see Figures III.14(c) and III.16(b)). The impact of the size effect reduces with increasing number of the cells (heterogeneities) incorporated within the tested region. Consequently, the discrete probabilities converge towards asymptotic values, and the size dependency substantially diminishes. It appears that the results of the studied idealistic microstructures may be considered free of size effect, if the minimum number of the unit cells along the edge of the model is $j\approx 25$ for the checker board and $j\approx 50$ for the fiber microstructure. For a size of the virtual bulk above this limit the obtained results approximate the infinite body case.

III.5.3.An Approach to 1/10 Buckle's Rule-of-Thumb for Heterogeneous Materials

The solution of contact mechanics are derived from an infinite half-space model with spatially uniform mechanical properties. Therefore the estimations obtained in the indentation test represent the average quantities taken over the activated volume with the characteristic length d located beneath the indenter probe. A good estimate between the size d and the indentation depth h, at which the measurements were taken, is $d\approx 3h\text{-}4h$ for Berkovich indenter.[3,6] According to this rough estimation, one would expect phases to be identifiable on the experimental distribution at $h_{1/10}$=3.2 [μm] corresponding to the interaction volume size d=9.6-12.8 [μm] for the checker-board microstructure with the checker size D=32 [μm].

The results confirm this expectation (see Figures III.10(a-c) and III.18(a)). For the interaction volume size approaching the mentioned range, the probability of probing *Phase 1* and *Phase 2* is above the significance level of 10 % (P_1+P_2=22-33 %). In addition, the model discrete distribution incorporates two additional modes clearly defined at the locations E_1 and E_2, next to the homogenization peak. Further decrease in the ratio d/D amplifies both peaks, lowering significantly the chance to obtain a mixture material response, represented by the probability mass $P_{12}=1-P_1+P_2$. This implies a clear bimodal distribution.

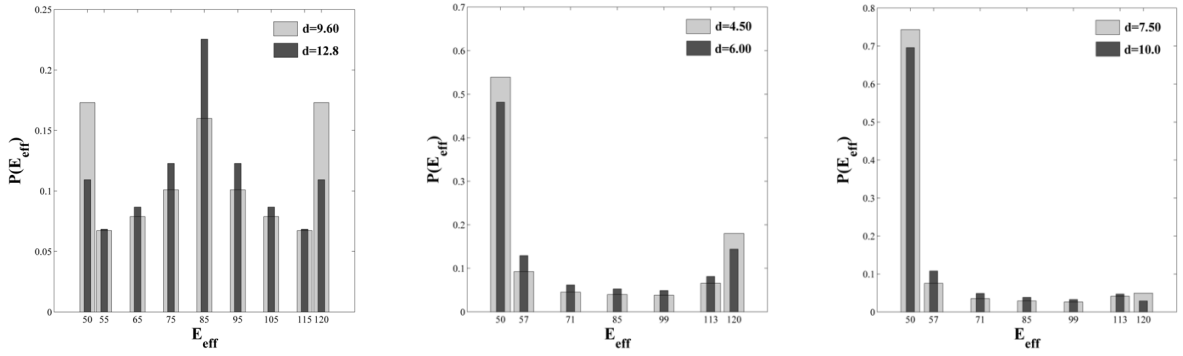

(a) (b) (c)

Figures III.18 Discrete probability distributions corresponding to the limiting values of the interaction volume size d associated with the 1/10 rule-of-thumb: a) checker-board microstructure $j\rightarrow\infty$, m=9, b) fiber composite model c_f = 0.3, c) fiber composite model $c_f \approx 0.10$.

In the second working example the choice of the satisfactory h relates to the two cell parameters, namely the diameter of the fiber D_f and the size of the cell D_{cell} or equivalently the fiber spacing distance L. Hence, the estimation of the 1/10 indentation depth is obtained on the basis of $min\{D_f, L\}$. Consider the case $\min\{D_f, L\}=L$ valid for all the cell configurations for which $c_f \geq 0.2$. According to this rule, the indentation depth h=1.5 [μm], which corresponds to the first of the investigated cell geometries with {D_f=25 [μm], L=15 [μm], giving c_f =0.3}, should be suitable to correctly depict the elastic properties of both constituents of the bulk. This depth entails an interaction volume d=4.5-6.0 [μm]. It may be observed that the size of the interaction volume from this range corresponds to the probability of probing a fiber P_f=0.14-0.18, giving exposed between 47 % up to 60 % of the maximum intensity $P_f^{max}(d\rightarrow 0)=c_f$ of this peak (Figure III.18(b)). The matrix phase may be identified much easier, since it is present in the significantly larger fraction c_m=0.7. Both phases are represented with clearly defined peaks in the bimodal distribution, whose separation and exposure increases with decreasing parameter d.

The separation of the fibers might increase, while keeping constant the diameter of the fiber $\min\{D_f, L\}=D_f$, and this case is represented by a model with D_f=25 [μm] and L=35 [μm] giving c_f=0.13 (Figure III.18(c)). In such a situation, the 1/10 rule implies the indentation depth h=2.5 [μm], what entails the interaction volume d=7.5-10 [μm] for the fiber phase to be identifiable. Because of the low volume fraction c_f, the related peak in the distribution spectra may be hindered and unidentified if the number of the discrete intervals is very small. However, the satisfactory separation and intensities of the peaks could be provided with a

more refined distribution. Alternatively, the indentation depth should be reduced to provide better separation and diminish the fraction of the records corresponding to the composite behavior.

III.6. CONCLUSIONS

This work represents an approach toward better understanding of the link between the characteristic scale of the measurement in the instrumented statistical indentation and the effective material properties obtained from the direct experiment on heterogeneous solids. It has been shown that the outcomes of the indentation experiment are scale and microstructure dependent. Providing that the characteristic scale of the interaction volume is sufficiently small when compared with the characteristic size of the incorporated phases, the inherent properties of the phases may be assessed. This trend holds up to the limiting value of the indentation depth, which is specified by the 1/10 principle.

The results obtained on simplified polycrystalline and fiber-matrix microstructures prove the use of Buckle's rule to approximate the upper threshold for any microstructure. Above this limit, the volume of the material, where the mixed response is assessed, starts to prevail. Therefore, the modes corresponding to the pure phase properties diminish significantly and may become indistinguishable. As a result, the experimental distribution may adopt different forms, depending how the microstructure is ordered. This evolution corresponds to the homogenization effect, which can be captured in the developed probabilistic frame.

III.7. REFERENCES

[1]C. Scheuerlein, T. Boutboul, D. Leroy, L. Oberli, B. Rehmer, "Hardness and tensile strength of multifilamentary metal-matrix composite superconductors for the Large Hadron Collider," European Organization for Nuclear Research, LHC project report 950 (2006).

[2]W. C. Oliver, G. M. Pharr "Measurements of hardness and elastic modulus by Instrumented Indentation: Advances in understanding and refinements of methodology," J. Mater. Res., 19 3-20 (2004).

[3]G. Constantinides, F. -J. Ulm, K. Van Vliet, "On use of nanoindentation for cementitious materials," Mater. Struct., 36 191-196 (2003).

[4]F. W. Zok "Developments in oxide fiber composites," J. Am. Ceram. Soc., 89 3309-3324 (2006).

[5]H. Bückle, VDI-Berichte, 41 (1961).

[6]G. Constantinides, K. S. Ravi Chandran, F. -J. Ulm, K. J. Van Vliet, "Grid indentation analysis of composite microstructure and mechanics: Principles and validation," Mat.Sci.Eng. A.,430 189-202 (2006).

[7]F. -J. Ulm, M. Vandamme, C. Bobko, J. A. Ortega, K. Tai, C. Ortiz, "Statistical Indentation Techniques for Hydrated Nanocomposites: Concrete, Bone and Shale," J. Am. Ceram. Soc., 90 2677-2692 (2007).

[8]H. Gao, C. H. Chi, J. Lee, "Elastic contact versus indentation modeling of mulit-layered materials," Int. J. Solids Struct., 29 2471-2492 (1993).

[9]J. Li, T. W. Chou, "Elastic field of a thin-film/substrate system under an axisymmetric loading," Int. J. Solids Struct., 34 4463-4478 (1997).

[10]M. F. Ashby, D. R. H. Jones, Engineering Materials 2, An introduction to microstructures, processing and design, 2nd edition, Butterworth-Heinemann (1998).

[11]J. Qu, M. Cherkaoui, Fundamentals of micromechanics of solids, John Wiley & Sons, Inc. (2006).

[12]P. Trtik, B. Münch, P. Lura, "A critical examination of nanoindentation on model materials and hardened cement pastes based on virtual experiments," Cem. Con. Comp., 31 705-714 (2010).

[13]A. Papoulis, Probability, random variables, and stochastic processes, McGraw-Hill, Inc., 3rd Edition (1991).

[14]A. C. Fischer-Cripps, Introduction to contact mechanics, Mechanical Engineering Series, Springer, 2nd Edition (2007).

IV. Assessment of Nanomechanical Phase Properties of Heterogeneous Materials by Means of the Maximum Likelihood Approach and Nanoindentation

ABSTRACT

The statistical grid indentation technique on heterogeneous materials is extended by the implementation of the bivariate Gaussian Mixture Model and Maximum Likelihood concept as a primary tool in the deconvolution analysis. Current deconvolution strategies reported in the literature are shortly reviewed. Next, the theoretical background for the Maximum Likelihood based deconvolution in bivariate space is briefly outlined. Following this introduction, the applicability of the proposed deconvolution approach is addressed on the basis of experimental results representing broad spectrum of materials, from naval brass to ordinary cement paste and masonry clay brick. The mechanical properties of α-, β-phase of naval brass, hydration products of ordinary cement paste, as well as polycrystalline-amorphous 'glassy' matrix phase and other additional phases incorporated in clay brick, are estimated. Clustering of the grid observations within each of these materials is executed based on a posteriori probability criterion, in which probabilistic maps of the indented region are constructed and linked with compositional (atomic number contrast) backscattered electron micrograph of indented surface, as well as the compositional maps prepared with the energy-dispersive x-ray spectrometer. As a last step, the inference of the number of phases with the highest probability to occur and compatible with the grid indentation data set is outlined. Finally, the results obtained in the frame of the proposed bivariate mixture modeling based on the maximum likelihood estimation are compared with the estimations from other deconvolution strategies reported in the literature.

IV.1. INTRODUCTION

Current conventional methods of material characterization, e.g. uniaxial compression and tension test or indirect tension test (Brazilian test), allow measuring the elastic properties and strength of the materials at their macro scale. Although it is convenient to use this methodology in the final stage of the macro characterization of a composite material, frequently it is desired to know the mechanical characteristics of the composite components in order to predict its macro behavior, to avoid redundant testing, to better understand the material and to develop new tailored or eco-efficient materials. Many composites, such as cement-based materials or ceramics, follow a multi-scale micromechanical scheme, where the microstructure and material phases depend on the length-scale of observation. In such situations it is of interest to find the mechanical properties of the fundamental building blocks of the material as well as the material domains at the intermediate observation scales.

Experimentalists are forced to access material phases much below the ordinary macro-scale, reaching the nanometers scale and use refined experimental techniques, being one of those the instrumented indentation combined with grid indentation analysis. The origin of this method comes from the traditional hardness test developed by Brinell, in order to evaluate the quality of produced steel.[1] He forced a hard probe to produce a visible imprint on the surface of the tested material. The ratio of the force applied P and the projected area of contact A_c defines the material hardness $H=P/A_c$. It was shown by Tabor[2] that the hardness or average pressure under the indenter is correlated to the uniaxial yield stress σ by a factor C, as $H=C\sigma$. This fundamental idea remains in the instrumented indentation, although recent developments in material science have called for significant modifications of the method in order to satisfy the growing experimental demands. The combination of the high resolution recording devices (sensors and actuators) allow continuous monitoring of the loads and displacements on the indenter as it is driven and withdrawn from a material. Typically, two material properties are derived from the indentation curve (P-h curve), namely the indentation hardness H and the indentation modulus M,[3,4] and the latter is related with the elastic modulus of the indented solid.

The simplicity of this experimental approach combined with the high accuracy of the results, as well as good repeatability, made the technique widely used in the last decades for the characterization of different materials. Examples include human soft and mineralized tissue,[5,6] coatings to polymers.[7,8] Most of these studies address instrumented indentation on single phase materials. In addition, if the investigated material is of composite nature, the

phases are of sufficient size and exhibit well defined boundaries.[9,10] This allows placing the indenter probe on a specific target and running statistically relevant number of measurements in a common fashion. Obviously, this is not the case for a large group of known multi-scale composite materials like concrete, shale or fired clay brick and many others. Such materials are a class of complex chemo-mechanical materials with a high degree of heterogeneity from atomistic scales to the macroscopic scales.[11,12] Thus, in order to obtain the relevant mechanical characteristics of the material domains from the lowest accessible scales, one must ensure the conditions under which the probed volume of material is representative, the so-called Representative Elementary Volume (REV).[13] In addition, existing phases have unclear boundaries and are randomly distributed within the volume. These facts have driven towards the extension of instrumented indentation analysis to structurally heterogeneous materials and the implementation of the statistical grid indentation technique.[14,15,16]

The grid indentation technique consists on the continuous probing of the material in the nodal points of a designed grid, spanned over the representative region of material. The large set of acquired data is analyzed by statistical means, what makes the identification of mechanically relevant phases possible, as well as allows to define the phase's packing density and morphology. In addition, the relation between the volume fractions of incorporated phases may be estimated. Since the final result of the grid indentation depends on the data analysis tools, the choice of the proper statistical approach for data processing is of crucial importance.

This manuscript addresses the problem of the grid indentation data analysis for heterogeneous materials. The first part of this chapter presents a detailed state of the art of the grid indentation and its fundamental assumptions. It also includes review of the current techniques applied in order to analyze the experimental outcomes in the qualitative and quantitative way. The subsequent part of the chapter deals with the application of the Maximum-Likelihood Approach for the sake of phase properties estimation with regard to the Gaussian Mixture Model. Afterwards, the estimation of the number of phases according to Bayesian Information statistics is considered. Following this approach, the internal data clustering is presented based on a posteriori probability criterion. The classification of abnormal observations is also discussed. Finally, the proposed method is compared with current deconvolution strategies reported in the literature.

IV.2. INSTRUMENTED GRID INDENTATION ON HETEROGENUOUS SOLIDS

The instrumented grid indentation technique proposed by Constantinides et al.[14,17] emerged from experimental investigations in cement based materials, with the objective to extract the mechanical and morphological characteristics of calcium-silicate-hydrate (*C-S-H*) nanocomposites.[11,18,19] In order to do this, an experimental protocol to measure the intrinsic properties on each scale has been proposed. One of the basic assumptions of this strategy is the existence of a *REV*, for which the constitutive relation between the stress and strain is independent of the length scale of analysis represented by indentation depth.[11] This independency is assured by the micromechanics scale separability condition, which must hold for the representative volume (Eq. IV.1):

$$d \ll L \ll (h, a, D) \qquad \text{IV.1}$$

where *(h,a)* are the indentation depth and radius, *D* is a characteristic microstructural length scale and *d* is the characteristic size of the (largest) heterogeneity included within *REV* (see Figure IV.1). Provided that this relation holds, an indentation experiment executed to an indentation depth *h* gives access to the material properties associated with the characteristic length scale *L*. In general, for indentation depths $h << D$ the experimentalist assesses the intrinsic phase properties, while for $h >> D$ the composite properties are probed.

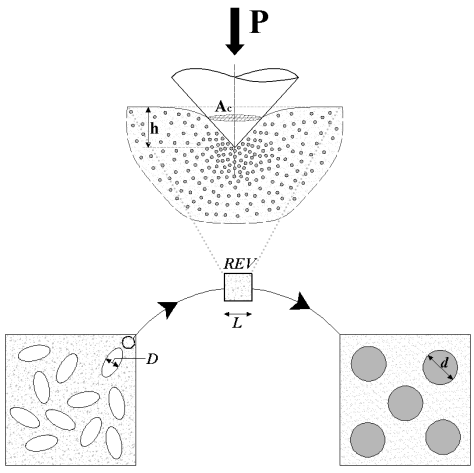

Figure IV.1 General representation of the indentation within multi-phase heterogeneous material: *P* - indentation force, *h* - indentation depth, A_c - projected area of contact, *d* and *D* - characteristic lengths of the incorporated heterogeneities, *L* - characteristic length scale of the *REV* representative volume.

Since the indentations are executed on a grid spanned over a defined region of a material, the internal spacing of the indents within the grid must assure the independency of successive measurements. In other words, the grid spacing l_x, l_y (see Figure IV.2(a)) should be larger than the characteristic size of the residual impression.[14] In the result, the probability of probing the specific phase equals its surface fraction. Additionally, if the grid spans over a region of material that is large enough to be considered as a representative, the surface fractions approach the volume fraction for the random heterogeneous materials.[20]

At each *i-th* point of the grid the *P-h* curve is recorded, which is used for calculation of the indentation modulus M_i and hardness H_i, where $i=1\ldots N$ with N as total number of executed indentations in the single grid experiment. This pair of values is the experimental realization $\boldsymbol{x}_i=[H_i, M_i]$ of the random variable $\boldsymbol{X}$. A possible outcome of a single indentation trial is $\boldsymbol{x}_i$ belonging to one of the g phases present within investigated region (see Figure IV.2(a)). Hence, the set of all possible outcomes of $\boldsymbol{X}$ defines the experiment sample space S in Eq. IV.2:[21,22]

$$S=\left\{\mathbf{x}=[M,H]\middle|\mathbf{x}\in\left\{G_1,\ldots,G_g\right\}\right\} \qquad \text{IV.2}$$

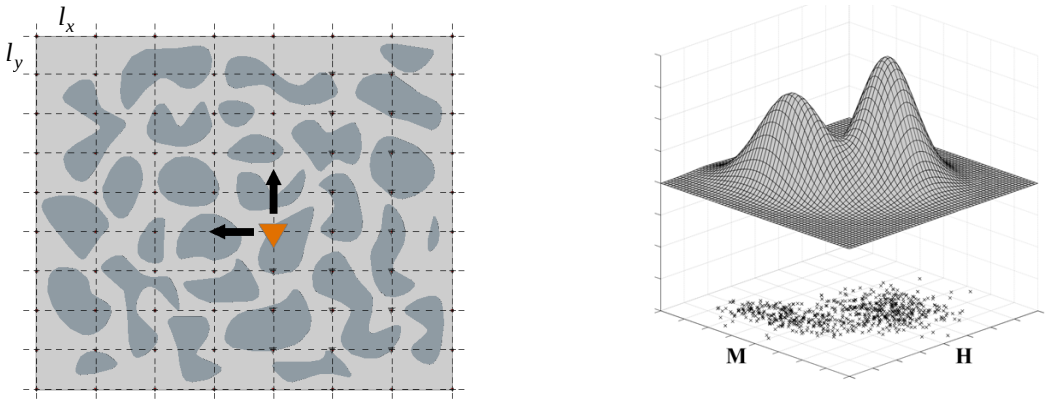

(a) (b)

Figure IV.2 Scheme of the grid indentation approach for multi-phase materials proposed by Constantinides (a),[11] the low indentation depths $h << D$ give an access to mechanical properties of individual phases, for each grid point the vector of properties is obtained in the form $\boldsymbol{x}_i=[H_i, M_i]$. The final result is a multimodal bivariate distribution (b).

Phases are considered to be material domains specified by distinct pairs of indentation modulus and hardness values on average $\boldsymbol{\mu}_j=[H_j, M_j]$, $j=1\ldots g$. The material heterogeneity together with imperfections of the probed surface and instruments leads to inherent scatter of the results in the domain of single phase G_j. Therefore, $\boldsymbol{x}$ within a phase G_j is distributed

around its expected value and may be modeled with a corresponding distribution function $f_j=f_j(\mathbf{x};\boldsymbol{\varphi}_j)$, where $\boldsymbol{\varphi}_j$ is a vector of unknown distribution parameters. The probability density function (p.d.f) of an observation vector $\boldsymbol{x}$ in S can therefore be represented in the finite mixture form by Eq. IV.3 (Figure IV.2(b)):[23]

$$f(\mathbf{x};\boldsymbol{\psi}) = \sum_{j=1}^{g} \pi_j f_j(\mathbf{x};\boldsymbol{\varphi}_j), \quad \sum_{j=1}^{g} \pi_j = 1, \quad \pi_j \geq 0 \qquad \text{IV.3}$$

where the $\pi_j,\ldots,\pi_g$ are weighting factors of each phase and $\boldsymbol{\psi}$ denotes the vector of all unknown parameters $\boldsymbol{\psi}=[\pi_j,\ldots,\pi_g,\boldsymbol{\varphi}_j,\ldots,\boldsymbol{\varphi}_g]$ associated with $f_1,\ldots,f_g$. The adopted distribution function f_j considered here is a multivariate normal distribution, hence $\boldsymbol{\varphi}$ consists of the elements of the mean vectors $\boldsymbol{\mu}_j$ and the distinct elements of the covariance matrices $\boldsymbol{\Sigma}_j$. To the end of this discussion the outcome of the grid indentation is considered to follow a Gaussian Mixture Model (GMM), and the determination of an estimate $\hat{\boldsymbol{\psi}}$ of its vector of parameters $\boldsymbol{\psi}$ is one of the main objectives of this work.

IV.3. REVIEW OF STANDARD ESTIMATION METHODS

IV.3.1. Probability Distribution Function (PDF)

One of the first attempts to estimate the vector of unknown parameters $\boldsymbol{\psi}$ was the standard error minimization procedure based on empirical frequency distributions (histograms).[11,14,19] In this approach, each component of the vector $\boldsymbol{x}$ is assumed to represent the independent, uncorrelated random variable $x=H,M$. Following this assumption the model univariate mixture for each variable may be represented as:

$$f_x(x;\boldsymbol{\psi}_x) = \sum_{j=1}^{g} \pi_j f_j^x(x;\boldsymbol{\varphi}_j^x), \quad \sum_{j=1}^{g} \pi_j = 1, \quad \pi_j \geq 0 \qquad \text{IV.4}$$

where

$$f_j^x(x,\boldsymbol{\varphi}_j^x) = \frac{1}{s_j^x\sqrt{2\pi}} \exp\left(\frac{-(x-\mu_j^x)^2}{(s_j^x)^2}\right) \qquad \text{IV.5}$$

is the distribution function for indentation modulus or hardness within single phase. Therefore μ_j^x and $(s_j^x)^2$ stand for the mean value and the variance of x variable within phase j, and are the components of vector of unknown parameters $\boldsymbol{\varphi}_j^x$. Next, the histograms, which represent the discrete values $F_i^x=H,M$ of indentation moduli and hardness, are constructed from the set of

the experimental records. The number of the histogram's intervals m and their size may be approximated according to the rule proposed by Scott (Eq. IV.6),[24,25] originally developed for normally distributed random variables:

$$h_0 \approx 3.486\sigma / \sqrt[3]{N} \qquad \text{IV.6}$$

where h_0 is a size of the bin, σ is an estimate of the standard deviation and N stands for number of data points. To find an estimate $\hat{\psi}$ of $\boldsymbol{\psi}=[\pi_j,\ldots,\pi_g,\boldsymbol{\varphi}_j^H,\boldsymbol{\varphi}_j^M,\ldots,\boldsymbol{\varphi}_g^H,\boldsymbol{\varphi}_g^M]$, where $\pi_j,\ldots,\pi_g$ are weighting factors of each phase and $\boldsymbol{\varphi}$ consists of μ_j^x and s_j^x, one must solve the problem of minimization of the sum of residual errors in the form given by:

$$\min \sum_{x=M,H} \sum_{i=1}^{m} (F_i^x - f_x(x_i;\boldsymbol{\psi}_x))^2, \quad \sum_{j=1}^{g} \pi_j = 1, \quad \pi_j \geq 0 \qquad \text{IV.7}$$

over all discrete points $i=1\ldots m$ of` experimental distributions $F_i^x=H,M$. An application of this approach is presented below, on the experimental data obtained from the grid indentation on naval brass (CDA 464) reported by Randall et al..[26] Naval brass contains two primary phases, α and β, whose mechanical properties are known to be indistinguishable by standard microindentation techniques. Therefore, the grid indentation was applied in order to extract mechanical characteristics of mentioned phases at sub-micron scale. The deconvolution of the experimental records with the p.d.f technique estimates the vectors of properties to be H_α=2.27 [GPa], M_α=134.41 [GPa] and H_β=2.83 [GPa], M_β=122.85 [GPa] (see Figures IV.3(a-b)). The corresponding weight of each phase is π_α=0.59 and π_β=0.41, respectively.

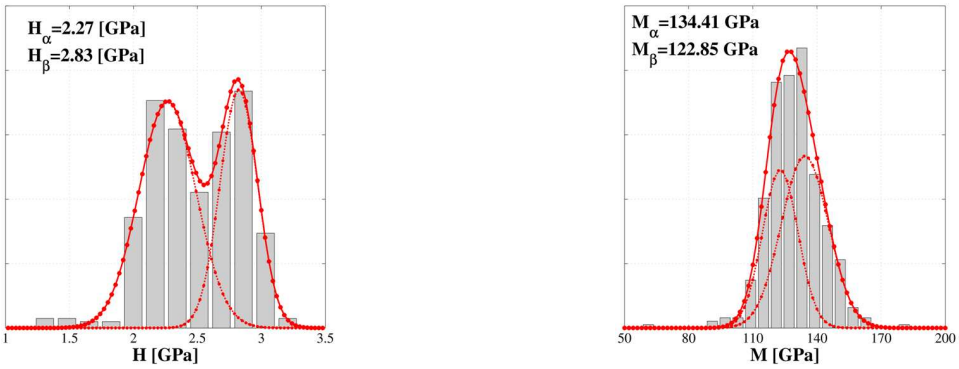

(a) (b)

Figure IV.3 Histogram based estimation of distribution parameters, experimental massive grid analysis on polished brass (naval brass CDA 464),[26] grid $N\times M$=20×20, maximum load 2 [mN], $l_x=l_y$=5 [μm]: a) histogram distribution of H and its fit, b) histogram distribution of M and its fit.

IV.3.2. Cumulative Distribution Function (CDF)

The deconvolution technique introduced in the previous section is based on the construction of the empirical frequency distribution. It has been widely recognized that the change in the size of the bin, or the shift in the initial point of the histogram, affects the probability discrete values.[22,25] As a consequence, the estimation of the model parameters is also affected, and an alternative approach has been proposed:[15,27] instead of probability density functions, the cumulative distribution functions c.d.f has been used. The entire c.d.f based deconcolution technique begins with the generation of the experimental cumulative distribution functions Eq. IV.8 for variables *M* and *H*, which are considered independent and uncorrelated. Let *N* be the total number of indentation tests in a single grid experiment and $\{H_i\}$ and $\{M_i\}$ for $i=1\ldots N$ the sorted values of the measured quantities. The *N* points of the empirical c.d.f for modulus and hardness, denoted by D_x where $x=H,M$, are obtained from the following definition:

$$D_i^x(x_i) = \frac{i}{N} - \frac{1}{2N}\ ,\ i = 1\ldots N \qquad \text{IV.8}$$

Once the empirical cumulative distributions are constructed the model c.d.fs are specified holding the assumption of Gaussian type distribution, for which the adopted c.d.fs are in the form of:

$$d_j^x(x_i, \boldsymbol{\varphi}_j^x) = \frac{1}{s_j^x\sqrt{2\pi}} \int_{-\infty}^{x_i} \exp\left(\frac{-(u-\mu_j^x)^2}{(s_j^x)^2}\right) du \qquad \text{IV.9}$$

and the model c.d.f is given by:

$$D_x(x_i; \boldsymbol{\psi}_x) = \sum_{j=1}^{g} \pi_j d_j^x(x_i; \boldsymbol{\varphi}_j^x),\ \ \sum_{j=1}^{g} \pi_j = 1,\ \ \pi_j \geq 0 \qquad \text{IV.10}$$

The estimate $\hat{\boldsymbol{\psi}}$ of unknown model parameters vector $\boldsymbol{\psi}=[\pi_j,\ldots,\pi_g,\boldsymbol{\varphi}_j^H,\boldsymbol{\varphi}_j^M,\ldots,\boldsymbol{\varphi}_g^H,\boldsymbol{\varphi}_g^M]$ is determined by the minimization of a least square problem, in which the residual is the difference between empirical cumulative and model cumulative distributions:

$$\min \sum_{x=M,H} \sum_{i=1}^{m} (D_i^x - D_x(x_i; \boldsymbol{\psi}_x))^2,\ \ \sum_{j=1}^{g} \pi_j = 1,\ \ \pi_j \geq 0 \qquad \text{IV.11}$$

The postulated minimization problem is strengthened with the additional condition given by Eq. IV.12 and regarding the 'statistical phase contrast' to avoid significant overlap of two neighboring Gaussian distributions. This condition also implies the coupling of mean properties to represent a single phase, $M_j < M_{j+1}$ and $H_j < H_{j+1}$ respectively.

$$\mu_j^x + s_j^x \leq \mu_{j+1}^x - s_{j+1}^x \qquad \text{IV.12}$$

As usual, the condition of global minimum must be satisfied in order to consider the vector $\hat{\boldsymbol{\psi}}$ as a correct solution of estimation problem. The case of grid indentation carried out on the Ordinary Portland Cement paste (OPC) is presented next (see Figures IV.4(a-b)). The experimental c.d.fs are fitted with a four component c.d.f mixture, which represents the primary hydration products low-density and high-density calcium-silica-gels phases, (*LD-C-S-H*, *HD C-S-H*) H_{LD}=0.51 [GPa], M_{LD}=16.44 [GPa], and H_{HD}=0.95 [GPa], M_{HD}=27.76 [GPa], as well as ultra-high-density *C-S-H* (*UHD C-S-H*) and non-reacted clinker phases, H_{UHD}=1.71 [GPa], M_{UHD}=42.30 [GPa], and H_{CL}=4.75 [GPa], M_{CL}=86.47 [GPa].

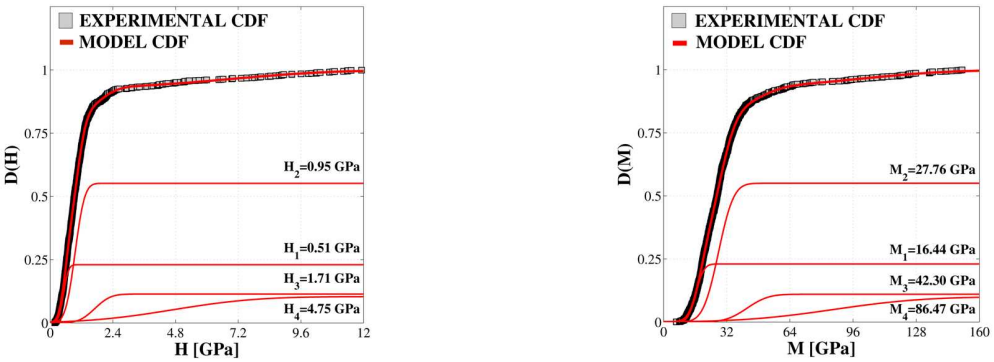

(a) (b)

Figure IV.4 Deconvolution of cement paste grid indentation data, experimental massive grid analysis on polished cement paste (w/c=0.4): a) c.d.f deconvolution of H, b) c.d.f deconvolution of M.

IV.4. MAXIMUM LIKELIHOOD APPROACH (MLA)

IV.4.1. Estimation of Parameters via Incomplete Data Concept

The strategies reviewed in the previous paragraph rely on the assumption of the univariate mixture to model the distribution of each of the measured quantities Eq. IV.4 and Eq. IV.10. As it has been shown on the experimental data of naval brass and OPC, such an approach may lead to the estimation of the phase mechanical properties, which exhibits good agreement with the literature data obtained with other, independent experimental methods. However, this assumption does implicate two independent statistical experiments, one for each measured property, with the outcomes being uncorrelated. According to the definition given in Eq. IV.2, the sample space of the random variables obtained with the grid indentation experiment are

the vectors in the form $\boldsymbol{x}_i=[H_i, M_i]$. This means that the hardness of the phase and the indentation modulus are the outcomes of the single experiment. As a consequence, the probability and its density are the bivariate functions defined in the $\Re^2$ space $H\times M$. To account for this, the bivariate Gaussians Mixture Model[23,28,29] is proposed next to model the grid indentation outcomes. Consequently, the assessment of nanomechanical phase properties by means of the Maximum Likelihood (ML) supported with Expectation-Maximization (EM)[30] algorithm applied to nanoindentation is introduced as a primary estimation tool. Additionally, the inference of a number of statistically relevant components within ML frame, as well as grid indentation data clustering, is introduced.

The first use of ML based estimation for a mixture model has been attributed to Rhao,[23,31] who used it for the case of two univariate distributions with equal variances. Further developments were carried along the years and led to the implementation of the ML and EM algorithm for different cases of mixtures in a large diversity of fields like biology, medicine or social sciences.[23,32] This technique proved its usefulness not only in the estimation of mixture parameters, but also in the cluster analysis of data due to its inherent ability to identify the internal structure of a data set for which no prior information is provided regarding the components properties and their structures. In particular, efficient iterative solutions of the ML equation via the EM algorithm are well established and widely adopted to study finite mixtures of Gaussians components. This methodology is readily applicable to the analysis of massive grid indentations results, where the experimental data exhibit the structured form due to indentation within a heterogeneous material.

The modeling of grid indentation data with the assumption of mixture of normal components begins by considering each indentation event $\boldsymbol{x}_i=[H_i, M_i]$ to be the realization of the random vector variable $\boldsymbol{X}$, which defines an appropriate sample space, see Eq. IV.2. In practice, $\boldsymbol{X}$ contains the random variables corresponding to $p=2$ measurements taken at the *i-th* node of the experimental grid. Hence, $\boldsymbol{X}=(\boldsymbol{X}_1^T,\ldots,\boldsymbol{X}_n^T)^T$ is a an n-tuple of points in $\Re^2$ with related realization vector $\boldsymbol{x}=(\boldsymbol{x}_1^T,\ldots,\boldsymbol{x}_n^T)^T$. The corresponding distribution function $f(\boldsymbol{x};\boldsymbol{\psi})$ of a g component finite mixture is given in the form defined by Eq. IV.3, whereas the components densities take now the form of the following bivariate Gaussian distribution:

$$f_i(\mathbf{x}_j;\boldsymbol{\varphi}_i)=\frac{1}{\sqrt{2\pi}}\left(|\boldsymbol{\Sigma}|\right)^{-\frac{1}{2}}\exp\left\{-\tfrac{1}{2}(\mathbf{x}-\boldsymbol{\mu})^T\boldsymbol{\Sigma}^{-1}(\mathbf{x}-\boldsymbol{\mu})\right\} \qquad \text{IV.13}$$

The indentations x_i are assumed to be independent and identically distributed $X_1,\ldots,X_n \overset{i.i.d}{\sim} F$ realizations of random variable.[23,28,29] The likelihood function for the vector of unknown parameters ψ, formed from the grid indentation data x, is denoted by $L(\psi)$ and given in log form as:

$$\log L(\boldsymbol{\psi}) = \sum_{j=1}^{n} \log f(\mathbf{x}_j;\boldsymbol{\psi}) \qquad \text{IV.14}$$

The Maximum Likelihood based estimation of vector ψ requires solving the likelihood equation given by:

$$\partial \log L(\boldsymbol{\psi}) / \partial \boldsymbol{\psi} = 0 \qquad \text{IV.15}$$

The application of the EM algorithm to the problem above requires the introduction of an additional set of variables Z, whose realization z is given by Eq. IV.16. This serves as a vector of labels of observations by defining the component in the mixture model from which the random vector x is withdrawn, as a type of binary indicator.

$$\mathbf{z}_{ij} = \begin{cases} 0 & \mathbf{x}_j \neq i \\ 1 & \mathbf{x}_j = i \end{cases} \qquad \text{IV.16}$$

This conceptualization allows to formulate the estimation problem as an incomplete-data problem (unknown data labels, variable z), for which the complete-data log-likelihood function for ψ is constructed as:

$$\log L_c(\boldsymbol{\psi}) = \sum_{i=1}^{g}\sum_{j=1}^{n} z_{ij}\left\{\log \pi_i + \log f_i(\mathbf{x}_j;\boldsymbol{\varphi}_i)\right\} \qquad \text{IV.17}$$

The components of the label vector z are treated as missing data. The estimation of distribution parameters with EM algorithm proceeds iteratively in two steps: expectation (E) and maximization (M).[23,30,33] The E-step handles the addition of Z by taking the conditional expectation of the complete-data log-likelihood $log(L_c(\psi))$ given the observed data x and using the current fit $\psi_{(k)}$ for ψ, as:

$$E_{\boldsymbol{\psi}^{(k)}}(Z_{ij}\,|\,\mathbf{x}) = pr_{\boldsymbol{\psi}^{(k)}}\left\{Z_{ij}=1\,|\,\mathbf{x}\right\} = \tau_i(\mathbf{x}_j;\boldsymbol{\psi}^{(k)}) \qquad \text{IV.18}$$

The current posterior probability $\tau_i(x_j;\psi^{(k)})$ that the *j-th* member of the indentation sample belongs to one of the components of the mixture is given by the Bayes Theorem:

$$\tau_i(\mathbf{x}_j;\boldsymbol{\psi}^{(k)}) = \pi_i^{(k)} f_i(\mathbf{x}_j;\varphi_i^{(k)}) / \sum_{h=1}^{g} \pi_h^{(k)} f_h(\mathbf{x}_j;\varphi_h^{(k)}) \qquad \text{IV.19}$$

for $i=1,\ldots,g$ and $j=1,\ldots,N$. The *M*-step aims at the global maximization of the complete likelihood function with respect to vector $\boldsymbol{\psi}$ over the parameter space Ω, given the expectation $E_{\boldsymbol{\psi}}^{(k)}(Z_{ij}|\mathbf{x})$ calculated in the *E*-step. The current fitting for the mix proportions, and the component means and covariance matrices are calculated explicitly as:

$$\pi_i^{(k+1)} = \sum_{j=1}^{n} \tau_i(\mathbf{x}_j;\boldsymbol{\psi}^{(k)}) / n \qquad \text{IV.20(a)}$$

$$\mu_i^{(k+1)} = \sum_{j=1}^{n} \tau_{ij}^{(k)} x_j / n\pi_i^{(k+1)} \qquad \text{IV.20(b)}$$

$$\Sigma_i^{(k+1)} = \sum_{j=1}^{n} \tau_{ij}^{(k)} (x_j - \mu_i^{(k+1)})(x_j - \mu_i^{(k+1)})^T / n\pi_i^{(k+1)} \qquad \text{IV.20(c)}$$

The *E*- and *M*-steps are alternated repeatedly until the difference in the likelihoods changes by an arbitrary small amount in the case of convergence of the sequence of likelihood values. As was shown by Dempster,[30] the ML estimate is non-decreasing on each iteration of EM algorithm and converges in the sequence of likelihood values to a fixed point in the parameter space. An additional feature of this approach is the probabilistic clustering of indentation data into g groups, obtained in terms of the fitted posterior probabilities of component memberships. Allocation of the indentation records $\boldsymbol{x}$ to the specific model's group is achieved by assigning each data point to the mixture component to which it is the highest estimated posterior probability of belonging, expressed by the Bayes rule of allocation $r_B(\boldsymbol{x}_j)$:

$$r_B(\mathbf{x}_j) = i \;\; if \;\; \tau_i(\mathbf{x}_j) \geq \tau_h(\mathbf{x}_j) \qquad \text{IV.21}$$

where $r_B(\boldsymbol{x}_j)=i$ implies that the *j-th* record within the indentation grid is assigned to the *i-th* statistically and mechanically relevant component existing within the investigated region of the material, $i=h=1,\ldots,g$ and $j=1,\ldots,N$. The reader is referred to references[23,28,29,33] for detailed discussions of ML method and EM algorithm.

The applicability of this approach to the grid indentation data analysis is demonstrated next on the grid indentation data from ordinary Portland cement paste and masonry clay brick investigated by the author. The estimation of distribution parameters is carried out with a non-commercial program for statistical mixture analysis EMMIX, developed by McLachlan et al..[34,35]

IV.4.2. Application to Cement Paste

The first application considers the OPC data previously deconvoluted with the c.d.f. based estimation method in Section IV.3.2. The experimental grid indentation data are now presented in the form of a scatter diagram on the *H*×*M* plane (Figure IV.5(a)).

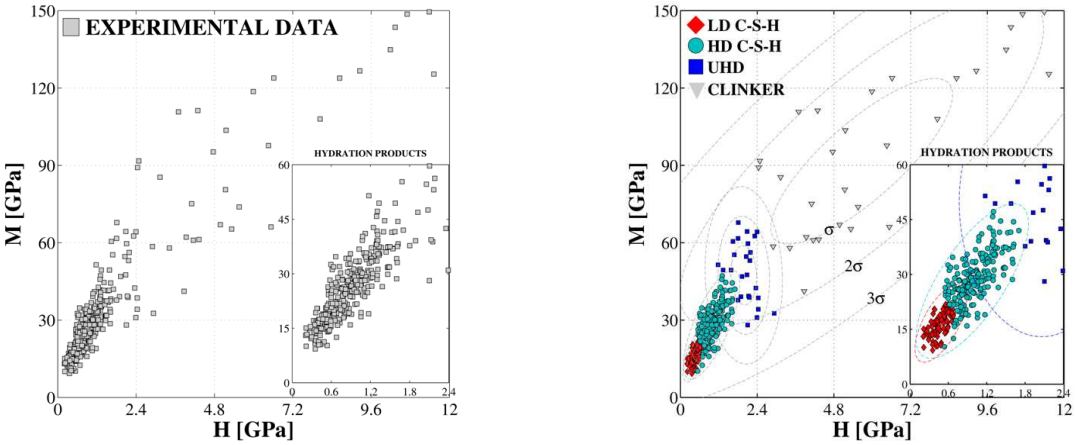

(a) (b)

Figure IV.5 Maximum Likelihood based deconvolution of the grid indentation data on OPC: a) global plot of the experimental records, with a zoom focus on the domain of hydration products, b) deconvoluted and clustered experimental data with biphasic nature of silica gels exposed. *H*-indentation hardness, *M*-indentation modulus.

It is evident on the global view, that the data cover a wide range of hardness values (up to 12 [GPa]) and indentation modulus (up to 150 [GPa]). However, the dominant fraction is concentrated in the subdomain with upper thresholds of *H*=5 [GPa] and *M*=60 [GPa], recognized to give the characteristic domain of cement hydration products *C-S-H*.[18,19] The applied bivariate mixture model to describe the OPC is based on the assumption of existence of four distinguishable, statistically significant components *g*=4, similarly to the estimation based on the c.d.f. function (Figure IV.4). It is also hypothesized, that among these components may be measurements that do not represent the real mechanical phase but rather can be classified as a 'statistical noise'. This issue will be addressed in the subsequent part. Referring to the deconvolution procedure, the application of the EM algorithm leads to the estimation of the mean values of each underlying component $\boldsymbol{\mu}_j$, the associated covariance matrices $\boldsymbol{\Sigma}_j$ and finally the weights π_j (Table IV.1). The execution of the expectation-maximization algorithm from a large number of different, randomly selected starting values of $\boldsymbol{\psi}$, indicated as $\boldsymbol{\psi}_{(0)}$, minimizes the possibility that the obtained solution represents only a local minimum.

Table IV.1 Mechanical phase properties of the OPC assessed with the ML based deconvolution

PHASE	H^1	σ_H	M^1	σ_M	$r_{H,M}{}^2$	φ^3	π
LD C–S–H	0.48	0.13	16.67	3.56	0.65	-1.42	0.22
HD C–S–H	0.97	0.29	28.24	7.03	0.73	-1.75	0.61
UHD	1.98	0.4	47.39	11.47	-0.07	0.15	0.08
CLINKER	5.67	2.84	91.62	32.09	0.80	-4.08	0.09

1-properties estimated in [GPa], 2-the linear (Pearson) correlation coefficient $r_{H,M}=cov(H,M)/(\sigma_H\sigma_M)$, 3-angle of inclination of the equal probability density ellipses $tan(2\varphi)=2cov(H,M)/((\sigma_H)^2-(\sigma_M)^2)$. Clockwise is positive and values are given in degrees of arc °.

The graphical representation of the ML estimation, as well as the result of allocation based on fitted posterior probabilities Eq. IV.21 to specific model groups, are demonstrated on Figure IV.5(b). According to these results, the biphasic nature of the hydration products is apparent, given by two independent clusters of experimental data. The distributions of records from both types of *C-S-H* components are characterized by positive *cov*(*H,M*). Additionally, the Pearson's correlation coefficient $r_{H,M}$ approaches ≈0.7, what suggests quite strong positive, linear dependence between hardness and elastic modulus within each *C-S-H* phase. The third component, namely *UHD*, may be considered as the composite phase which incorporates portlandite (*CH*) mineral. Its density distribution and related cluster are characterized by significant higher dispersion of the data points than the two previously described hydration products. Moreover, the close proximity of the Pearson's product to zero defines a marginal correlation of *H* and *M* for this phase. The last component is of experimental noise type, as a material noise, which incorporates atypical and rare observations, which fall out of the general trend and are spread over a large *H-M* domain. This set includes rare indentation records on unhydrated components of cement (Albite, Belite, C_3S, C_2S etc.), which are recognized to have indentation hardness in the following ranges *H*=7.0÷11.5 [GPa], *M*=100.0÷155 [GPa],[11,36] and other records that are considered as single measurements of composite response. Data categorized as inherent phases of cement based material represented by the three first components account for more than 90 % of the experimental records, leaving $\pi < 10$ % for the fraction of atypical and rare observations.

IV.4.3. Application to Fired Clay Brick

A second example of the ML application is the case of grid indentation carried out on masonry clay brick. This ceramic composite material exhibits a high degree of heterogeneity on multiple scales.[37,38,39] Massive grid indentation (Figure IV.6(a)) has been carried over a selected region of polished ceramic in order to obtain the mechanical characteristics of the brick constituents. The special focus has been put on the 'glassy' matrix and its mechanical properties as a function of indentation depth. The indentation grid covers the rectangular region with the approximate dimensions 110×40 [μm] and internal grid spacing l_x=l_y=2.0 [μm]. Multiple force-controlled measurements were executed with equal loading and unloading rates of 5.0 [mN/min]. The dwell time of 5.0 [s] has been chosen for the maximum force P_{max}=1.125 [mN].

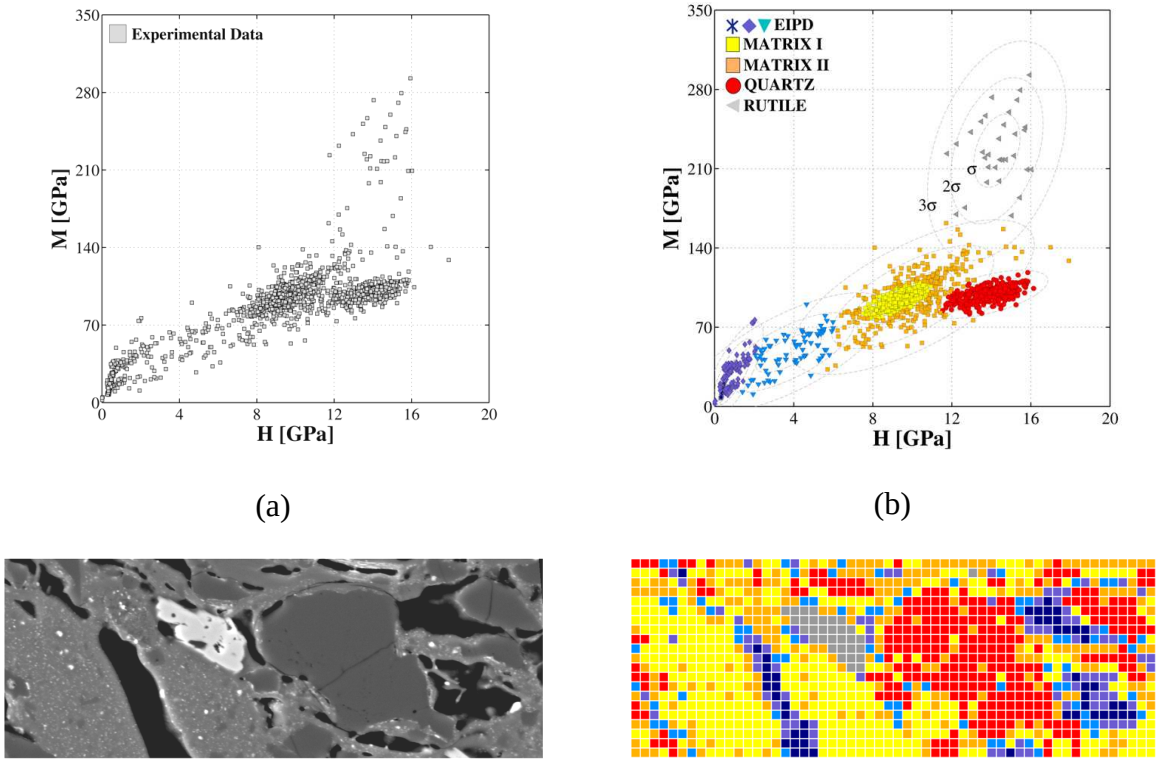

Figure IV.6 Grid indentation data on the facing brick: grid span 110×40 [μm], number of grid points i×j=21×56, spacing l_x=l_y=2.0 [μm]. Sample impregnated with epoxy resin: a) raw data set (abnormal observations included), b) deconvolution and clustering of experimental records, c) BSEM micrograph of investigated region, d) phase distribution reconstructed on the basis of the results of the cluster analysis. EIPD-epoxy impregnated porous domain.

The adopted Gaussian Mixture Model assumes the number of statistical groups equal to seven g=7. This choice for g is not arbitrary, but obeys the Bayesian Information Matrix (BIC) criterion proposed by Schwarz,[23,40] which provides g=7 as the number of phases with the highest probability to occur. A discussion on the influence of the number of phases on the results will be addressed below.

The deconvolution of the raw data, together with the allocation of the experimental records is presented in the form of the scatter diagram on $H\times M$ plane (see Figure IV.6(b)) and Table IV.2).

Table IV.2 Mechanical phase properties of the brick matrix and quartz assessed with the ML based deconvolution

PHASE	H^1	σ_H	M^1	σ_M	$r_{H,M}{}^2$	φ^3	π
MATRIX I	9.37	0.77	94.51	7.24	0.69	-4.23	0.30
MATRIX II	10.00	2.06	96.57	22.81	0.68	-3.54	0.26
QUARTZ	13.78	1.03	99.08	7.08	0.58	-4.87	0.24

1-properties estimated in [GPa], 2-the linear (Pearson) correlation coefficient $r_{H,M}=cov(H,M)/(\sigma_H\sigma_M)$, 3-angle of inclination of the equal probability density ellipses $tan(2\varphi)=2cov(H,M)/((\sigma_H)^2-(\sigma_M)^2)$, unit: degrees of arc °.

The presence of a very stiff and hard phase (with a left oriented grey triangular marker) is noticed, with the relevant properties H_7=14.28 [GPa] and M_7=225.86 [GPa], with moderate dispersion and $r_{H,M}$ approaching zero. This phase represents the single aggregate of titanium oxide based mineral (possibly rutile or anatase),[41,42] which is clearly seen on the Back Scattered Electron Microscopy (BSEM) micrograph (Figure IV.6(c)). This observation is also supported by the elemental distribution of titanium (see EDX map on Figure IV.7(f)), which exposes definitely its chemical origin. The next cluster with a relatively high value of hardness represents quartz (circle red marker).[43,44] A close inspection of EDX maps (Figures IV.7(a-f)) tends to strengthen this hypothesis. The estimated mechanical properties are H_6=13.78 [GPa] and M_6=99.08 [GPa] (Table IV.2). The obtained values represent the case of shallow indents P_{max}=1.125 [mN] and $h_{max}\approx$100 [nm]. However, the measured hardness approaches well the literature data reported for quartz of $H_Q\approx$14.00 [GPa] obtained at higher depths.[4] The measured indentation modulus is approaching the elastic stiffness reported for quartz mineral ($E_{11}\approx$79 [GPa], $E_{33}\approx$103 [GPa]),[44] however these two stiffness measures, M and E are not directly comparable for crystal materials due to present anisotropy. The variance

of indentation moduli is very small in comparison with the previous phase, indicating higher homogeneity of this set of observations. The calculated value of $r_{H,M}$ for this component is ≈0.58 and φ=-4.87 suggesting quite strong correlation of *H* and *M* in this cluster (Table IV.2).

The binding 'glassy' matrix, typical for the microstructure of the facing clay brick, is represented in this analysis by two components, e.g. square yellow and orange markers on Figure IV.6(b). This duality may be attributed to the variation in the local chemical composition as well as to the changes in the morphology and interaction with other mechanical phases. The first set of measurements related to the binding matrix (square yellow marker) is concentrated around the mean hardness H_I=9.37 [GPa] and lower modulus M_I=94.51 [GPa]. The indentations with the measurements allocated to this group are mostly located on the large chunk of the 'glassy' matrix pocket, although a minor fraction may be found outside this region as well (see Figures IV.6(c-d)).

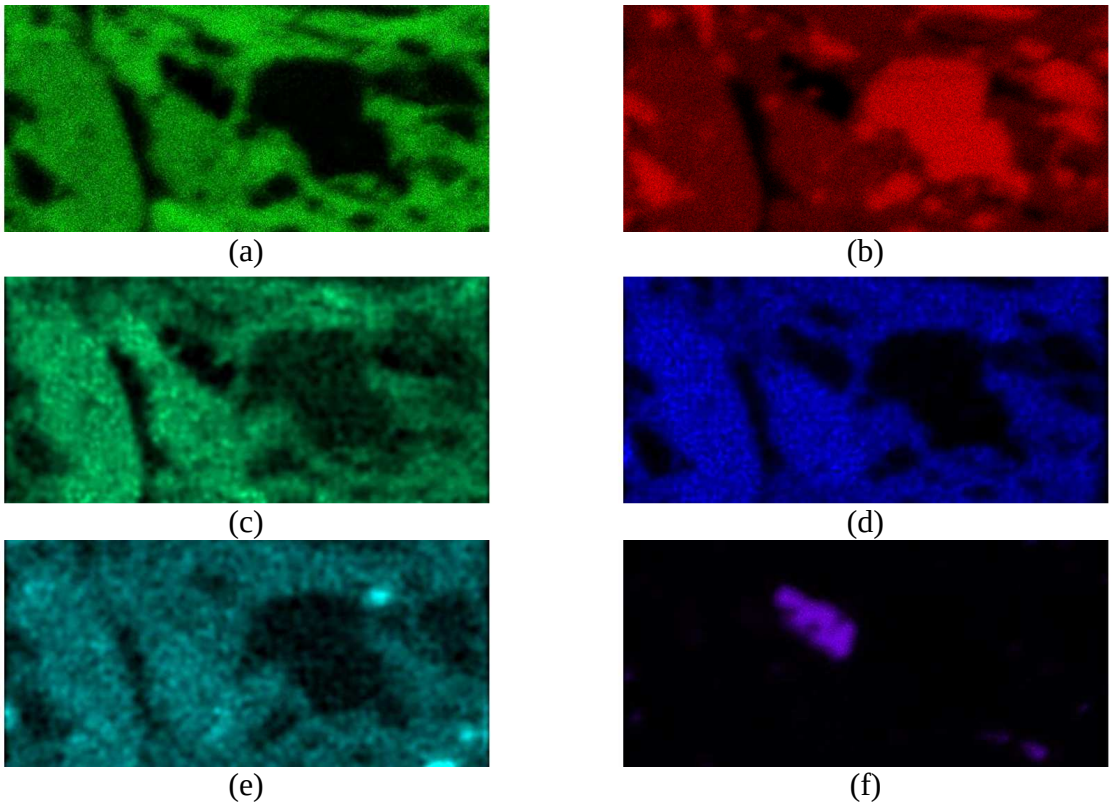

Figure IV.7 Distribution of elements within investigated region recorded in EDX microanalysis: a) *Al*, b) *Si*, c) *Mg*, d) *K*, e) *Ca*, f) *Ti*. Note the visible relatively large aggregates of quartz (SiO_2), the matrix pocket with characteristic higher concentration of alkaline elements (*K*, *Mg*, *Ca)*, the external matrix with relative higher concentration of alumina and low concentration of alkaline elements, and the single grains of titanium based mineral.

The continuity of this phase, together with improved homogeneity (at the scale of present indentation), tends to result in a relatively small variance of *H*, *M* and a small scatter of observations within the corresponding cluster. The EDX results collected over this particular region show higher concentration of the alkali elements, e.g. magnesium and potassium, than in the rest of the investigated area (Figures IV.7(c-d)). The estimated mechanical properties of the second type (square orange marker) H_{II}=10.00 [GPa] and M_{II}=96.57 [GPa] are slightly higher than its previous phase. In this case, the variance in both measured quantities increases considerably. The slight increase in *H* and *M* could be attributed to the higher concentration of the aluminum in the region surrounding the pocket of glass (Figure IV.7(a)). Additionally, the interaction with other mechanical phases of higher strength and stiffness, as well as possible higher variation in surface topography, may result in the larger variance and shift in the mode position of this component of the mixture model. A moderate correlation between the hardness and indentation moduli has been found for both groups, with $r_{H,MI}$=0.69 and $r_{H,MII}$=0.68. The assessed mechanical properties of the binding phase of facing clay brick fall in the range of aluminosilicate glass and glass ceramics.[1,45,46,47]

The last three statistical phases, identified with the ML based deconvolution represent the indentations executed on the epoxy impregnated porous domain (EIPD) or in its close neighborhood (Figure IV.6). Therefore, the measurements, which were mostly probing the bulk hardened epoxy resin (star dark blue marker), are concentrated around the mode representing the smallest hardness and indentation modulus values *H*=0.40 [GPa] and *M*=14.80 [GPa]. The two remaining groups include the indents executed in boundary zone between the resin and stiffer phases (Figure IV.6(d)). Under these circumstances, the interaction volume probed by the indenter incorporates the fractions of the stiffer phases in a random fashion. As a consequence, the measured properties become enhanced compared with the properties of the epoxy resin, and they tend to exhibit significant scatter. The local influence of the rounded edges together with changes in the surface profile at the interfaces may contribute to this dispersion as well. Note that ill conditioned measurements were found, e.g. fracture under the indenter and soft-on-hard behavior, which do not follow a $P \propto h^m$ relation and, in general, fall in the lower range of measured quantities. This type of abnormal observations could be easily identified, and these measurements establish an independent statistically relevant group (diamond blue marker) (Figure IV.6(b)).

The ML estimated surface fractions of each mechanical phase (Table IV.3) are compared with the results obtained by the Digital Image Analysis (DIA) of the micrograph pictured on

Figure IV.6(c). In this analysis the surface fraction of porosity represents the sum of the first three clusters with the lowest hardness values. A good agreement has been found between both methods, with the maximum divergence approaching 7 % for quartz phase.

Table IV.3 Comparison of the surface fractions estimated with ML approach and the results of the Digital Image Analysis (DIA) of the BSEM micrograph of the indented region (Figure IV.6(c)).

	π-surface fraction			
	matrix	quartz	rutile	porosity
ML[1]	0.558	0.240	0.028	0.174
DIA[2]	0.572	0.225	0.028	0.175
$\Delta[\%]$[3]	2.450	6.670	0.000	0.570

1–original estimation with included abnormal observations, 2–image resolution: 1pix≈0.09 [μm], 3–$\Delta = |\pi_{DIA} - \pi_{ML}| / \pi_{DIA}$

IV.4.4. Inference of the Number of Components

In the field of Gaussian Mixture Models, for the definition of the adequate number of components g is a difficult problem which has not been completely resolved. Several penalized log likelihood criteria have been developed and are commonly reported in the literature.[23,28,29] One of them is Bayesian Information Criterion (BIC) proposed by Schwartz,[40] which has been applied in this work. Accordingly, the number of components g with the highest probability to occur minimizes the statistic given by:

$$\log L_g(\hat{\psi}) - \tfrac{1}{2} k_g \log N \qquad \text{IV.22}$$

where $L_g(\hat{\psi})$ is the likelihood function for model g, k_g is the number of model parameters and N is the size of the sample. The results of the assessed BIC statistic with respect to the number of model's components g are presented below for all three introduced materials: naval brass, cement paste and clay brick (see Figure IV.8(a)).

While in Section IV.3.1 the deconvolution of naval brass has been carried out under the assumption of two components, the new results (Figure IV.8(a)) require the refinement of the model into three groups. The new component includes most of the observations located outside the 3σ equal probability density contours of the main phases (Figure IV.8(b)). The

new phase is also characterized by a much higher variance in the measured properties as well as significantly lower weight. It is hypothesized, that it does not represent a physical phase, but rather measurements with unrecognized ill conditioned nature or affected by local phenomena, e.g. chemical composition or surface profile. But it is stressed, that the incorporation of this so called 'noise' component improves the accuracy in the estimations of hardness and indentation modulus of two physically relevant mechanical α- and β-phases.

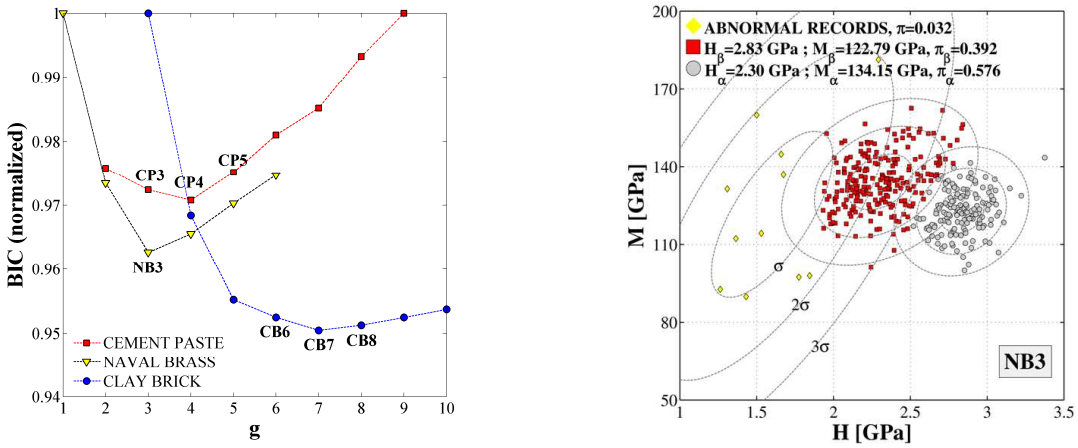

(a) (b)

Figure IV.8 Assessment of the number of model's components for investigated materials based on the BIC statistics: a) evident global minimum g=3 for naval brass, g=4 for cement paste and g=7 for clay brick, b) deconvolution of naval brass experimental data under the assumption of GMM composed of three components.

The OPC mixture model with $g = 4$ components minimizes BIC criterion (Figure IV.8(a)). The successive deconvolution refinement of the cement paste model into three (CP3) and five (CP5) phases is presented below for the sake of discussion (Figures IV.9(a-b)). It is evident, that for g=3 the general pattern of the data is clearly outlined, which incorporates the hydration product family, the portlandite family and the set of rare indentation events on unreacted clinker. Addition of one more component, minimizes BIC and exposes the duality of *C-S-H* gel (Figure IV.5(b)). Further refinement with $g > 4$ does not alter the grouping within *C-S-H*, but splits the last component (Figure IV.9(b)) leading to a drastic increase of the BIC statistic.

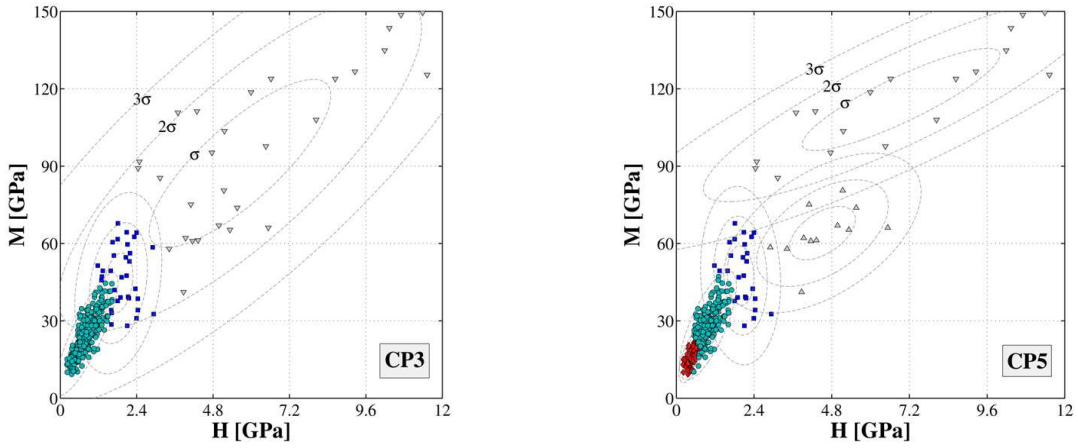

(a) (b)

Figure IV.9 Successive deconvolution refinement of the cement paste grid indentation data: a) *g*=3, b) *g*=5 components.

The GMM with seven normal components minimizes the Schwartz statistic for the clay brick indentation measurements. Although, the contrast in BIC value from six to eight components is quite small, visible and significant changes may be noticed in related distributions and a posteriori clustering (Figures IV.6(b) and IV.10(a-b)).

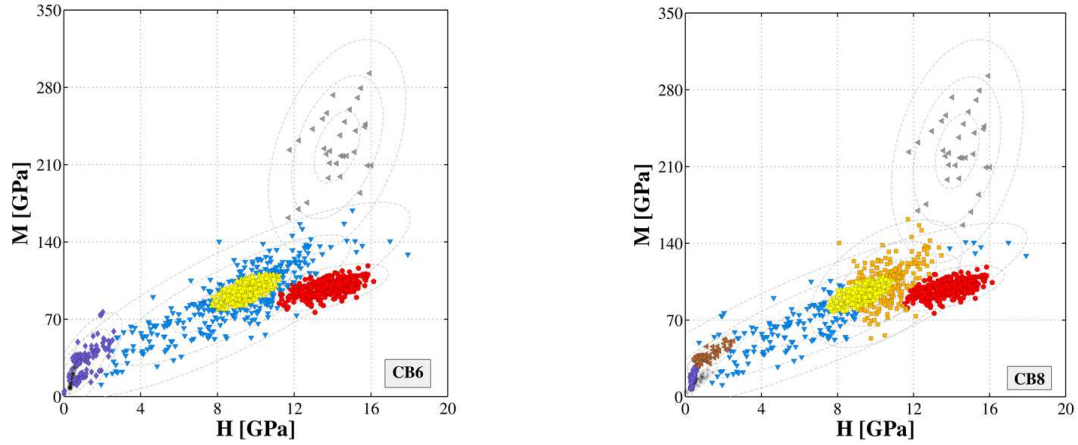

(a) (b)

Figure IV.10 Successive deconvolution refinement of the clay brick grid indentation data: a) *g*=6, b) *g*=8 components.

The first mixture model recognizes only one cluster corresponding to matrix phase and enlarges the distribution component related to the epoxy impregnated domain of voids. This enlarged cluster spans over large domain of *H* and *M* and wrongly incorporates indentations

carried on matrix. Under these circumstances the estimated weights deviate drastically from the results obtained with DIA, e.g. $\pi_M \approx 33$ %, $\pi_{porosity} \approx 40$ % comparing to $\pi_M \approx 57$ %, $\pi_{porosity} \approx 17$ %. The proper estimation of weights, as well as better separation of phases, corresponds to the model with seven components, which minimizes BIC criterion. Its physical notion has been grounded additionally by the EDX analysis as well as direct comparison of BSEM micrograph (Figure IV.6(c)) with its probabilistic reproduction based on the corresponding clustering results (Figure IV.6(d)). Finally, the construction of a more complex model leads to exposure of local distributions within already identified (Figure IV.10(b)). Such sparse solutions increase the BIC value and appear in the group of records related with the epoxy impregnated porosity domain.

IV.5. COMPARISON OF THE METHODS

The introduced maximum likelihood deconvolution approach (MLA) is defined over $\Re^2$ space, where the model components are represented by a bivariate normal distribution function $f(\boldsymbol{x}|\boldsymbol{\mu},\boldsymbol{\Sigma})$ that includes variance-covariance matrix $\boldsymbol{\Sigma}$ in its complete form. Such an approach differs fundamentally from the strategies briefly reviewed at the beginning of this manuscript, which work with discrete values and univariate mixture models. Consequently, the estimated parameters obtained with these methods differ in the level of accuracy.

Table IV.4 Deconvolution of the indentation data on naval brass with different methods of estimation applied.

		α–phase					β–phase				
		H^1	σ_H	M^1	σ_M	π	H^1	σ_H	M^1	σ_M	π
PDF[2]	$2h_0$	2.32	0.23	131.85	14.45	0.64	2.95	0.11	125.91	7.33	0.36
	h_0	2.27	0.22	134.41	11.07	0.59	2.83	0.15	122.85	8.24	0.41
	$h_{0/2}$	2.25	0.20	135.66	11.51	0.55	2.81	0.15	123.38	8.17	0.45
CDF		2.24	0.20	133.45	12.20	0.56	2.81	0.15	124.44	9.03	0.44
MLA[3]		2.29	0.29	133.28	12.96	0.64	2.84	0.13	122.11	7.82	0.36
MLA[4]		2.30	0.21	134.15	10.72	0.59	2.83	0.15	122.79	8.30	0.41
CV(%)		1.34	15.07	0.95	11.38	6.44	1.86	11.95	1.12	6.91	9.47

1 – properties estimated in [GPa], 2 – different size of the histogram intervals, 3 – two-component model which does not correspond to *min*(BIC) which is attained for g=3, 4 – estimated values for min(BIC) model with g=3.

Next, the parameters of naval brass and OPC estimated with the p.d.f. and c.d.f. based methods are confronted with the solution obtained by making use of the proposed strategy (Tables IV.4 and IV.5). The clay brick grid indentation is excluded from this brief comparative analysis, even if the MLA seems to provide also good results for this material. The large number of components in clay brick effectively complicates the estimation with the two first methods, whose application tends to be restricted to less enlarged mixture models. Note also that p.d.f. is not applied to OPC because of the known influence of the size of the histogram interval on the value of estimated parameter.

Table IV.5 Properties of hydration products estimated with different methods.

		LD C–S–H					*HD C–S–H*				
		H^1	σ_H	M^1	σ_M	π	H^1	σ_H	M^1	σ_M	π
CDF[2]	A	0.51	0.15	16.44	3.20	0.23	0.95	0.29	27.76	6.08	0.55
	B	0.51	0.14	16.45	2.84	0.18	0.92	0.31	27.66	6.86	0.60
MLA[3]		0.48	0.13	16.67	3.56	0.22	0.97	0.29	28.24	7.03	0.61
CV(%)		3.46	7.14	0.79	11.25	12.60	2.66	3.89	1.11	7.61	5.48

1 – properties estimated in [GPa], 2 – with phase contrast condition incorporated (A), with phase contrast condition released (B), 3 – four-component mixture model.

It may be seen, that the estimated properties holds consistency regardless the applied method and with reference to the mean values of H and M (naval brass: CV_H<2.0 %, CV_M<1.5 %, *OPC*: $CV_{H\ C\text{-}S\text{-}H}$ < 3.5 %, $CV_{M\ C\text{-}S\text{-}H}$ < 1.5 %). However, the estimation of standard deviations and consequently the components weights deviate significantly comparing to the solution obtained with MLA. The variations in these two estimators across the methods are much greater (naval brass: $CV_{\pi\alpha}$≈7 %, $CV_{\pi\beta}$≈11 %, *OPC*: $CV_{LD\ C\text{-}S\text{-}H}$≈13 %, $CV_{HDC\text{-}S\text{-}H}$≈5.5%). It may be also noticed from the results reported in Table IV.4, that the p.d.f. based estimation for which the bin size equals $2h_0$ gives the same results as the MLA (g=2) in terms of standard deviation and surface fraction. However, in the further refinements of the histogram (h_0, $h_{0/2}$) this approach tends to overestimate the β-phase of brass, while underscoring the remaining α-phase. This observation shows that the change in the size of the bin or shift in the histogram initial point automatically changes the probability discrete values and empirical distribution, leading to no negligible impact on the estimated parameters.[22,25] Likewise the bin size, the phase separation condition incorporated into the c.d.f based deconcolution method may lead to noticeable distortions of standard deviations estimators and components weights

(Table IV.5), in comparison with the MLA solution. This effect is expected to be more pronounced in the grid indentation results where the significant mixing of the components takes place, e.g. weak fulfillment of the phase separation condition or unsatisfactory sample preparation. In such a situation, the correct overlap of two successive Gaussians may not follow $\mu_j^x+s_j^x \leq \mu_{j+1}^x-s_{j+1}^x$. From this perspective, it appears reasonable to neglect the 'phase contrast condition', such as in the example of indentation grid analysis on ceramic materials reported by Guicciardi et al.[48], and allow the minimization procedure to be solved in its general form like in the usual case. Besides, a condition like this specifies particular order of phases within investigated material, namely each phase can only have an indentation modulus and hardness greater than the one before, which is a hypothesis without physical ground. This ordering is only one among many possible, which may be encountered in the indentation on the heterogeneous materials.

IV.6. CONCLUSIONS

The statistical grid indentation technique on heterogeneous materials has been substantially extended with the implementation of the mulitvariate Gaussian Mixture Model and Maximum Likelihood concept as a primary tool in the deconvolution analysis. It has been shown that bivariate modeling and the ML estimation approach together with the Expectation Maximization algorithm offers a robust and efficient deconvolution strategy. This fact has been demonstrated on the examples of a simpler metallic material, namely naval brass, as well as more complex cohesive-frictional materials, namely ordinary Portland cement paste and masonry clay brick. Under the assumption of independent and identically distributed realizations of random variables, the maximum likelihood estimation of phase properties, theirs covariance matrices and surface fractions have been found. The obtained values show good agreement with the data reported in the literature. While the estimations of mean phase properties are quite coherent among the reviewed methods and ML approach, a significant improvement on the estimation of the components weight has been found. Additionally, the introduced deconvolution strategy permits to execute data clustering and to expose its internal structure. Therefore, the allocation of indentation records to specific components based on a posteriori probability may be carried. As a result, the statistical map of the material in the investigated region may be drawn on a pure probabilistic basis. This technique has been demonstrated for the clay brick indentation experiment, where the BSEM micrograph and EDX elemental maps have been compared with the results of cluster analysis. In this way,

each indentation may be directly linked to the local chemical composition. Besides this, the abnormal measurements may be pinpointed and possibly associated with particular features of the surface in its location or local composition. This group includes all observations, which are loaded with an experimental error of different nature, as well as rare indentation events which number is too small to establish a statistically significant and homogenous group. The typical characteristics of this group are the relatively large scatter and the tendency to exhibit a uniform distribution within a specific region of $H \times M$ plane. In addition, the influence of the abnormal observations on the estimated parameters may be quantified, and appropriate corrections can be introduced.

In the frame of the proposed strategy, the most probable number of components compatible with the analyzed grid indentation data may be inferred with the BIC estimator. This fact may be of major importance if no prior information regarding the phase composition is available, or subgrouping of the phases is encountered, like in the case of ordinary cement paste. In this material the BIC statistics has attained its minimum for the model which exposes duality of the Calcium Silica Gel, being in full agreement with the results of other independent measures and theoretical models.

IV.7. REFERENCES

[1]I. J. McColm, Ceramic Hardness, Plenum Press, New York (1990).

[2]D. Tabor, The Hardness of Metals, Oxford Classical Text in the Physical Sciences (2000).

[3]E. E. Gdoutos, Fracture Mechanics, An Introduction, Solid Mechanics and Its Application, Springer Netherlands, Volume 123 (2005).

[4]W. C. Oliver, G. M. Pharr, “An improved technique for determining hardness and elastic modulus using load and displacement sensing indentation experiments,” J. Mater. Res., 7 1564-83 (1992).

[5]K. S. Tai, H. J. Qi, and C. Ortiz, ‘‘Effect of Mineral Content on the Nanoindentation Properties and Nanoscale Deformation Mechanisms of Bovine Tibial Cortical Bone,’’ J. Mater. Sci.-Mater. Med., 16 947-59 (2005).

[6]D. M. Ebenstein, L. A. Pruitt, “Nanoindentation of biological materials,” NanoToday, 1 26-33 (2006).

[7]Z. H. Xu, D. Rowcliffe,” Nanoindentation on diamond-like carbon and alumina coatings,” Surf. Coat. Tech., 161 44-51 (2002).

[8]D. Drechsler, A. Karbach, H. Fuchs, "Nanoindentation on polycarbonate-polymethyl methacrylate Blends," Appl. Phys. A, 66 825-829 (1999).

[9]T. Gómez-Del Río, P. Roza, J. Rodríquez, "Micromechanical characterization of Al 8090/SiC composites by nanoindentation," J. Mater. Sci., 40 1513-1515 (2005).

[10]H. Engqvist, U. Wiklund, "Mapping of mechanical properties of WC–Co using nanoindentation," Tribology Letters, 8 147-152 (2000).

[11]G. Constantinides, Invariant Mechanical Properties of Calcium-Silicate-Hydrates (C-S-H) in Cement-Based Materials: Instrumented Nanoindentation and Micromechanical Modeling, MIT, PhD Thesis (2006).

[12]F. -J. Ulm, Y. Abousleiman, "The nanogranular nature of shale," Acta Geotechnica, 1 77-88 (2006).

[13]F. Hill, "'Elastic properties of reinforced solids: some theoretical principles," J. Mech. Phys. Solids, 11 357-372 (1963).

[14]G. Constantinides, K. S. Ravi Chandran, F. -J. Ulm, K. J. Van Vliet, "Grid indentation analysis of composite microstructure and mechanics: Principles and validation," Mat. Sci. Eng. A, 430 189-202 (2006).

[15]F. -J. Ulm, M. Vandamme, C. Bobko, J. A. Ortega, K. Tai, C. Ortiz, "Statistical Indentation Techniques for Hydrated Nanocomposites: Concrete, Bone and Shale," J. Am. Ceram. Soc., 90 2677-2692 (2007).

[16]L. Sorelli, G. Constantinides, F. -J. Ulm, F. Toutlemonde, "The nano-mechanical signature of Ultra High Performance Concrete by statistical nanoindentation techniques," Cem. Con. Res., 12 1447-1456 (2008).

[17]G. Constantinides, F. -J. Ulm, K. J. Van Vliet, "On the use of nanoindentation for cementitious materials,"Mater. Struct., 36 191-196 (2003).

[18]G. Constantinides, F. -J. Ulm, "The nanogranular nature of C–S–H," J. Mech. Phys. Solids, 55 64-90 (2007).

[19]M. J. DeJong, F. -J. Ulm, "The nanogranular behavior of C-S-H at elevated temperatures (up to 700 °C)," Cem. Con. Res. 37 1-12 (2007).

[20]M. Delesse, "Procédé mécanique pour déterminer la composition des roches," C. R. Acad. Sci. 25 544-547 (1847).

[21]R. E. Walpole, R. H. Myers, Probability and Statistics for Engineers and Scientists, 5th edition, Macmillan Publishing Company (1993).

[22]J. Kornacki, J. Mielniczuk, Statistics for Students of Natural and Technical Sciences, (in polish), 3rd edition, WNT (2006).

[23]G. J. McLachlan, D. Peel, Finite Mixture Models, Wiley Series in Probability and Statistics, A Wiley-Interscience Publication (2000).

[24]D. W. Scott, “On Optimal and Data-Based Histograms,” Biometrika, 66 605-610 (1979).

[25]L. Gajek, M. Kałuszka, Statistical Inference: Models and Methods, (in polish), WNT, 4th edition (2000).

[26]N. X. Randall, M. Vandamme, F. -J. Ulm, “Nanoindentation analysis as a two-dimensional tool for mapping the mechanical properties of complex surfaces,” J. Mater. Res., 24 679-690 (2009).

[27]M. Vandamme, The Nanogranular Origin of Concrete Creep: A Nanoindentation Investigation of Microstructure and Fundamental Properties of Calcium-Silicate-Hydrates, MIT, PhD Thesis (2008).

[28]G. J. McLachlan, K. E. Basford, Mixture Models, Inference and Applications to Clustering, Statistics: Textbooks and monographs, volume 84, Marcel Dekker, Inc., New York (1988).

[29]D. M. Titterington, A. F. M. Smith, U. E. Makov, Statistical Analysis of Finite Mixture Distributions, Wiley Series in Probability and Mathematical Statistics, John Wiley & Sons (1985).

[30]A. P. Dempster, N. M. Laird, D. B. Rubin, “Maximum Likelihood from Incomplete Data via the EM Algorithm,” J. Roy. Stat. Soc. B. Met., 39 1-38 (1977).

[31]C. R. Rao, “The utilization of multiple measurements in problems of biological classification,” J. Roy. Stat. Soc. B. Met., 10 159-203 (1948).

[32]G. J. McLachlan, “Cluster analysis and related techniques in medical research,” Stat. Methods Med Res., 1 27-48 (1992).

[33]G. J. McLachlan, T. Krishnan, The EM Algorithm and Extension, Wiley Series in Probability and Statistics, 2nd edition, John Wiley & Sons (2008).

[34]G. J. McLachlan, D. Peel, K. E. Basford, P. Adams, “The EMMIX software for the fitting of mixtures of normal and t-components,” J. Stat. Soft., 4 (1999).

[35]EMMIX code webpage, http://www.maths.uq.edu.au/~gjm/emmix/emmix.html.

[36]K. Velez, S. Maximilien, D. Damidot, G. Fantozzi, F. Sorrentino, "Determination by nanoindentation of elastic modulus and hardness of pure constituents of Portland cement clinker,” Cem. Con. Res., 31 555-561 (2001).

[37]A. J. Flynn, Z. H. Stachurski, “Microstructure and properties of stoneware clay bodies,” Clay Min., 41 775-789 (2006).

[38]B. Bauluz, M. J. Mayayo, A. Yuste, C. Fernandez-Nieto, J. M. Gonzalez Lopez, "TEM study of mineral transformations in fired carbonated clays: relevance to brick making," Clay Min., 39 333-344 (2004).

[39]G. Cultrone, E. Sebastián, K. Elert, M. J. de la Torre, O. Cazalla, C. Rodriguez-Navarro, "Influence of mineralogy and firing temperature on the porosity of bricks," J. Eur. Ceram. Soc., 24 547-564 (2004).

[40]G. Schwarz, "Estimating the Dimension of a Model," Ann. Stat., 6 461-464 (1978).

[41]J. G. Berryman, "Bounds and self-consistent estimates for elastic constant of random polycrystals with hexagonal, trigonal, and tetragonal symmetries," J. Mech. Phys. Solids, 53 2141-2173 (2005).

[42]I. Gheewala, R. Smith, S. D. Kenny, "Nanoindentation and nanoscratching of rutile and anatase TiO_2 studied using molecular dynamics simulations," J. Phys. Condens. Matter., 20 (2008).

[43]W. Zhu, J. Hughes, N. Bicanic, C. J. Pearce, "Nanoindentation mapping of mechanical properties of cement paste and natural rocks," Mater. Charact., 58 1189-1198 (2007).

[44]P. Heyliger, H. Ledbetter, S. Kim, "Elastic constants of natural quartz," J. Acoust. Soc. Am., 114 644-50 (2003).

[45]M. W. Barsoum, Fundamentals of Ceramics, Series in Material Science and Engineering, IoP (2003).

[46]T. Rouxel, "Elastic properties of glasses: a multiscale approach," C. R. Mecanique, 334 743-753 (2006).

[47]C. -C. Lin, L. Liu, "Composition dependence of elasticity in aluminosilicate glasses," Phys. Chem. Miner., 33 332-46 (2006).

[48]S. Guicciardi, C. Melandri, L. Silvestroni, D. Sciti, "Indentation grid analysis of nanoindentation bulk and in situ properties of ceramic phases," J. Mater. Sci., 43 4348-4352 (2008).

V. Probing of the Building Brick Microstructure by Means of Instrumented Indentation Method: In-situ Assessment of Hardness and Elastic Properties of the 'Glassy' Matrix

ABSTRACT

The main focus of the work presented here is the experimental analysis of the elastic properties and the hardness of the polycrystalline-amorphous bond, the main component of the fired clay brick microstructure. The Young's modulus of this composite, together with the indentation hardness, is assessed with the aid of instrumented indentation executed at sub-micron scale. Different force regimes are investigated, and the evolution of both properties with respect to the depth of indentation is investigated. The gathered results corroborate the composite nature of the 'glassy' bond, in which the stiffness and hardness become enhanced due to mutual interplay between aluminosilicate glass and reinforcing neo-crystal phases. Additionally, the mechanical properties of the accessory phases like quartz, incorporated within the brick microstructure, are inferred.

V.1. INTRODUCTION

Ceramic materials have been inherently present in the human culture, being a part of mankind development process and growth of civilizations. The easy access to abundant resources of raw materials concentrated in the earth crust, the processing simplicity and the attractive final properties made ceramics suitable for many applications in different fields. Non-surprisingly one of the first applications of the fired-clay solids, where their superior properties above other available materials have been recognized, was housing. The oldest fired bricks applied in the construction of habitats have been found in Knossos (Crete) and dated back to around 4300 BC.[1] They effectively replaced the sun dried bricks which had tendency to disintegrate easily under humid atmosphere.[2] Therefore, the life-expectancy of buildings, together with their comfort, was significantly improved while elevating the status of inhabitants. The potential of ceramics used as a construction material has been appreciated since then.

Naturally, the understanding the processes, which allow building bricks to develop given physical and mechanical properties, became a subject of intensive research. This is particularly true in the last decade, as the demand for sustainable and environmental friendly construction materials is substantially increasing. It is known that, next to concrete or steel, structural ceramics have a high environmental footprint due to the energy consumption in manufacturing. The production of one ton of bricks releases around 250 kilograms of CO_2 to the atmosphere.[3,4] This is only a quarter of Portland cement, but in a comparison with concrete, the emission of carbon dioxide for structural ceramics is almost the double, per kilogram of bulk material. Ceramics is one of the most energy-intensive building materials. Hence, a good understanding of the link between industrial processes, composition and microstructure is required in order to reduce energy consumption, and tailor the properties of the material to our needs. In order to reach this goal, the study of the mechanical performance of brick microstructure elements with respect to composition and mechanical loads applied is relevant to modern masonry as well as to ceramics sciences in general.

In the brick complex material system one of the primary components is the polycrystalline-amorphous ‘glassy’ matrix created on the basis of the solidified, viscous melt. Its volume fraction and phase composition are governed by the composition of the starting materials as well as the temperature processing history. Obviously, apart from other existing factors, its mechanical performance drives much of the elastic behavior and strength of brick, properties known by engineers and applied at the structural level.

Until recently, the available methods in experimental mechanics could not provide access to the material bulk at sub-micron scale. However, the rapid progress in the experimental instrumentation brought depth-sensing indentation technique tailored for the nano- and micro-scale mechanical characterization of solids. This relatively new and promising method, combined with advanced statistics, has become a much versatile tool for the non-destructive characterization of heterogeneous materials at different scales. This experimental approach is especially useful when the bulk of material occupies very small volumes and its spatial distribution is random. These two attributes are typical of the brick 'glassy' matrix, which is a load bearing phase that forms complex 3-D scaffolds with a characteristic scale in the order of 10^{-4} [m] and randomly arranged in space.

The work reported here is focused on the experimental identification of the mechanical properties of the 'glassy' matrix existing within the brick by means of multiple depth-sensing experiments and advanced statistical analysis. Due to the random distribution of the 'glassy' matrix bulk, the depth-sensing measurements are executed in the nodal points of the grids, which cover specific regions of material or in randomly selected areas. The indentation moduli, as well as the indentation hardness, are estimated for each grid point from the depth-load curve according to the Oliver-Pharr method.[5] The mean properties are estimated with the Maximum Likelihood function applied to a statistical Gaussian Mixture Model (GMM).[6] The short description of the investigated brick microstructure is presented together with the chosen experimental approach. Finally, the obtained results are presented and supplemented with a detailed discussion.

V.2. MATERIALS

V.2.1. Microstructural Order, Phase Composition and Dimensional Characteristics

The investigated polycrystalline-amorphous 'glassy' matrix is one of the principal components of the facing brick fired in the ~55 hour-cycle using a gas fueled industrial kiln with the peak temperature 1050 [°C] (Figure V.1(a)). This load bearing material phase, which at the macro-level appears to be homogenous in nature,[7] hosts neo formed crystals of nanometer size $d_0<10^{-6}$ [m] (Figure V.1(b-d)) formed in the phase transformations at the expenses of the parent clay mineral or as a mixture of clay minerals and fluxes.

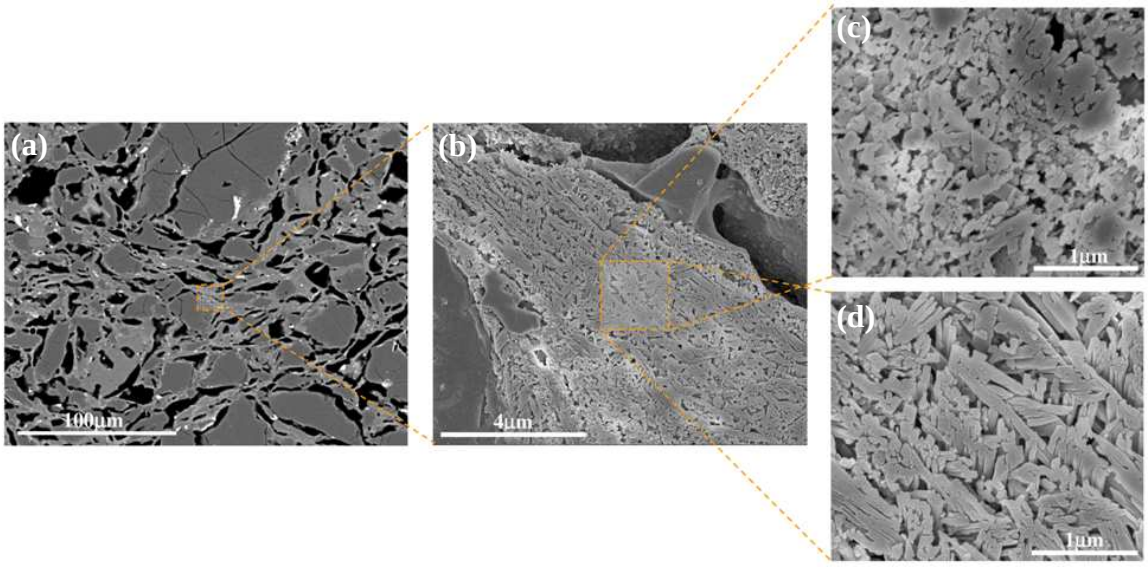

Figure V.1 Multi-component microstructure of facing brick (Back-scattered electron microscopy, BSEM): a) view on the macro scale, b) polycrystalline nature of the 'glassy' bond phase (sample etched with 6 % Hydrofluoric Acid, HF, for 1 [min]), c,d) detailed view on two apparently different morphologies of neo-crystal phases for mullite.

The dominant neo-crystals hosted in the aluminosilicate melt are the spinel-type phase and mullite crystals as well as the precipitated phases, like fine grained hematite, rutile, etc.. The first mentioned crystals are obtained from the kaolin mineral after breaking down the metakaolin at $T \approx 925 \div 980$ [°C],[8,9] or from crystallization of mica minerals at $T \approx 850 \div 950$ [°C].[10,11] This cubic spinel-type structure was considered an aluminum silicon *Al-Si* spinel,[9] however later studies carried by Sonuparlak[12] on well-crystallized kaolinite with TiO_2 impurity showed γ-Al_2O_3 as a bearing component with some residual SiO_2. Its crystal size strongly depends on the peak temperature and duration of the heat treatment cycle. Therefore, the crystalline regions of spinel formed at 980 [°C] may be as small as a few nanometers (5÷8 [nm]), as revealed in the beam-induced in-situ heating TEM studies.[12] On the other hand, for the same peak temperature but substantially prolonged heat treatment (1 day), a one order increase (≈100 [nm]) in the spinel crystal size may be observed. Crystals of spinel larger than those originated from kaolinite clays are crystallized from the clays which incorporate mica (illite, muscovite). The spinel crystals developed upon heating for 3 [h] at 900 [°C] are reported to be in the size of ≈20÷50 [nm] long and ≈5 [nm] wide,[13] to be oriented, and to be embedded in the silica- and potassium-rich matrix. Further increase in the firing temperature leads to the more intense development of amorphous matrix as well as

coarsening of the existing spinel ≈100×10 [nm] and precipitation of the hematite and rutile crystals ≈200 [nm] (at 1100 [°C]).[13]

The development of the spinel phase is followed by the crystallization of the mullite in the exothermic reaction around ≈1050 [°C] for pure kaolinite.[9] For complex mixtures with muscovite and quartz incorporated, mullite has been detected for temperature ≥900 [°C] and in significant volume fractions at ≈1000 [°C].[14,15] The morphology, stoichiometry and composition of the developed mullite crystals are complex functions of the starting materials and the processing conditions. Therefore, mullite crystals display various *Al* to *Si* ratios according to $Al_{4+2x}Si_{2-2x}O_{10-x}$, with x=[0.2;0.9][16] as well as various crystal dimensions.[17,18,19] Still, the division in primary and secondary mullite is usually accepted.

Primary 2:1 mullite is the first to derive from the clay laths, while secondary 3:2 mullite is formed from interaction of clay and fluxes. The primary mullite derived from the kaolinite clay relicts takes the form of fine cuboidal crystals (<100 [nm]). The secondary form, grown in the regions with impurities from feldspar, takes the form of needle shaped crystals, which may reach up to 1 [μm] in length,[14,17,18,19,20] depending on the initial size of clay particles, temperature, firing time applied and the local chemical potential of the melt. The crystals of acicular morphology are revealed in the back-scattered electron micrographs (BSEM) of the investigated material matrix (Figure V.1(c-d)) with an approximate size ≈500 [nm]. Their exact shape and dimensions are blurred by the complexity of 3D microstructural order.

The existing neo-crystals of spinel type cubic phase, as well as the mullite acicular crystals and hematite, are bound together by mutual interlocking (mechanical bonding), but, more important, by the solidified aluminosilicate glass. This glass phase develops from the amorphous silica SiO_2 and clay impurities released during the formation of the spinel type cubic phase as well as the crystallization of mullite. Enrichment of the system with silica melt decreases the eutectic point of the potassium feldspar flux,[21] leading to more pronounced liquid development rich in alkali elements and free alumina. Upon cooling, the viscous melt transform to amorphous glass. However, significant undercooling of the melt may induce nucleation and growth of new fraction of mullite crystals with a random orientation. These later crystals have finer structure than those formed primary.[13,14,17]

V.2.2. Surface Preparation Protocol and Areal Parameters

Small volume samples of the bulk were cut from the central part of the brick using a diamond drop saw to an approximate size of 1×1×0.5 [cm]. Subsequently, ultrasonically

cleaned and oven dried specimens were impregnated under vacuum (3 cycles vacuum-to-atmospheric pressure) with a low viscosity epoxy resin, EpoThin (5:2) of Buehler. Prior to the impregnation, the epoxy resin had been carefully warmed up to decrease its viscosity further. Moreover, in order to amplify the penetration of the porous solid by the viscous filler, pressurization with air (≈0.6 [bar]) for about 30 [min] was applied at the final stage of the impregnation process. Upper and lower faces of the sample were ground using a diamond disc Apex DGD Buehler with grit size 45 [μm], with subsequent cleaning in the ultrasonic water bath and drying prior to mounting in the metal holder with a cyanoacrylate agent.

Fine polishing has been carried out down to 0.25 [μm] and using 9 [μm], 3 [μm] and 1 [μm] diamond abrasive, with the aid of a metal jig and a lapping wheel. A detailed description of this procedure can be found in Miller et al..[22] Water based diamond solutions were sprayed on the hard perforated pads TexMetP Buehler. After each pass, ultrasonic cleaning was carried out before advancing any further. Such a procedure led to a rather clear 'mirror' like reflection, which could be observed by visual inspection. However, the surface quality was inspected using an atomic force microscope (AFM) operating in the contact tip mode (see Figure V.2), as well as a scanning electron microscope (SEM) (Figure V.3(a-b)). The surface topographic data were then collected over several spots of approximate size 70×70 [μm] and smaller.

The surface roughness S_a and the mean-squared roughness S_q were estimated over selected regions of interest (ROI) on the bulk (see Figure V.2), according to the ISO 25178 standard,[23] giving the average values of around ≈33 [nm] and ≈44 [nm], respectively. However, as seen in the image above and the SEM micrographs (Figure V.3(a-b)), the effect of relief is present. The hardened epoxy resin of significantly lower hardness H≈0.3 [GPa], present within the porous domain (EIPD), is removed in a higher fraction than the proper bulk with H≈6 [GPa] and above. Therefore, the surface of the epoxy filler is not leveled with the surface of the substrate. The difference may reach up to a few microns giving the impression of 'empty' voids or significant surface irregularities. In addition, local collapse and fracture (F1, F2 on Figure V.3(a-b)) of the proper bulk or matrix phase may be observed as well as the so called 'comet tails' (C1) or single empty pores.

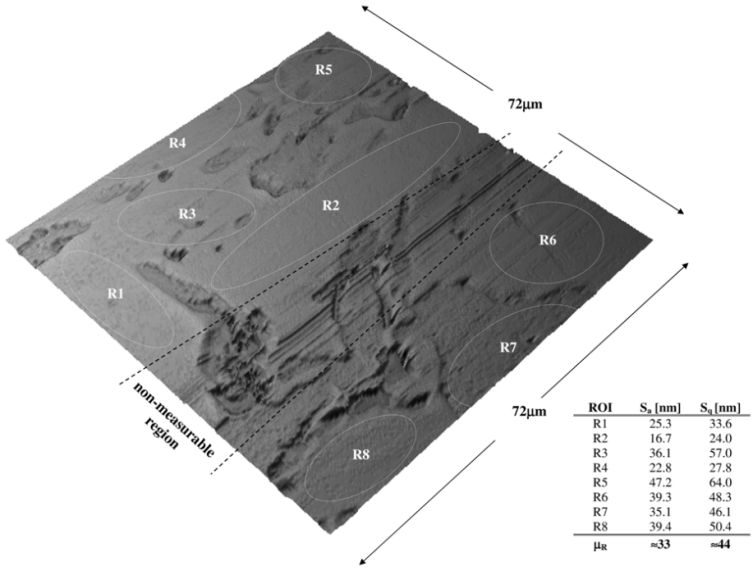

ROI	S_a [nm]	S_q [nm]
R1	25.3	33.6
R2	16.7	24.0
R3	36.1	57.0
R4	22.8	27.8
R5	47.2	64.0
R6	39.3	48.3
R7	35.1	46.1
R8	39.4	50.4
μ_R	≈33	≈44

Figure V.2 Isometric view (MountainsMap®) of the surface topography obtained with the aid of the AFM microscope, after leveling and subtraction of waviness component (8 [µm]). Please note that the obtained topographic images include scanning artifacts, and therefore the most affected region has been excluded from the roughness analysis. The surface scan was made after the polishing process.

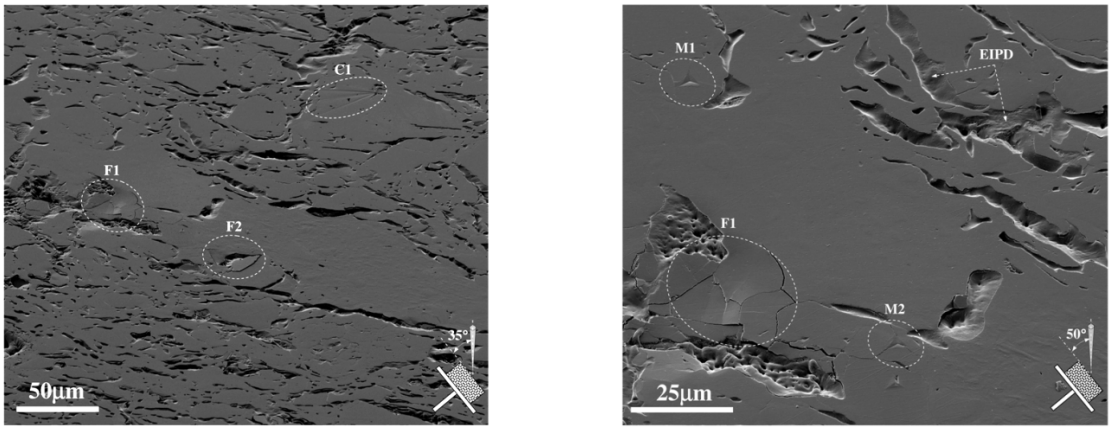

(a) (b)

Figure V.3 General view on the surface and its topography observed from different perspectives under the SEM microscope: a) surface tilt 35 [deg], b) surface tilt 50 [deg]. Apparent zones of local collapse of microstructure F1 and F2 of unidentified origin, ‘comet tails’ C1 or single empty pores, epoxy impregnated porous domain (EIPD) with relief, global indentation markings M1 and M2. The micrographs were taken 15 months after the experimental analysis and the sample was stored in a closed plastic container under normal room conditions.

V.3. EXPERIMENTAL PROCEDURE

The depth-sensing experiments were carried out with the CSM nanoindenter tester, provided with a vibration isolating system and constant temperature and humidity enclosure. Prior to running the indentation schedule, the depth-area function of Berkovich diamond indenter had been calibrated on the polished standard fused silica sample E=72 [GPa], ν=0.17, certified and provided by the instrument manufacturer. The automatic calibration schedule covering load range from 0.1 [mN] up to 100 [mN], with five measurements at each of 22 load steps, has been applied. The compliance of the indenter load frame is fixed with C_f=0.1 [μm/N]. The polished brick sample had been fixed with cyanoacrylate glue to the metal base, cleaned using cotton-wool moistened with isopropanol, and, finally, firmly mounted into the sample holder of the instrument.

Single indentation grid covers a region on the surface of the sample as small as $L_x \times L_y$=30×30 [μm], if one specific single target is in focus (e.g. pockets of 'glassy' matrix or quartz), but also much larger areas L_x,L_y>100 [μm], which include the mixture of the existing phases. Therefore, the optical microscope provided with the nanoindentation tester has been extensively used for an accurate target location and visual pre- and post-inspection of the probed area. Within each rectangular matrix, the inner spacing of the grid points along X and Y axes are equal l_x=l_y. The separation distance is chosen according to the size of the indentation imprint l (see Figure V.4(a)) for the load protocol specified in the scheduled matrix. This is obtained on a control run on the 'glassy' matrix phase, taken in the close proximity of the matrix origin. Hence, for a given maximum load P_{max} the size of the indentation imprint with Berkovich tip equals l=$6.52h_c \approx 7h_c$, where h_c=h_{max}-$\varepsilon P_{max}/S$ is a depth of contact evaluated from the control depth-force diagram (see Figure V.4(b)), h_{max} is the maximum depth, S is the tangent of the control depth-load diagram at maximum load and ε is a constant that depends on the geometry of the indenter.[5]

In order to avoid overlapping of the two adjacent indentation imprints produced on the 'glassy' matrix and phases with comparable or higher hardness, e.g. quartz, hematite or feldspar, the minimum spacing $l_x \geq 2l = 14h_c$ has been adopted. Since the porosity domain is filled with the hardened epoxy resin, which is known to be a much softer material, a significant overlap of the indents on this sub-domain is expected to take place. So the formulated criterion, together with the investigated spot size, governs the number of the grid points N_{tot}=$N_x \times N_y$, with minimum value set to ≈100.

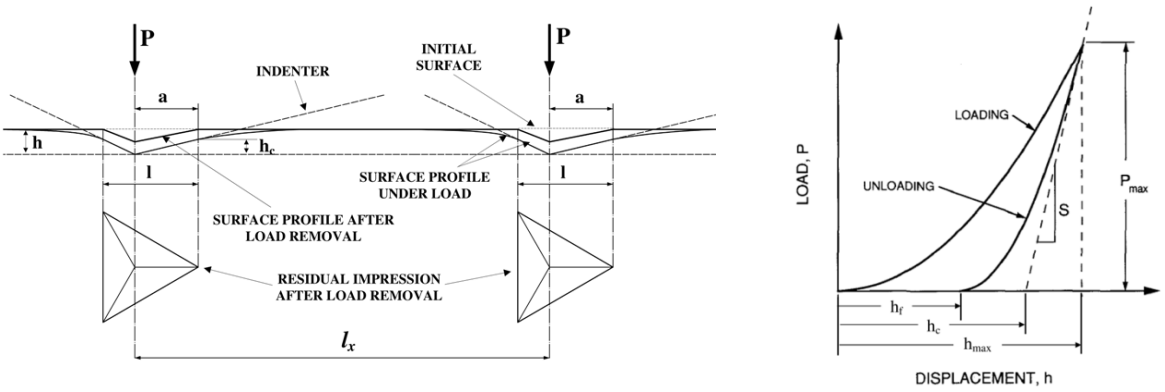

(a) (b)

Figure V.4 A schematic representation of the indentation grid segment and load-displacement relation with various quantities used in the analysis: a) a section through a sequence of indentation imprints with top view on the indented surface, b) a typical indentation curve with graphical definition of plastic h_f, contact h_c and maximum depth h_{max} after.[5]

At each point of the single grid, the depth-sensing measurement has been executed following the same protocol: loading with a constant rate 5 [mN/min] up to a maximum force, dwell time t_d=5 [s] at maximum load and unloading with a constant rate 5 [mN/min]. The speed of the tip approach to the surface has been fixed to a value 2 [μm/min]. Four different load regimes have been investigated P_{max}={1.125; 2.25; 4.5; 9.0} [mN]. An holding period at $0.1P_{max}$ for the thermal drift correction was not applied.

The resultant indentation load-displacement data are analyzed according to the method proposed by Oliver and Pharr,[5] which provides the indentation modulus M for general anisotropic materials, see Eq. V.1[24] as well as the indentation hardness $H=P_{max}/A$, where M_r is the reduced (effective) elastic modulus calculated from the unloading stiffness S and the projected area of contact A at peak load (Figure V.4(b)).

$$\frac{1}{M}=\frac{1}{M_r}-\left(\frac{1-\nu^2}{E}\right)_{indenter} \qquad \text{V.1}$$

The indentation modulus and hardening are determined at each *i-th* grid point of the indentation matrix. Therefore, in statistical sense they may be considered as an experimental set $\boldsymbol{x}_i=[H_i, M_i]$ for $i=1\ldots N_{tot}$ of the random variable $\boldsymbol{X}$, which obeys the statistical law of mixtures (Eq. V.2):

$$f(\mathbf{x};\boldsymbol{\psi}) = \sum_{j=1}^{g} \pi_j f_j(\mathbf{x};\boldsymbol{\varphi}_j), \quad \sum_{j=1}^{g} \pi_j = 1, \quad \pi_j \geq 0 \qquad \text{V.2}$$

In this work, the corresponding distribution functions $f_j=f_j(\boldsymbol{x};\boldsymbol{\varphi}_j)$ are assumed to take the form of bivariate normal distributions with weights π_i. Vector $\boldsymbol{\varphi}$ consists of the elements of the mean phase properties $\boldsymbol{\mu}_j$ and the distinct elements of the corresponding covariance matrices $\boldsymbol{\Sigma}_j$. Hence, Eq. V.2 represents the Gaussian Mixture Model (GMM)[6] with unknown parameters $\boldsymbol{\psi}=[\pi_j,\ldots,\pi_g,\boldsymbol{\varphi}_j,\ldots,\boldsymbol{\varphi}_g]$, which are assessed with the Maximum Likelihood (ML) based estimation via the Expectation and Maximization (EM) algorithm. The assessment of phase properties, the dispersion of experimental data and their correlation, as well as the data clustering have been achieved with the help of the code EMMIX.[25]

Finally, the post-indentation screening of the investigated regions has been done in the general purpose Scanning Electron Microscope (SEM) JEOL 5910, equipped with Bruker Energy-Dispersive X-ray (EDX) spectroscopy of elemental analysis and mapping.

V.4. EXPERIMENTAL RESULTS

This paragraph presents the experimental results in the following order: first, the phase properties obtained at the local level of particular single grids are introduced; next, the results of global (averaging) analysis are considered; finally, the estimation of the descriptors of the surface topography like mean S_a and squared-mean roughness S_q, obtained in the depth-sensing experiment, are reported.

V.4.1. Local Analysis-Single Matrix Results

For this particular experimental run the macro-pocket of the ‘glassy’ matrix phase was localized on the surface of the sample and chosen for the assessment of the mechanical phase properties by means of nanoindentation (see Figure V.5(a-b)). As may be seen from the BSEM micrograph (Figure V.5(c)), the ‘macro-pocket’ of matrix occupies a significant region on the surface, with characteristic dimensions assessed by the means of Feret’s maximum F_{max} and minimum F_{min} statistical diameters equal to ≈800 [μm] and ≈150 [μm], respectively. Due to the large size, the depth-sensing indentations could be carried out on several grids under different maximum force regimes. Moreover, the effect of mixing with other microstructural features, like aggregates of different origins or porosity, is significantly reduced in comparison with the grid measurements carried out in the ‘non-localized’ fashion.

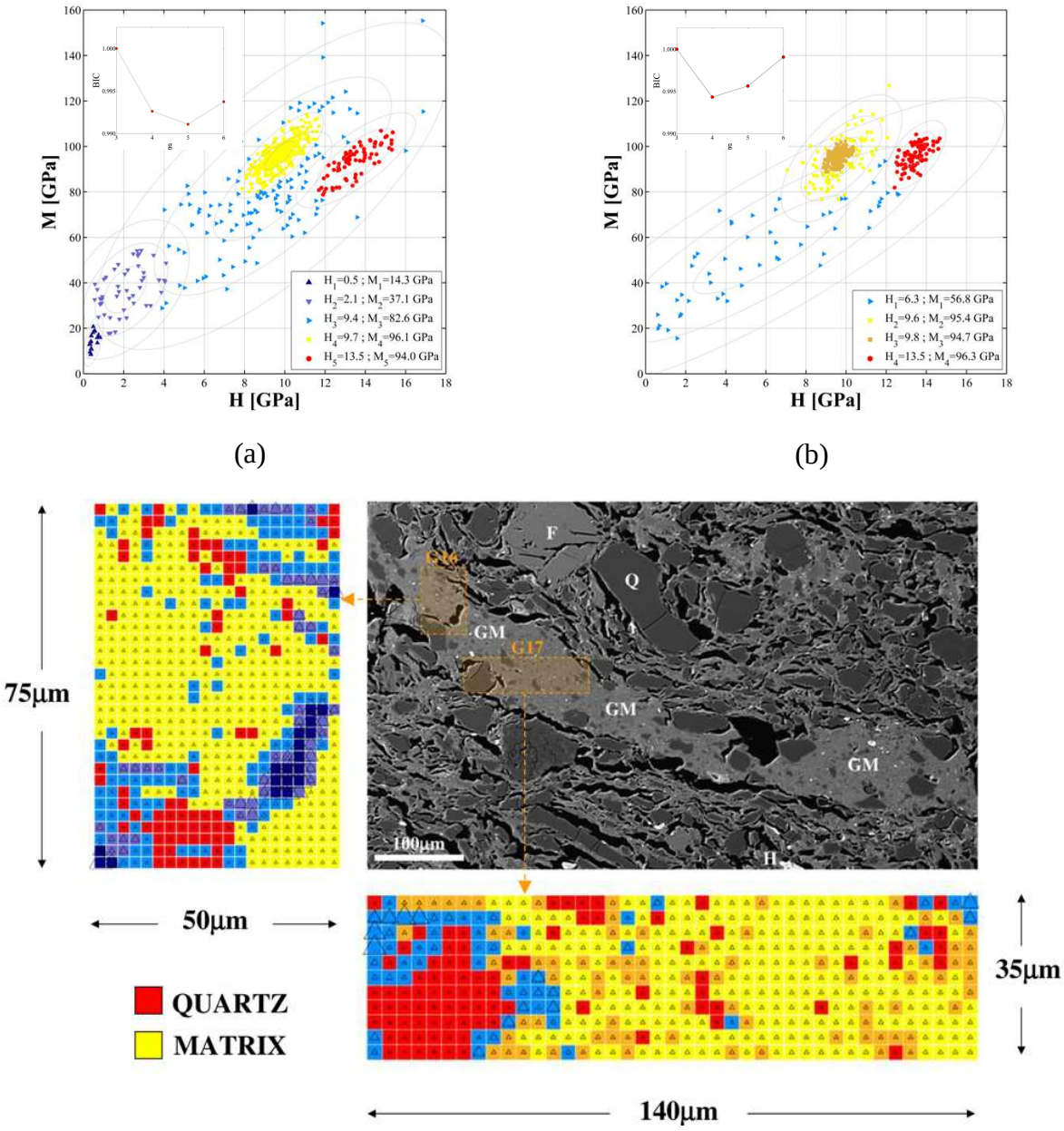

Figure V.5 Results of the grid indentation analysis carried out on the large pocket of 'glassy' matrix. Scatter diagrams of the experimental records in bivariate space *H-M*: a) Grid G16, P_{max}=2.5 [mN], l_x=l_y=2.5 [µm], N_x×N_y=21×31, b) Grid G17, P_{max}=4.5 [mN], l_x=l_y=3.5 [µm], N_x×N_y=41×11, c) global view on the investigated region of material obtained in BSEM mode, visible macro pocket of 'glassy' matrix, grains of *k*-feldspar (F), quartz (Q) and hematite (H), with probabilistic reproductions of indented domain based on the clustering of experimental records for grids G16 and G17. Estimation procedure and clustering carried with the aid of code EMMIX.[25]

The results from two experimental grids are selected for further details. The first grid (G16 on Figure V.5(c)) covers the region on a surface 50×75 [μm] with internal grid spacing equal to 2.5 [μm], giving around 650 measurement points in total. The indentations are driven up to a maximum force P_{max}=2.5 [mN]. The corresponding outcome is presented in the form of the scatter diagrams in the bivariate space *H-M* (Figure V.5(a)). Looking at this diagram, the experimental records concentrate mostly into two main sets of points, overlaid with the group of measurements scattered over a significantly larger domain of *H* and *M*. The Bayesian Information Criterion (BIC) is minimized for *g*=5 normal components. Therefore, this penalty criterion recognizes the two main sets (phase 4 and 5), but the third group described with significant dispersion has been discretized into three separate families (phases 1, 2 and 3). The 'glassy' matrix phase, which is the focus of present research, appears to be described by the cluster of the points with the mean properties: hardness H_4=9.7 [GPa] and indentation modulus M_4=96.1 [GPa] (yellow cluster, Figure V.5(a)). Its hardness seems considerably lower than the hardness of the quartz aggregate (red cluster), with H_5=13.5 [GPa], but the indentation modulus seems to be comparable, with M_5=94.0 [GPa]. The remaining phases correspond to the indentations carried on hardened epoxy within the porous domain or in close proximity to incorporated voids. This group of records includes also abnormal measurements, which are ill conditioned in nature due to fracture or different type of anomalies, e.g. soft-on-hard behavior.

The second grid spans over a surface 140×35 [μm] (G17 on Figure V.5(c)). This grid includes around 450 grid points separated by the distance of 3.5 [μm] with a maximum force applied almost doubled P_{max}=4.5 [mN]. Also in this case, two main groups of points may be easily depicted on the diagram. But on the contrary to the previous results, the number of the mixture components assessed with BIC penalty decreases by one. Moreover, an additional component has been introduced within the *H-M* domain of the 'glassy' matrix phase. The two clusters which correspond to the indentation on the 'glassy' matrix phase have mean values which are almost indistinguishable, hardness H_2=9.6 [GPa] and H_3=9.8 [GPa], and indentation moduli M_2=95.4 [GPa] and M_3=94.7 [GPa], respectively. However, as may be observed from the scatter diagram, the two sets of points have significantly different internal dispersion, with variances of properties being much larger in the set 3 than in set 2. The quartz properties obtained at higher load are H_4=13.5 [GPa] and indentation modulus M_4=96.3 [GPa]. The homogeneity of the quartz cluster appears to be considerably improved comparing with the results for lower peak load.

Finally, to enhance the spatial correlation of the grid measurements with the surface topography captured with BSEM micrograph, the probabilistic map of the indented surface based on the clustering results is presented for both grids (Figure V.5(c)). The center of each marker corresponds to the location of the depth-sensing measurement, while its color reflects the color scale assumed in the scatter diagrams located above. The outlines of the model indentation imprints produced on the surface are also shown.

V.4.2. Global Analysis – Results of Matrix Averaging

The grid indentation measurements were carried out in four different regimes of the indentation load P_{max}. For each regime of the load applied, the GMM deconvolution was executed in order to indentify the mechanically and statistically active material phases. Therefore, the results of the GMM deconvolution, as shown for G16 and G17 above, at local level of the grid analysis demonstrate the existence of the two principal clusters. These clusters have been associated to the 'glassy' matrix phase $H \in [8;12]$ [GPa], $M \in [80;120]$ [GPa] and mineral quartz with approximate bounds $H^Q \in [12;16]$ [GPa], $M^Q \in [80;120]$ [GPa]. They have been identified in each of the carried grid measurements, independently of the indentation load as well as the grid target, e.g. localized or non-localized analysis.

The Global Analysis and its results introduced at this point correspond to the mechanical phase properties, which represent the average of the results obtained in the Local Analysis at each indentation load. It has been assumed that the mechanical properties of the 'glassy' matrix, as well as quartz, are distributed normally at the global level, with population mean $\mu_{H,M}$ and variance $\sigma_{H,M}^2$. Therefore, each cluster identified in the grid measurements and corresponding to the mentioned mechanical phases, has been considered as a subsample derived from the related population and distributed around the related sample mean with the appropriate sample variance. As a result, the average of the obtained sample means approaches the population mean and may be used as an estimator of the mean phase properties at the global scale. The outcomes of the averaging process, as well as the corresponding confidence intervals and additional statistical measures, e.g. Pearson's coefficient, are included in Table V.1 for the 'glassy' matrix and Table V.2(a-b) for the quartz phase.

Table V.1 Mechanical properties of the 'glassy' matrix' obtained in the depth-sensing indentation in multiple grid indentation measurements.[1]

P_{max} [mN]	1.17±0.01	2.28±0.01	4.54±0.01	9.03±0.04
h_{max} [nm]	97.47±3.36	140.45±4.17	206.98±9.96	293.13±0.78
H [GPa]*	9.54±0.40	9.60±0.33	9.17±0.81	9.92±0.46
M [GPa]*	100.09±7.36	95.34±5.41	89.92±8.20	90.55±5.45†
φ**	-3.73±0.73	-3.46±0.87	-3.48±1.82	-3.20±0.83
r***	0.63±0.18	0.72±0.09	0.67±0.16	0.67±0.06

1- properties extracted from the GMM deconvolution of multiple matrix measurements, * - mean values with limits representing the 95% confidence intervals of the mean, ** - angle of inclination of the equal probability density ellipses $tan(2\varphi)=2cov(H_{IT},M)/((\sigma_{HIT})^2-(\sigma_M)^2)$, counterclockwise, degrees of arc °, *** -the linear (Pearson) correlation coefficient $r_{Hit,M}=cov(H_{IT},M)/(\sigma_{Hit}\sigma_M)$, † - one standard deviation

As can be seen from Table V.1 and its pictorial representation (Figure V.6(a)), the average indentation hardness H of the 'glassy' matrix may be considered stable over the range of the load applied, taking into account the span of the confidence intervals. This trend may not hold for the indentation modulus M because of the apparent steady rise of this property with decreasing indentation force. On the other hand, as the maximum indentation force increases, the convergence of this property towards an asymptote ≈90 [GPa] takes place (see Figure V.6(a)). Both measured properties are strongly correlated, reflected by a quite significant value of linear (Pearson) correlation coefficient r, which appears to be relatively stable for the considered loads. Finally, the equal probability inclination angle φ and $r > 0$ show that this correlation is positive independently on the force applied, meaning that any increase in the indentation hardness of matrix phase H leads to an increase in the modulus M.

The average indentation hardness of the second identified mechanical phase (statistical cluster II), corresponding to the quartz mineral, is much higher in comparison to the hardness of the matrix phase $min(H^{II})\approx 1.4 min(H^{I})$. Also in this case, H does not suffer from drastic changes in value, with respect to the level of the load applied in the experimental analysis (Table V.2(a)). However, Figure V.6(b), and previously referred table, shows a slight increase over the remaining means of hardness for the indentation load ≈11 [mN]. A similar tendency has been noticed in indentation experiments on single, isolated aggregate of quartz, whose results representing the average from a minimum of 10 measurements at each load level are included in Table V.2(b). Regarding the average indentation modulus M, this property seems to be hardly influenced by the load level (penetration depth) based on the grid measurements

results. A less prominent convergence toward an asymptote located at $M \approx 95$ [GPa] when compared to the 'glassy' matrix phase is observed.

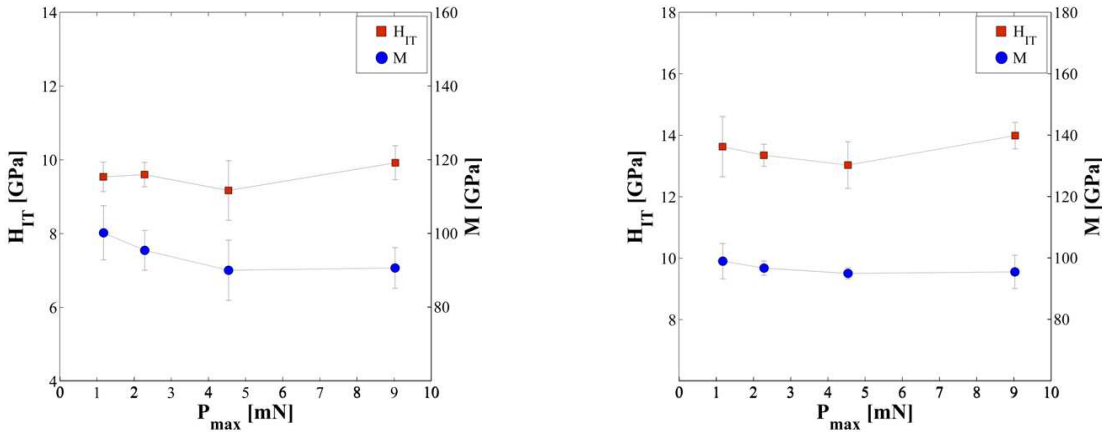

(a) (b)

Figure V.6 Results of the global analysis, variation of the indentation hardness *H* and modulus *M* with respect to the maximum indentation load P_{max} applied: a) *Phase 1* is associated to 'glassy' matrix (Table V.1), b) *Phase 2* is assumed to represent the quartz (Table V.2(a-b)). Note that the grey lines are visual aids and do not imply any trends.

The average values of the indentation modulus obtained in grid analysis (Table V.2(a)) compare well with the outcomes from the single aggregate measurements (Table V.2(b)), but an increase in the modulus for the lower loads appears to occur in the latter case. According to the discussed results, both measured properties are positively correlated for most of the ranges of indentation load or penetration depth equivalently.

Table V.2(a). Mechanical properties of quartz obtained in the depth-sensing indentation in multiple grid indentation measurements.[1]

P_{max} [mN]	1.17±0.01	2.28±0.01	4.54±0.01	9.03±0.04
h_{max} [nm]	90.24±3.39	127.75±1.43	185.66±3.31	264.18±0.89
H [GPa]*	13.63±0.98	13.35±0.36	13.03±0.76	13.99±0.43
M [GPa]*	98.89±5.76	96.61±2.35	94.89±1.82	95.39±5.42†
φ**	-6.97±6.01	-5.27±1.32	-2.73±1.90	-3.22±2.14
r***	0.66±0.37	0.67±0.20	0.54±0.34	0.70±0.08

1- properties extracted from the GMM deconvolution of multiple matrix measurements, * - mean values with limits representing the 95% confidence intervals of the mean, ** - angle of inclination of the equal probability density ellipses $tan(2\varphi)=2cov(H_{IT},M)/((\sigma_{HIT})^2-(\sigma_M)^2)$, counterclockwise, degrees of arc °, *** - the linear (Pearson) correlation coefficient $r_{Hit,M}=cov(H_{IT},M)/(\sigma_{Hit}\sigma_M)$, † - one standard deviation

Table V.2(b). Mechanical properties of quartz[2] obtained in the depth-sensing indentation on single aggregate.

P_{max} [mN]	1.16±0.01	2.29±0.01	5.53±0.01	11.05±0.02
h_{max} [nm]	88.95±1.02	126.71±2.17	208.29±6.27	296.85±2.97
H_{it} [GPa]*	13.70±0.28	13.23±0.54	13.28±0.57	13.86±0.32
M [GPa]*	102.31±2.15	99.88±2.72	91.82±6.71	93.43±1.95
r***	0.23	0.89	0.59	0.40

2- properties measured on the isolated, single aggregate of quartz, $\tau_l=\tau_{ul}=2.5$ [mN/min], * - mean value, from minimum 10 measurements, with limits representing the 95% confidence intervals of the mean.

In the closure of this section additional findings revealed in the statistical gird indentation experimental analysis are briefly reported. In the experimental campaign the main target has been set on the assessment of the mechanical properties of the 'glassy' bond incorporated within the brick microstructure. However, next to the mechanical identification of the mentioned phase, the experimental analysis revealed the presence of other components with distinct mechanical properties and incorporated in significantly lower volume fractions. One of such species is titanium-oxide bearing solid, whose chemical composition has been confirmed in the EDX analysis. This phase is provided with a radically higher stiffness than the host matrix or even quartz, with a mean value about $M\approx240$ [GPa]. On the other hand, its hardness $H\approx14.50$ [GPa] is still significantly higher than the indentation hardness of 'glassy' matrix, but appears to be comparable to the hardness of quartz. The reported values were obtained at the penetration depth $h_{max}\approx73$ [nm]. Such solid may be associated with rutile mineral, which is common in the ceramic batches as well as structural building products.

V.4.3. Surface Topography – a First Order Approximation Toward Areal Parameter Characterization of Investigated Regions via the Point of Contact Detection Procedure

A single depth-sensing experiment protocol, carried out in the standard way, incorporates three basic stages (see Figure V.7(a)): approaching the surface with the indenter head, the proper indentation according to a chosen loading-unloading schedule and finally retracting the probe to its neutral position z_0. The second step, leading to the principal load-penetration depth *(P-h)* curve, is initialized once the contact between the probe and the sample surface, marked as 'point of initial contact' z_c, has been achieved. This point represents the position of the indenter that is the 'zero' reference for the depth-measurement.[26,27] Such a sequence is

repeated at each *i-th* nodal point of the indentation grid programmed over a chosen region of interest (ROI) on the specimen surface. From the figure it may be observed that, if the neutral position of the tip marked as z_0 is assumed to represent the auxiliary reference plane $z(x,y)=z_0$, hence the distance measure $\Delta_i=z_{c,i}-z_0$ gives access to the ROI topography at each discrete location. Therefore, an approximate map of the surface texture, with accuracy (resolution) limited mostly by the grid spacing l_x and l_y may be reconstructed, as well as a first order estimation of the areal parameters could be obtained.

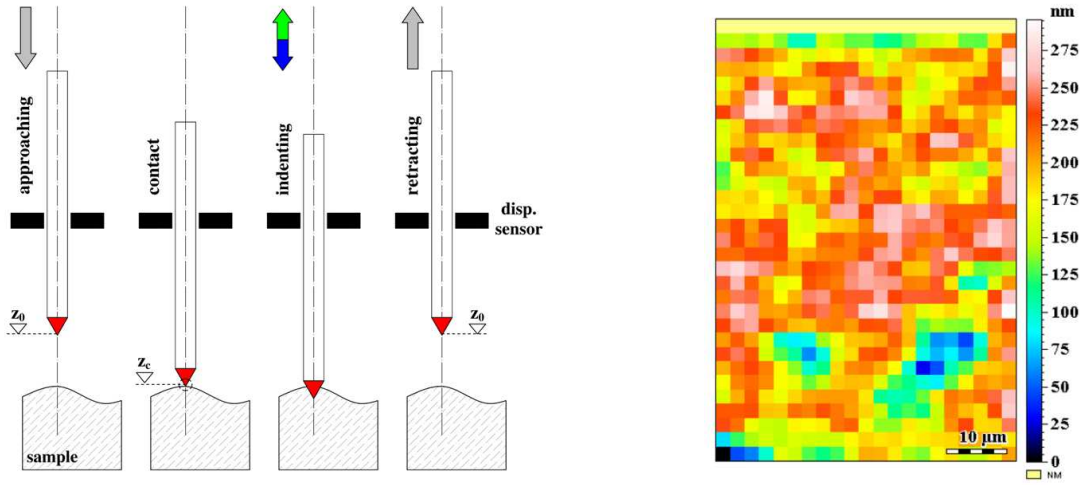

(a) (b)

Figure V.7 Aspects regarding the single indentation experiment: a) a schematic representation of the flow sequence, b) reconstruction of the specimen surface based on the 'point of contact' procedure, roughness component of the surface obtained with MountainsMap®[28] after leveling and filtering the waviness (8 [µm]) component from the raw data. NM – non-measurable points.

An attempt to estimate the areal parameter of grid G16 (see Figure V.5(c)) based on the points of contact approximation is presented next (Figure V.7(b)). The corresponding measures of the surface roughness S_a and S_q are calculated according to the ISO standard,[23] giving in this particular case the approximate values of ≈36 [nm] and ≈46 [nm], respectively. This means that the obtained values compare well with the average values measured with the Atomic Force Microscope (AFM).

V.5. DISCUSSION

V.5.1. Glassy Bond – the Origin of Its Elastic Properties and Hardness, and a Comparison with Existing Data for Glass and Glass-Ceramics

In the opening of this discussion the morphology together with composition of the 'glassy' bond must be recalled. This load bearing component of the brick microstructure is a composite material, where the neo-formed crystals, e.g. spinel, mullite of sub-micrometer size coexist with aluminosilicate glass (see Figures V.1(a-d) and V.8(c)). This structure reminds that of glass-ceramics, in which randomly oriented crystals are bound by residual glass to form a solid free of voids. However, while in the glass-ceramic the typical mass fraction of glass does not exceed 5 [wt%],[29] this is not the case for the building ceramics. In this group of materials, the mass fraction of the incorporated amorphous phase tends to span from around 10 % at 900 [°C] to as much as 60 % of the total mass of solid for processing temperature around 1300 [°C].[30,31,32,33] On the other hand, in this temperature range the mass contribution of neo-crystal phases, like mullite, is substantially lower. The studies of quantitative determination of crystalline and amorphous phases reveal this contribution to be in the range [3;15] [wt%] for traditional ceramic products,[30,33] rarely exceeding 20 % of the total mass of the stoneware, like in the case of electric porcelain bodies produced at 1400 [°C].[34] Therefore, the fraction of the polycrystalline phase incorporated within the 'glassy' matrix is well below the one for glass-ceramics, what makes the aluminosilicate glass the principal component. Nevertheless, it may be instructive to trace the characteristic domains of the elastic properties and hardness of oxide glass-ceramics and glasses created on the base of a ceramic system, in which SiO_2-Al_2O_3 pair of oxides represents the principal chemical species. Such materials could be considered as representing a part of the 'fictitious' frontier for the domain of the measured properties of the 'glassy' matrix.

Two of the examples belonging to the first group of materials are the glass-ceramics investigated by Hunger et al.[35] or Wange et al.[36] (see Figure V.8(a)). Both studies are focused on the microstructure-property relation in the glass-ceramics in the system SiO_2-Al_2O_3-MgO-TiO_2, with possible use of nucleating agents like ZrO_2. According to these studies, the glass-ceramics microstructures, whose principal components are crystals of low-, high-quartz, next to minor contribution of *Mg-Al* spinel, sapphirine or cordierite in the size tens of nanometers (see Figure V.8(a)), are characterized by relatively high Young's modulus E (>100 [GPa]) and Vickers hardness HV (>8 [GPa]), the later obtained at load level P=2÷20 [N] (Figure V.9(a)). It may be also noted, that both measured properties of such

ceramic systems may reach up to ≈150 [GPa] for modulus of elasticity and as much as ≈12.5 [GPa] for hardness.

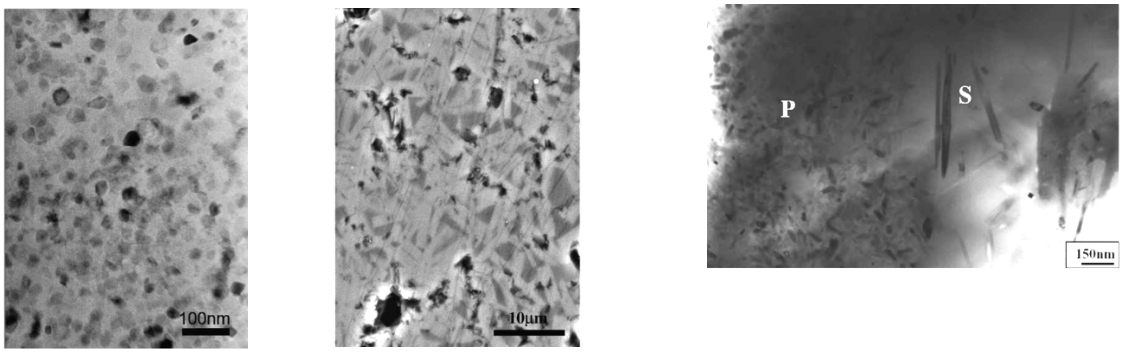

(a) (b) (c)

Figure V.8 Examples of glass-ceramic microstructures: a) TEM micrograph of glass-ceramics investigated by Hunger et al.,[35] b) SEM micrograph of the feldspar glass-ceramics studied by Bernardo et al.,[37] c) Bright-field TEM of 'glassy' matrix with primary (P) on left side and secondary (S) mullites on the right side in model porcelain sample quenched after 3 [h] at 1100 [°C], adopted from Iqbal and Lee.[17]

Similar Vickers hardness ≈8 [GPa], measured at P=5 [N], may be also encountered in the porous (φ<5 %) feldspar glass-ceramics investigated by Bernardo et al..[37] In this material the main phase constituents are feldspars (microcline and orthoclase), which account for almost 80 % of the total volume and are of fibrous morphology with average crystal size of [4;5] [μm] (see Figure V.8(b)). However, despite the incorporation of the alumina platelets in the volume fraction up to 15 %, its Young's modulus in the range [60;80] [GPa] is significantly lower than the one from quartz-based glass-ceramics previously discussed (Figure V.9(a)).

The domain of Young's modulus and hardness of inorganic glasses shifts drastically towards smaller values on the *HV-E* 'fictitious roadmap' (Figure V.9(a)). The results of Hand and Tadjiev,[38] Yoshida et al.[39] or Pukh et al.,[40] obtained on silicate glasses, indicate a common range for the Young's modulus [60;80] [GPa]. Similar range of values was given by Rouxel for soda-lime-silicates.[41] As for the Vickers hardness, it tends to be inscribed within [4;6] [GPa]. All referred studies confirm an appreciable variation of mechanical properties with respect to the glass chemistry (Figure V.9(a-b)), as observed in the earlier investigations of Ainsworth[42,43] or Yamane and Mackenzie on silicate glasses.[44,45] It is generally accepted, that the main reason for this is the variation of the bonding energy of atoms and their packing density with glass composition. Therefore, the elastic behavior of glass and its strength

depend on the nature of the oxygen polyhedra (network former), the way on which the polyhedra are linked together and the nature of any network-modifiers present.[42,43]

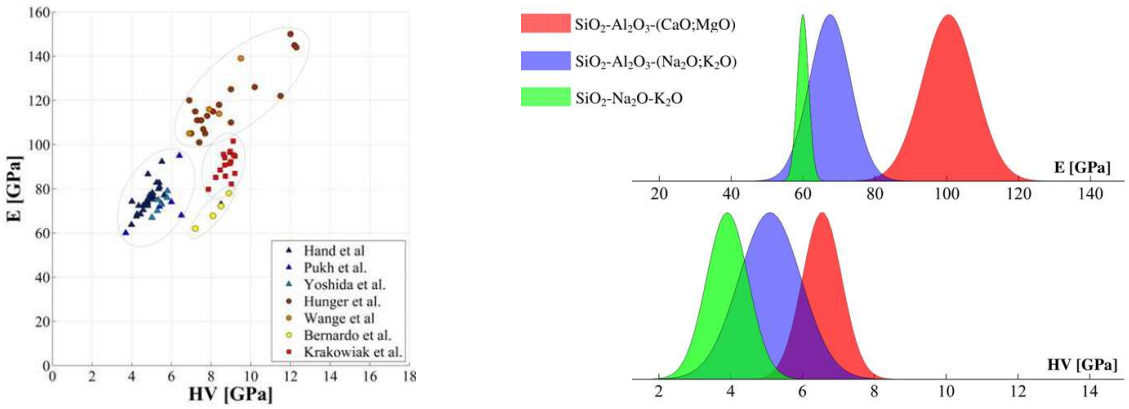

(a) (b)

Figure V.9 Mechanical properties of selected ceramic materials: a) scatter diagram of HV-E for inorganic glasses and selected glass-ceramics, b) modulus of elasticity (*E*) and Vickers hardness (*HV*) of silicate and aluminosilicate glasses, data extracted from the SciGlass data base for glass properties.[46]

With the model results of glass-ceramics and silicate glasses discussed above, an attempt to classify and understand the origin of the experimentally measured indentation properties of 'glassy' matrix phase is made next. In order to reach this goal, the experimental indentation modulus *M* and indentation hardness *H* are used to calculate the corresponding modulus of elasticity $E=M(1-\nu^2)$ and Vickers hardness $HV\approx0.93H$ of matrix obtained in each single grid measurement. An assumption of the isotropic solid with Poisson ratio ν=0.24 is made, what seems to represent a reasonable compromise between the glass and glass-ceramic materials. The results of such conversion are overlaid together with reference data on the *HV-E* plane (Figure V.9(a)). It must be noted that no distinction for the force applied is made in this case, therefore the set of the experimental values is bound approximately within [8;10]×[80;100] [GPa] region on *HV-E* plane, with a tendency of the records to skew towards its upper limits.

One of the first observations drawn relates to the hardness of matrix, which appears to be quite similar to the reference hardness of quartz- and feldspar glass-ceramics, although significant differences exist in the mineralogical composition. Such a conclusion must be considered with care and may be premature, since the *HV* of 'glassy' matrix is not measured directly but inferred theoretically. Moreover, the load level applied in the experimental

analysis of the brick matrix is much smaller than the referred cases. While the magnitude of hardness tends to be comparable, a similar observation does not hold for the Young's modulus (Figure V.9(a)). The elastic modulus of 'glassy' matrix is substantially higher than the elastic modulus of silicate or aluminosilicate glasses with alkali oxides incorporated as well as feldspar ceramics. On the other hand, the elastic modulus is appreciably lower than in case of high strength glass-ceramics reported by Hunger et al.[35] or Wange et al..[36] Such result corroborates the composite nature of the 'glassy' phase (see Figure V.8(c)), meaning that the neo-formed crystal species, e.g. mullite, contribute to the overall stiffness of matrix and enhance this property, when compared with the 'pure' silicate or aluminosilicate glasses with alkaline elements (Figure V.9(b)).

Table V.3 Composition [wt%] and theoretical Young's modulus [GPa] of the glass incorporated within the microstructure of structural clay products.

Oxide	I*	II*	III*	IV**
SiO_2	60.16	67.88	59.50	76.00
Al_2O_3	24.11	22.86	26.86	16.00
Na_2O	3.21	1.81	3.84	---
K_2O	7.26	5.15	6.44	7.00
CaO	---	---	---	1.00
MgO	1.94	0.73	---	---
Fe_2O_3	3.32	1.58	2.45	---
TiO_2	---	---	1.07	---
E†	71.09	70.48	69.38	69.96(73.35)

*- quantitative electron microscopy (AEM) results reported by Navarro et al.,[14] **- reported by Iqbal and Lee,[17] † - values calculated according to method Priven-2000[46,47] as well as Makishima and Mackenzie[46,48] in brackets.

A quantitative image of the phenomenon just reported may be given by considering the volume c_m fraction of mullite estimated form the Voigt (upper bound, Eq. V.3(a)) and Reuss (lower bound Eq. V.3(b)) solutions for the effective stiffness E_{eff} of a composite material:

$$c_m^V = \frac{E_{eff} - E_g}{E_M - E_g} \qquad \text{V.3(a)}$$

$$c_m^R = \frac{(E_g - E_{eff})}{(E_g - E_m)} \frac{E_m}{E_{eff}} \qquad \text{V.3(b)}$$

where E_g and E_m are the theoretical moduli of the amorphous bearing phase and mullite crystal, respectively. The theoretical Young's modulus of the glass, calculated on basis of the experimentally determined composition (Table V.3), approaches $E_g \approx 71$ [GPa]. The modulus of mullite, corresponding to the average of the Voigt and Reuss model,[16,49] is around $E_m \approx 224$ [GPa]. Given these values, together with the mean of experimental records ≈91 [GPa] treated as a effective response, the expected volume fraction of the mullite phase is inscribed within the range [0.13;0.32] (see Figure V.10). As may be observed from the same diagram, the experimental band may shift and scale this interval significantly towards lower values (lower edge), or allow for appreciably higher volume of neo-crystals in order to reach experimental stiffness (upper edge). Nevertheless, such limits for c_m appear to be very consistent with the values determined experimentally. The Rietveld analysis on the structural clay products reveals the range of mullite volume fraction to be [0.05;0.16],[30,33] while the semi-quantitative analysis of heat-treated mixtures of mica, kaolinite and quartz in the temperature range 1100÷1300 [°C] gives the approximate bounds [0.18;0.33].[11]

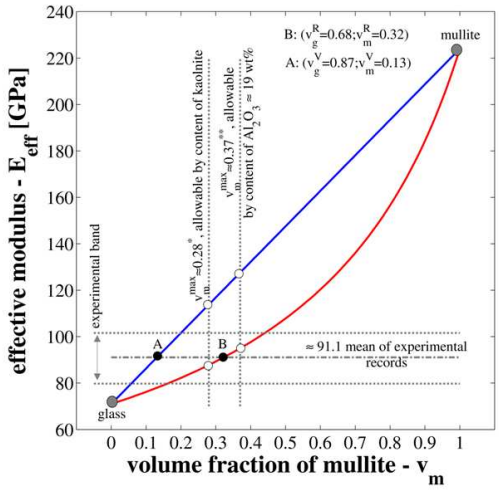

Figure V.10 Variation of the Voigt (upper) and Reuss (lower) bounds of effective modulus with respect to the mullite volume fraction within the 'glassy' matrix.

Finally, it is worth mentioning that the theoretical bounds for c_m, computed from the Voigt and Reuss solutions, are much lower than the maximum volume fraction of the mullite phase within the matrix $c^{max}{}_m$, which could be reached if the total amount ≈19 [wt%] of Al_2O_3 available in the batch was attributed to this phase only. This value has been estimated from the assumption of quartz content of 40 [wt%], which represents a very extreme case. In the typical commercial stoneware, the quartz content varies between 20 to 25 [wt%] only.[17,33]

Additionally, assuming that all the kaolinite contained in the raw batch ≈36 [wt%], obtained in the semi-quantitative FRX-XRD analysis, transforms to mullite on heating, the volume fraction of mullite approaches 0.28, which is within the Reuss-Voigt theoretical range. These observations additionally support the experimental finding reported in this work.

V.5.2. Phase Properties – Correlation With the Local Chemical Composition Obtained in the X-Ray Energy Dispersive Spectroscopy (EDX) Analysis

One of the most characteristic features of structural ceramics is the level of heterogeneity of its microstructure. Such heterogeneity, present across the material scales of a brick,[7,14,17,19] manifests not only by the complex 3D form of the brick skeleton, but also by the spatial variation of the mineralogical and chemical composition. The energy dispersive x-ray spectrometry (XRD) analysis exposes this phenomenon by mapping the distribution of the elements over the investigated surface of the tested brick (see Figure V.11(a-d)). This variation is apparent in the distribution of the coarse and fine grained quartz mineral or feldspar (see Figure V.1 and Figure V.5(c)), whose location within the skeleton tends to be random in nature. Therefore, with increasing size of the randomly selected region of interest (ROI) to carry out the depth-sensing grid measurements, the chances of probing phases of different mineral origins within a single matrix are increasing. As a result, the experimental outcome, seen for example as a scatter diagram of the records in *H-M* plane, may represent the complex pattern, whose statistical interpretation (deconvolution) could be complex leading to misclassification of estimated phase properties. Such effect may be easily amplified if a very low quality polished surface is examined or the contrast between the mechanical properties of the existing phases is weak. However, the careful surface preparation procedure and fine surface finish, together with appreciable mechanical contrast between the phases, provided a clear phase separation obtained in the statistical deconvolution (Figure V.5(a-b)), supported by the elemental maps taken on a larger scale over the same ROIs (Figure V.11(a-d)). Both grid measurements, G16 and G17, expose the cluster of the points associated with the quartz mineral, which may be easily located on the elemental maps as a region where the only element present is silicon (Si).

The appreciable variation of the chemical composition is encountered in the ‘glassy’ matrix phase as well and may be captured from the referred x-ray elemental maps. While the gross distribution of silicon appears to be uniform within the matrix phase (see Figure V.11(a)), a significant variation in the aluminum concentration is observed (Figure V.11(b)). More explicitly, the large pocket of the melt where the grid measurements G16 and G17 were

located tends to have quite constant concentration of this element. The rest of the matrix domain outside of the central ‘pocket’, with the characteristic form of ‘strings’, experiences a high gradient in alumina concentration, depending on the spatial location. Such regions are identified by much higher intensity of the x-ray signal recorded in the EDX detector on the elemental Al map (Figure V.11(b)).

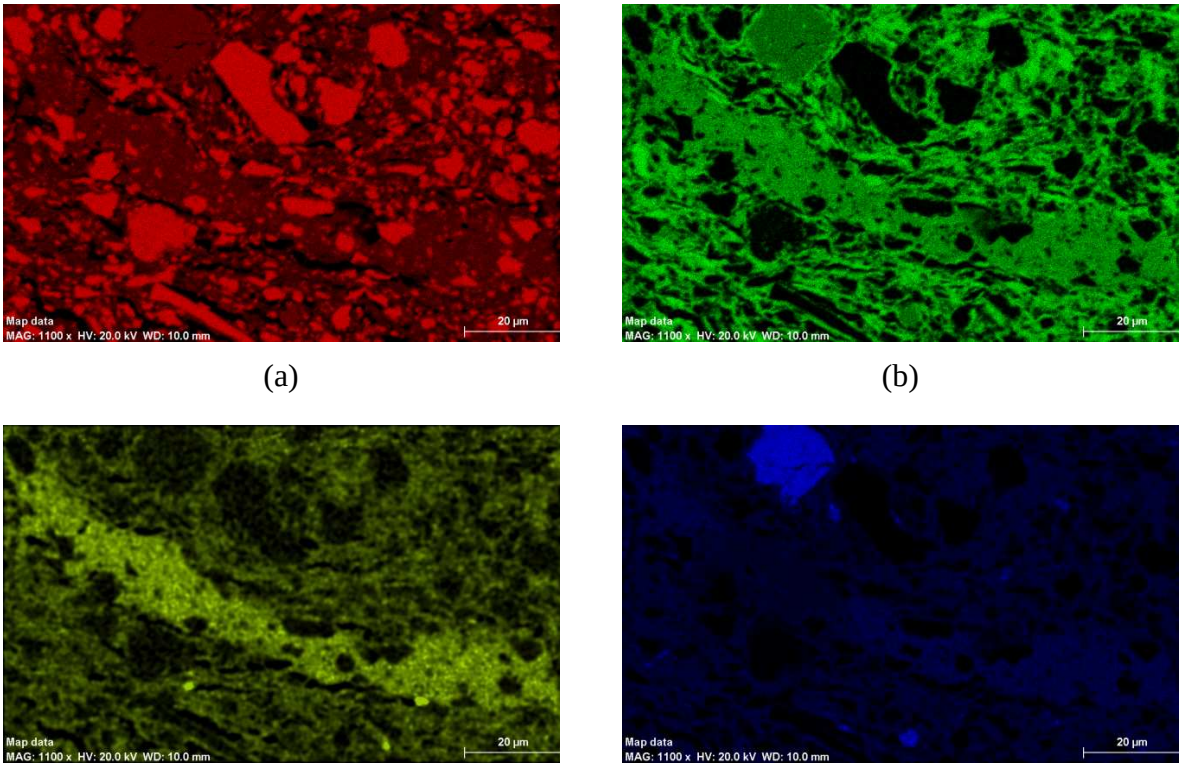

Figure V.11 Relative gross variations in the chemical composition over the region of interest (ROI) including the domain of the G16 and G17 matrices (see Figure V.5(a-c)). Mapping of spatial distribution of: a) silicon, b) aluminum, c) magnesium and d) potassium.

On the other side, the central melt pocket incorporates magnesium in higher amounts than the rest of the surrounding matrix phase. Finally, an apparent uneven distribution of alkalis, like potassium (see Figure V.11(d)), is present within the central melt ‘pocket’ itself. It may be observed, that the concentration of this element is lower in the region corresponding to the G17 grid experiment, when compared to the region of matrix G16 as well as the rest of the melt pocket. This difference in the contribution of the potassium to the overall composition of the melt could contribute to the slight difference in the average indentation modulus obtained on the two grids. Thus, the ‘glassy’ matrix region, where the higher concentration of potassium occurs (G17, M=94.7 [GPa]), gives average stiffness lower than the matrix phase

with less amount of alkali elements (G16 M=96.1 [GPa]). This observation is coherent with the behavior of inorganic glasses. The reduction of K_2O content by half in the melt composition I included in Table V.3, with simultaneous proportional increase of the other components to account for reduced mass, leads to theoretical Young's modulus E=73.11 [GPa]. Comparing this value with the original value of 71.09 [GPa] a minor 2 % increase has been found. Finally, such spatial variability in the chemical composition over the domain of matrix may significantly contribute to the overall scatter of the experimental results.

V.5.3. Phase Properties – Micromechanical Representativeness

In the testing of the mechanical properties of heterogeneous materials, the concept of mechanical representativeness of the measured properties is of primary importance. Therefore, it is required that the volume of the material considered to measure inherent material response should be representative – Representative Elementary Volume (REV). More specifically, to demonstrate the REV concept consider statistically homogenous composite material (satisfied condition of ergodicity)[50] of two solid phases firmly bonded together. According to Hill,[51] in such a case the REV term is used in reference to the sub-volume of the bulk composite material that "… (a) is structurally entirely typical of the whole mixture on average, and (b) contains a sufficient number of inclusions for the apparent overall moduli to be effectively independent of the surface values of traction and displacement, so long as these values are 'macroscopically uniform'.". Such a requirement must be obeyed not only at macro-level, e.g. direct uniaxial tension-compression tests, but also at the smaller scales (indentation tests), where the bulk material is confined in much limited volumes and one looks for the intrinsic properties of the phase. The postulate of Hill, in the framework of the classical homogenization (mean field) theory, aims at predicting the overall behavior of the heterogeneous medium at upper scale L_{macro} from its micro scale (denoted by d) constituents and is referred to as the *scale separability condition* (Eq. V.4):

$$\left.\begin{matrix} d < \\ d \ll \end{matrix}\right\} L_0 \ll L_{macro} \qquad \text{V.4}$$

where L_0 represents the characteristic scale associated with REV volume. As given, two options are allowed on the left side. The first inequality $d<L$ may be a sufficient condition for the phases with weak geometric disorder and weak properties mismatch, while in the other cases a much stronger restriction $d<<L$ must be fulfilled.[52]

The existence of the representative elementary volume and related scale parameter L_0 for the 'glassy' matrix composite is discussed next. Previous experimental investigations show the duality in the size of the neo-crystals incorporated within the 'glassy' matrix phase.[7,17,19] Such a duality is related to the two basic forms of the mullite phase, primary and secondary types, respectively. The primary mullite, together with accessory minerals like hematite, may reach up to ≈0.2 [μm] in size, while the secondary type is of acicular morphology with the approximate length ≈0.5 [μm] and aspect ratio a≈0.1÷0.25.[17] One may find mullite needles grown excessively above this size, however this occur only localized. The assembly of newly formed crystals and glass may be considered free of voids ($\varphi \approx 0$). Is such cases, the REV scale parameter $\delta_0=L_0/d$ depends on the relative mechanical contrast $E^{(i)}/E^{(m)}$ between the incorporated inclusions $E^{(i)}$ and the aluminosilicate glass $E^{(m)}$≈[60;80] [GPa]. The elastic constants of mullite measured with the aid of Resonant Ultrasound Spectroscopy (RUS) or Brillouin Spectroscopy are well documented $\boldsymbol{C}_{mullite}$={C_{11}≈280; C_{22}≈233; C_{33}=360} [GPa],[16,49] leading to the isotropic polycrystalline modulus $E^{(i)}$≈225 [GPa]. The elastic properties of hematite, as well as quartz, do not diverge significantly from the ones reported for mullite. Hence, $\boldsymbol{C}_{hematite}$={$C_{11}=C_{22}$≈242; C_{33}=228}[53] [GPa] and for quartz $\boldsymbol{C}_{quartz}$={$C_{11}=C_{22}$≈87; C_{33}=106}[54] [GPa] giving $E^{(i)}{}_{quartz}$≈99 [GPa] (Voigt/Reuss/Hill averaging). It is evident, that all the incorporated phases are relatively close to glass matrix in the sense of elasticity. Therefore, the 'glassy' matrix composite is characterized by the apparently small mismatch in the elastic properties $\alpha=E^{(i)}/E^{(m)}$≈3. As a result, the weak form of the scale separation condition (Eq. V.4) seems to apply.

According to the criterion proposed by Drugan & Willis (called here DW model)[55] for a two phase composite of randomly dispersed isotropic particles within an isotropic matrix, the minimum REV size for which the nonlocal term in the explicit equilibrium equations produces a no negligible correction to the local term, with 1 % error of the effective modulus, is $\delta_{DW}=l_N/2a$=3.5. This would be valid for the entire range of the volume fraction and is confirmed numerically by Gusev,[56] suggesting that the REV size is unexpectedly small, i.e. at least 3.5 times larger than the size of incorporated heterogeneity. This would entail $L^{DW}{}_0$≈0.7 [μm] for a primary mullite (PM) type morphology and $L^{DW}{}_0$≈1.7 [μm] for a secondary (SM) form. On the other hand, the numerical investigation[57] of two phase linear elastic composite, reinforced with the same inclusion type, indicates a REV parameter $\delta=L_0/d$>8. For a characteristic size of the material volume eight times larger than the incorporated heterogeneity, the discrepancy of the effective material properties obtained under

kinematic uniform boundary conditions (KUBC) and under static uniform boundary conditions (SUBC) is below 10 % for the phase contrast in the range [0.1;10]. Additionally, under both boundary conditions problems the coefficient of variation in the strain energy is below 5 %. Further increase in the REV size leads to the asymptotic convergence of the effective properties discrepancy towards zero. Hence, the results of numerical analysis suggest the REV size $L^{NUM}{}_0 \approx 1.6$ [μm] for primary mullite morphology and up to $L^{NUM}{}_0 \approx 4.0$ [μm] in case of secondary mullite morphology.

Summarizing the numerical estimation, and the theoretical bound given by the DW-model, the characteristic scale L_0 of REV element valid for 'glassy' matrix tends to be inscribed within the intervals $L^{PM}{}_0 \in [0.7;1.6]$ [μm] and $L^{SM}{}_0 \in [1.7;4.0]$ [μm], respectively. It should be emphasized at this point that the derived bounds assume the composite material reinforced by isotropic spherical inclusions. However, as mentioned in the text, as well as in the materials section of this chapter, the mullite phase (anisotropic behavior), and particularly its secondary morphology, is of acicular shape with quite significant aspect ratio. Therefore, the divergence of L_0 from the postulated limits above cannot be excluded.

The philosophy behind the standard indentation test is simple: by pushing the diamond probe of the indenter the volume of the bulk beneath becomes deformed in a way which reflects the mechanical properties of the tested solid. Therefore, the results of the inverse analysis of the experimental *P-h* diagram are considered to represent the average quantities from the volume (called here the interaction volume element IVE), which incorporates the fraction of the bulk excited from its natural state due to the mechanical interaction with the probe. It is generally assumed that a rough estimate of the interaction volume size is $3h_{max}$-$5h_{max}$ for Berkovich type indenter.[58,59] Appling this approximation to the indentation depths reached along the experimental campaign described in this work (Table V.1), one finds the interaction volume to be: [0.3;0.5] [μm] at P=1.17 [mN], [0.42;0.7] [μm] at P=2.25 [mN], [0.63;1.05] [μm] at P=4.5 [mN] and finally [0.9;1.5] [μm] at P=9.00 [mN], for 'glassy' matrix phase. Naturally, for a higher force applied, a proportional increase in the penetration depth (or equivalently interaction volume) is achieved. This means that the IVE is converging towards the theoretical estimate of the REV derived in the previous paragraph. In case of the very shallow indents at load level 1.17 [mN], the interaction volume size is two times smaller than the REV for primary mullite morphology and drastically smaller than the REV estimated for secondary mullite form. However, starting from the 2.25 [mN] indentation force, both elementary volumes start sharing common region and finally overlap for PM type morphology, whereas for the 9.0 [mN] load the interaction volume starts approaching the

lower bound of REV of secondary type morphology. Given this correspondence between both elementary volumes REV and IVE, it is very unlikely that the indentation experiment operated to a depth below 100 [nm] will infer the intrinsic properties of 'glassy' matrix phase. At this depth limit a measured composite response is highly influenced by the volume fractions ratio of glass and inclusions at the location of the grid point, leading to the high spatial variability in the measured properties. Such effect may demonstrates itself as a high scatter of the points in the experimental cloud plotted in H-M plane or as a cluster with much higher variance vector $[\sigma^2_H;\sigma^2_M]$ values.

V.6. CONCLUSIONS

The polycrystalline-amorphous matrix, called here the 'glassy' phase, represents a continuous composite solid, where the aluminosilicate glass hosts the neo-crystals of spinel, mullite and other accessory minerals in the size of tens of nanometers. Its complex geometrical form, a kind of three-dimensional 'scaffolds' with the sub-micron characteristic scale of its bulk, requires a novel experimental approach able to operate at nano-, micro-level and infer relevant mechanical characteristics. The multiple depth-sensing experiments combined with the advanced statistical methods, framed as statistical grid indentation technique (SGI method), was applied in this work providing unprecedented access to the hardness and stiffness of this principal brick microstructure component.

The indentation tests, operated to a maximum depth below 300 [nm], reveal the indentation hardness of the 'glassy' matrix around ≈9.5 [GPa] with relatively small fluctuations around this value with respect to the depth of indentation. In terms of the hardness level, this experimental value classifies the 'glassy' matrix above the family of silica and aluminosilicate glasses with alkaline additions, in the group of glass-ceramic materials next to the feldspar glass-ceramics, or even the high strength glass-ceramics based on low and high poliform of quartz.

The average indentation modulus of the 'glassy' matrix shows a small tendency to vary with the load, or equivalently the depth of indentation, converging toward an asymptotic value ≈91 [GPa] for testing depths above ≈150 [nm]. Below this threshold, the characteristic length scales of the indentation interaction volume and the representative elementary volume diverge significantly, entailing higher scatter of the experimental records.

The Young's modulus averaged over the experimental means, derived under the assumption of Poisson ratio 0.24, appears to be superior to the Young's moduli of inorganic glasses doped with alkaline elements. This enhanced stiffness finds its origin in the contribution of the neo-crystal phases to the overall elastic behavior of the 'glassy' bond. The particles and whiskers of mullite, of higher stiffness and strength than the host glass, reinforce the 'glassy' matrix and aid in the more homogeneous strain and stress redistribution over its volume. Therefore, the higher load can be sustained with the presence of smaller deformations, comparing to the pure glass.

Brick microstructure investigated in this work is of complex nature, with high level of the compositional heterogeneity and structural disorder. Such a phenomenon refers to the bulk of the brick, but also to the 'glassy' matrix itself, where the local variability in composition and morphology may be encountered. All these factors may contribute to overall dispersion of the experimental results measured by indentation technique. Moreover, this complex material system requires careful and pragmatic approach in the surface preparation for the indentation experiment, which is a challenge in the porous and multi-components solids like brick. The work reported here represents an attempt to describe the mechanical properties of the brick principal component, despite of difficulties mentioned above. It is believed, that the new insight into the mechanical performance of the 'glassy' matrix, as well as other findings reported in this work will help to change the brick into a more sustainable and energy-efficient construction material, tailored to our needs.

V.7. REFERENCES

[1]H. Reh, "Current classification of ceramic materials," pp. 39-62 in Extrusion in Ceramics, Engineering Materials and Processes. Edited by F. Händle. Springer-Verlag Berlin Heidenberg (2007).

[2]P. Bormans, Ceramics are more than clay alone, CISP, Cambridge International Science Publishing (2004).

[3]Brick Development Association, UK and Ireland, www.brick.org.uk/industry-sustainability.html

[4]Ch. Koroneos, A. Dompros, "Environmental assessment of brick production in Greece," Build. Envir., 42 2114-2123 (2007).

[5]W. C. Oliver, G. M. Pharr, “An improved technique for determining hardness and elastic modulus,” J. Mater. Res., 7 1564-1583 (1992).

[6]G. J. McLachlan, D. Peel, Finite Mixture Models, Wiley Series in Probability and Statistics, A Wiley-Interscience Publication (2000).

[7]K. J. Krakowiak, P. B. Lourenco, F. -J. Ulm, “Multi-technique Investigation of extruded clay brick microstructure,” J. Am. Ceram. Soc., accepted for publication (2011).

[8]G. W. Brindley, M. Nakahira, “The Kaolinite-Mullite reaction series: II, Metakaolin,” J. Am. Ceram. Soc., 42 314-318 (1959).

[9]G. W. Brindley, M. Nakahira, “The Kaolinite-Mullite reaction series: III, High-temperature phases,” J. Am. Ceram. Soc., 42 319-324 (1959).

[10]R. E. Grim, W. F. Bradley, “Investigation of the effect of heat on the clay minerals Illite and Montmorillonite,” J. Am. Ceram. Soc., 23 242-248 (1940).

[11]G. W. Brindley, S. Udagava, ”High-temperature reactions of clay mineral mixtures and their ceramic properties: I, Kaolinite-Mica-Quartz mixtures with 25 weight % Quartz,” J. Am. Ceram. Soc., 43 59-65 (1960).

[12]B. Sonuparlak, M. Sarikaya, I. Aksay, “Spinel phase formation during the 980°C exothermic reaction in Kaolinite-to-Mullite reaction series,” J. Am. Ceram. Soc., 70 837-842 (1987).

[13]C. J. McConville, W. E. Lee, “Microstructural development on firing illite and smectite clays compared with that in kaolinite,” J. Am. Ceram. Soc. 88 2267-2276 (2005).

[14]C. Rodriguez-Navarro, G. Cultrone, A. Sanchez-Navas, E. Sebastian, “TEM study of mullite growth after muscovite breakdown,” Am. Mineral. 88 713-724 (2003).

[15]R. E. Grim, W. F. Bradley, “Investigation of the effect of heat on the clay minerals Illite and Montmorillonite,” J. Am. Ceram. Soc. 23 242-248 (1940).

[16]H. Schneider, S. Komarneni (Eds), Mullite, 2nd edition, A Wiley-VCH Verlag GmbH & Co., KGaA (2005).

[17]Y. Iqbal, W. E. Lee, “Fired porcelain microstructures revisited,” J. Am. Ceram. Soc., 82 3584-90 (1999).

[18]O. Castelein, R. Guinebretière, J. P. Bonet, P. Blanchart, “Shape, size and compositon of mullite nanocrystals from rapidly sintered kaolin,” J. Eur. Ceram. Soc., 21 2369-2376 (2001).

[19]W. E. Lee, G. P. Souza, C. J. McConville, T. Tarvornpanich, Y. Iqbal, “Mullite formation in clays and clay-derived vitreous ceramics,” J. Eur. Ceram. Soc., 28 465-71 (2008).

[20]K. Devineau, B. Devouard, F. Villieras, F. Faure, J.-L. Devidal, A. Kohler, “Evolution of product phase assemblabes during thermal decomposition of muscovite under strong disequilibrium conditions,” Am. Mineral., 91 413-424 (2006).

[21]J. F. Schairer, N. L. Bowen, "Melting relations in the systems Na_2O-Al_2O_3-SiO_2 and K_2O-Al_2O_3-SiO_2," Am. J. Sci., 245 193-204 (1947).

[22]M. Miller, Ch. Bobko, M. Vandamme, F.-J. Ulm, "Surface roughness criteria for cement paste nanoindentation," Cem. Concr. Res., 38 467-476 (2008).

[23]ISO 25178, "Geometrical product specifications (GPS) – Surface texture: Areal".

[24]J. J. Vlassak, W. D. Nix, "Measuring the elastic properties of anisotropic materials by means of indentation experiment," J. Mech. Phys. Solids, 42 1223-1245 (1994).

[25]EMMIX code webpage, http://www.maths.uq.edu.au/~gjm/emmix/emmix.html.

[26]A. C. Fischer-Cripps, The IBIS handbook of nanoindentation, Fischer-Cripps Laboratories Pty. Limited, www.ibisonline.com.au (2009).

[27]A. Fischer-Cripps, "Nanoindentation," Springer Verlag, New York (2003).

[28]www.digitalsurf.fr

[29]M. W. Barsoum, Fundamentals of Ceramics, Series in Materials Science and Engineering, IoP (2003).

[30]A. F. Gualtieri, M. Zanni, "Quantitative determination of crystalline and amorphous phase in traditional ceramics by combined Rietveld-RIR method," Mat. Sci. Forum, 278-281 834-839 (1998).

[31]M. Dondi, M. Marsigli, I. Venturi, "Microstructure and mechanical propoerties of clay bricks: comparison between fast firing and traditional firing," Br. Ceram. Trans., 98 12-18 (1999).

[32]G. Cultrone, E. Sebastián, K. Elert, M. J. de la Torre, O. Cazalla, C. Rodriguez-Navarro, "Influence of mineralogy and firing temperature on the porosity of bricks," J. Eur. Ceram. Soc., 24 547-564 (2004).

[33]J. Martin-Marquez, A. G. De la Torre, M. A. G. Aranda, J. Ma Rincon, M. Romero, "Evolution with temperature of crystalline and amorphous phases in porcelain stoneware," J. Am. Ceram. Soc., 92 229-234 (2009).

[34]S. P. Chaudhuri, P. Sakar, "Constitution of porcelain before and after heat-treatment. I: Mineralogical composition," J. Eur. Ceram. Soc., 15 1031-1035 (1995).

[35]A. Hunger, G. Carl, A. Gebhart, Ch. Rüssel, "Young's moduli and microhardness of glass-ceramics in the system $MgO/Al_2O_3/TiO_2/ZrO_2/SiO_2$ containing quartz nanocrystals," Mater. Chem. Phys., 122 502-506 (2010).

[36]P. Wange, T. Höche, Ch. Rüssel, J. D. Schnapp, "Microstructure-property relationship in high-strength MgO-Al_2O_3-SiO_2-TiO_2 glass-ceramics," J. Non-Cryst. Solids, 298 137-145 (2002).

[37]E. Bernardo, J. Doyle, S. Hampshire, “Sintered feldspar glass-ceramics and glass-ceramic matrix composites,” Ceram. Int., 34 2037-2042 (2008).

[38]R. J. Hand, D. R. Tadjiev, “Mechanical properties of silicate glasses as a function of composition,” J. Non-Cryst. Solids, 356 2417-2423 (2010).

[39]S. Yoshida, J.-Ch. Sangleboeuf, T. Rouxel, “Quantitative evaluation of indentation-induced densification in glass,” J. Mater. Res., 20 3404-3412 (2005).

[40]V. P. Pukh, L. G. Baĭkova, M. F. Kireenko, L. V. Tikhonova, T. P. Kazannikova, A. B. Sinani, “Atomic structure and strength of inorganic glasses,” Phys. Solid State, 47 876-881 (2005).

[41]T. Rouxel, “Elastic properties of glasses: a multiscale approeach,” C. R. Mecanique, 334 743-753 (2006).

[42]L. Ainsworth, “The Diamond Pyramid Hardness of Glass in Relation to the Strength and Structure of Glass. Part I. An Investigation of the Diamond Pyramid Hardness Test Applied to Glass,” J. Soc. Glass Technol., 38 479-500 (1954).

[43]L. Ainsworth, “The Diamond Pyramid Hardness of Glass in Relation to the Strength and Structure of Glass. Part II. Silicate Glass,” J. Soc. Glass Technol., 38 479-500 (1954).

[44]M. Yamane, J. D. Mackenzie, “Vicker’s hardness of glass,” J. Non-Cryst. Solids, 15 153-164 (1974).

[45]A. Makishima, J. D. Mackenzie, “Calculation of bulk modulus,, shear modulus and Poisson’s ratio of glass,” J. Non-Cryst. Solids, 17 147-157 (1975).

[46]www.sciglass.info

[47]http://glassproperties.com/priven/

[48]A. Makishima, J. D. Mackenzie, “Direct calculation of Young’s modulus of glass,” J. Non-Cryst. Solids, 12 35-45 (1973).

[49]H. Schneider, J. Schreuer, B. Hildmann, “Structure and properties of mullite – A review,” J. Eur. Ceram. Soc., 28 329-344 (2008).

[50]J. Qu, M. Cherkaoui, Fundamentals of Micromechanics of Solids, John Wiley & Sons Inc. (2006).

[51]F. Hill, “Elastic properties of reinforced solids: some theoretical principles,” J. Mech. Phys. Solids 11 357-372 (1963).

[52]M. Ostoja – Starzewski, “Material spatial randomness: From statistical to representative volume element,” Probabilist. Eng. Mech. 21 112-132 (2006).

[53]J. G. Berryman, “Bounds and self-consistent estimates for elastic constants of random polycrystals with hexagonal, trigonal, and tetragonal symmetries,” J. Mech. Phys. Solids, 53 2141-2173 (2004).

[54]P. Heyliger, H. Ledbetter, S. Kim, “Elastic constants of natural quartz,” J. Acoust. Soc. Am., 114 644-50 (2003).

[55]W. J. Drugan, J. R. Willis, “A micromechanics-based nonlocal constitutive equation and estimates of representative volume element size for elastic composites,” J. Mech. Phys. Solids, 44 497-524 (1996).

[56]A. A. Gusev, “Representative volume element size for elastic composites: a numerical study,” J. Mech. Phys. Solids, 45 1449-1459 (1997).

[57]Z. F. Khisaeva, M. Ostoja – Starzewski, “On the size of RVE in finite elasticity of random composites,” J. Elasticity 86 153-173 (2006).

[58]G. Constantinides, K. S. R. Chandran, F. -J. Ulm, K. J. Van Vliet, “Grid indentation analysis of composite microstructure and mechanics: Principles and validation,” Mater. Sci. Eng. A-Struct. Mater. Properties Microstruct. Process., 430 189-202 (2006).

[59]F. -J. Ulm, M. Vandamme, H. M. Jennings, J. Vanzo, M. Bentivegna, K. J. Krakowiak, G. Constantinides, Ch. P. Bobko, K. J. Van Vliet, “Does microstructure matter for statistical nanoindentation techniques?,” Cem. Concr. Compos., 32 92-99 (2010).

VI. Conclusions and Future Perspectives

The development of sustainable and innovative masonry should motivate continuing research. This includes novel developments in the field of material science of basic constituents of masonry, which are fired clay brick as well as cement or lime mortars. In particular, the study of the microstructure-property relation is much relevant for the reliable prediction of the engineering properties. This thesis contributes to our understanding of the complex interplay between composition, material processing and fired clay brick microstructure by providing a systematic description of brick morphology as well as the mechanical performance at different material levels.

VI.1. SUMMARY OF MAIN FINDINGS AND OPEN QUESTIONS

The experimental approach followed in this work gives a detailed picture of the fired clay brick microstructure. The hierarchical ordering has been proved, which allows one to break down the masonry brick into three structural blocks with different morphological and mechanical fingerprints. Such blocks are linked to the composition of the raw materials and influenced to a great extent by the processing technology.

Conclusion 1: *The microstructure of the clay brick can be dissected into three material scales: Level "0" (<10^{-6} [m]), "Primary Brick" (<10^{-4} [m]) and "Secondary Brick" (<10^{-2} [m]). The level "0" represents the nanocomposite 'glassy' matrix developed for a temperature above the melting temperature of the raw materials, or the assembly of dehydroxylated, partially molten clay aggregates and initial melt if the processing temperature approaches the melting threshold. The 'glassy' matrix phase is of composite nature. It incorporates the neo-crystals of primary and secondary mullites, hematite and other minor phases in different forms, such as whiskers, of sub-micron scale hosted in the amorphous phase. The "Primary Brick" structure combines the lower scale block and inherent microporosity. It exhibits either a granular morphology or continuous matrix*

morphology with pore inclusions. The top level in the brick microstructure hierarchy is represented by the "Secondary Brick" block. It is composed of fractured coarse aggregates of sand, peripheral cracks at the interface of the coarse particles and the composite represented by "Primary Brick". Such a structure is described with anisotropic mechanical and physical behavior, whose origin is found in the manufacturing technology.

Several open questions persist. One of them is related to the prediction of the volumetric proportions of the mineral components incorporated within the proposed scheme. It appears that at the current state of knowledge the qualitative description of the phase transformation products is available only for pure kaolinite mineral. Such quantitative model is lacking for the mica group of minerals as well as for the mixture of kaolinite and mica minerals. Therefore, most of the available studies, which deal with the phase transformations of raw materials used in the production of structural clay products, represent only a qualitative approach to this problem. Alternatively, such studies refer to the phase diagrams, which may give the approximate weight fractions of the phase product, but only for limited cases of binary or ternary system of oxides. Another open problem refers to the homogenization scheme. An upscaling procedure, which is able to couple all the microstructural blocks indentified in this study, is required in order to transfer this knowledge to quantitative, reliable macroscopic behavior. Recent developments in the computational homogenization of stochastic media may provide an answer to this problem.

Conclusion 2: *The mechanical response of heterogeneous materials and its correlation with the local composition and morphology can be accurately assessed with Statistical Grid Indentation (SGI) methods. The depth-sensing tests offer a robust means to measure in-situ mechanical characteristics of the phase, which was created within unique chemical environment and cannot be recapitulated ex-situ in the bulk form. For heterogeneous materials with hierarchical ordering of microstructure a Buckle's rule applies as a first order approximation of the indentation depth, at which the measured phase properties may be considered intrinsic. Above this limit, the results of SGI method converge with increasing indentation depth towards the homogenized material response, via transient states which are scale and microstructure dependent. The bivariate deconvolution based on Maximum Likelihood concept and Expectation Maximization algorithm provides an accurate mean to infer the internal structure of the experimental data and the number of model components, and associate the records with the unique feature of the investigated microstructure. Such*

result is achieved due to implementation of data clustering according to the Bayes rule of allocation, which allows reproducing the local phase composition of the investigated region on pure probabilistic basis and measured mechanical response.

The results of SGI technique gathered in the experimental campaign reported in this thesis demonstrated the versatility and flexibility of the method, which can be easily extended to other types of composite materials. The method originally developed for cement based materials has been extended in this thesis and substantiated with theoretical support by considering the simplistic microstructures commonly adopted in the material science field. Future progress is foreseen with respect to the choice of the size of Region of Interest (ROI) over which the grid indentations are executed, and the total number of the nodal points in single grid measurements with respect to the level of material heterogeneity. Such a study seems to be valuable if the surface fractions of each phase incorporated within the investigated ROI are intended to be representative estimators of the volumetric fractions in the bulk. The problem of 'statistical noise', usually present in the outcome of SGI method, and its influence on the estimated properties and surface fractions of the phases should be also addressed in future refinements of the method.

Conclusion 3: *The 'glassy' matrix incorporated at Level "0" within the brick microstructure represents a continuous composite solid. Its main component is aluminosilicate glass, which hosts neo-crystal phases of higher stiffness and strength. In such a material system both mechanical properties, Young's modulus ≈91 [GPa] and Vickers hardness ≈9.5 [GPa], are enhanced to a level significantly above the properties of silica and aluminosilicate glasses with alkaline additions. The 'glassy' bond is described by a high level of compositional heterogeneity and structural disorder, which contributes to the large scatter of the experimentally measured properties.*

An attempt has been made to give a quantitative mechanical description of the primary constituent of fired clay brick microstructure, which originates at Level "0" and develops for a temperature above the melting temperature of the raw materials mixture. One of the important remaining problems is related to the quantification of the mechanical behavior of the matrix phase if the temperature of brick processing approaches the melting temperature, and the processing conditions are not sufficient for the clay minerals to transform into a continuous matrix of 'glassy' type. Such a question stays open and deserves a subsequent attempt to be

addressed. This aspect appears to be of primary importance for the preservation of cultural heritage constructed with fired clay brick masonry. Indeed, it is common to find a matrix composed of relicts of the clay aggregates and melt in fired brick applied in historical constructions.

VI.2. FUTURE PERSPECTIVES AND CONCLUDING REMARKS

The study presented here aims at the implementation of the material science paradigm and at the application of the recent developments in the experimental material science into the field of fired clay masonry. The chosen approach provided the necessary results to achieve the objectives postulated on the beginning of this thesis. The relation between the brick microstructure, its composition and processing conditions has been inferred. The refined statistical nanoindentation has been applied and validated on the heterogeneous materials, providing reliable quantitative measures of the mechanical performance of the 'glassy' bond, which is considered the main component of the building ceramics.

On 17th March 1989 the Civic Tower of Pavia collapsed, with no previous apparent damage or significant strength deterioration. The 60 [m] height bell tower collapsed, killing four people and provoking severe damage in local surrounding. This catastrophe has driven an attention of researchers to the time-dependent behavior of masonry, e.g. creep, as well as environmentally driven stiffness and strength deterioration. After this disaster, it became common practice to construct large scale masonry prisms in order to follow the strain evolution in time under applied constant load. A similar strategy applies for durability studies, in which the environmental load is applied on the sample, e.g. cyclic moisture and temperature variation, and the evolution of strain, strength or stiffness is assessed. Such measured 'properties' refer to the macro scale, leaving the fundamental explanation of creep origin or degradation mechanism unresolved. The methods and approach presented here provide great expectations for an insight into these problems. In fact the depth-indentation techniques give access to the creep properties. The intrinsic creep properties of each phase of clay brick or mortar may be assessed at small length and time scale, reducing significantly the testing effort required in the large scale specimens. In addition, the material deterioration or coupled phenomena may be traced at all scales.

The methods applied in this study are of general character and find their application in the studies on a broad spectrum of materials. However, the SGI method represents a unique and promising experimental approach to investigate the multi-physics phenomena at the smallest

accessible scales, nano-, and submicron scale. The fact that the nanoindentation method has been extended to heterogeneous materials driven by the need of exploration of cement based materials cannot be ignored. Since the first pioneering applications in the laboratories of the Massachusetts Institute of Technology, the versatility and reliability of these methods have been proved, providing relevant insight into the more refined structures of such materials. The author believes that such progress and advance may be also achieved in the field of structural clay products and will help to tailor this material to societal needs and environmental demands.

Appendix I: MatLab code – Checker Board Model (Chapter III)

```
function [ P, d, SPR ] = CheckerBoard3D( j,d,D,M )

%-------------------------------------------------------------------------
% Konrad J.Krakowiak 21.07.2010
%-------------------------------------------------------------------------
% CheckerBoard3D - function to calculate the discrete probability masses Pi
% distribution of the checkerboard idealized material model, for given
% partition scheme H with odd numbers of intervals (Chapter III)
%-------------------------------------------------------------------------
% Input parameters:
% j - even number of the checkers per edge
% d - size of the interaction volume
% M - odd division number of the discrete areas within the composite zone
%     M=m-2, where m stands for the total number of the intervals within
%     the discrete partition H
% D - the size of the single checker
%-------------------------------------------------------------------------

VTOT=(j*D-d).^3;        % Volume available for probing with interaction
                        % volume of characteristic size d

V1=0.5*(j^3)*(D-d).^3;  % Volume which represents Phase 1, V2=V1, c1=c2=0.5

%*************************************************************************
%Calculation of the discrete volumes VI(III.6b), VII(III.7b), VIII(III.8)
%*************************************************************************

% Definition of the vectors VI, VII, VIII and the sub-volumes Qi(III.6a) as
% well as sub-areas Si (III.7a)
```

```
VI=zeros(1,(M+3)/2);
VII=zeros(1,(M+3)/2);
VIII=zeros(1,(M+3)/2);


Q=zeros(1,(M+3)/2);
Q(1)=0;
Q((M+3)/2)=(d/2)^3;


S=zeros(1,(M+3)/2);
S(1)=0;
S((M+3)/2)=(d/2)^2;


% Calculation of the sub-volumes Qi and sub-areas Si (integration):

for i=2:((M+1)/2)

    Q(i)=quadgk(@(x)CheckerIntegralVolume(x,(i-1)/M,d),0,(i-1)*d/M);
    F=@(x)d*(((i-1)/M)*d-x)./(d-2*x);
    S(i)=quad(F,0,(i-1)*d/M);

end

% Definition of the multiplication factors NI, NII and NIII. NI-the number
% of corner points common for 8 checkers, NII-the number of edges common
% for 4 checkers, and NIII-the number of faces common for 2 checkers

NI=(j-1)^3;
NII=3*j*((j-1)^2);
NIII=3*(j^2)*(j-1);

% Calculation of the VI, VII and VIII:

for i=1:((M+1)/2)

    VI(i+1)=8*NI*(Q(i+1)-Q(i));
    VII(i+1)=4*NII*(D-d)*(S(i+1)-S(i));
```

```
    if i<((M+1)/2)                      % see Figure III.6(a)
    VIII(i+1)=2*NIII*(d/M)*((D-d)^2);

    else
    VIII(i+1)=NIII*(d/M)*((D-d)^2);     % see Figure III.6(a)

    end

%************************************************************************
%Calculation of the global vector of discrete volumes Vi, which corresponds
%to the assumed partition scheme H
%************************************************************************

VOL=[V1 0.5.*(VI(2:(M+1)/2)+VII(2:(M+1)/2)+VIII(2:(M+1)/2))...
     (VI((M+3)/2)+VII((M+3)/2)+VIII((M+3)/2))];

% Symmetry Condition (Vi=Vm+1-i)

counter=1;
for j=(M+2):-1:(M+3)/2
    VOL(j)=VOL(counter);
    counter=counter+1;
end

%************************************************************************
%Calculation of the vector of probability masses Pi for given partition H
%************************************************************************

P=VOL/VTOT;
P=P';

%************************************************************************
% Verification
%************************************************************************

SPR=VTOT-sum(VOL);

%************************************************************************

end
```

```
function z=CheckerIntegralVolume(x,a,d)
%-------------------------------------------------------------------------
% Konrad J.Krakowiak 21.07.2010
%-------------------------------------------------------------------------
% CheckerChackerInegralVolume - function to evaluate numerically integral
% Eq. III.6(a)
%-------------------------------------------------------------------------

n=length(x);
z=zeros(size(x));

for j=1:n

% Limits of integration for the second variable (Xi2)

y1=0;
y2=d*(a*d-x(j))/(d-2*x(j));

%*************************************************************************
% Function z=f(x,y) expressed in the modified coordinate system Eq. III.2b
%*************************************************************************

A1=(d^2)*x(j);
A2=2*d*x(j);
A3=4*x(j);

h=@(y)((-a*d^3)+A1+(d^2)*y-A2*y)./(A2+2*d*y-A3*y-d^2);

% Integration with adaptive Simpson quadrature

z(j)=quad(h,y1,y2);

end
```

Appendix II: MatLab code – Homogenization (Separation of Scales) (Chapter III, Figure III.17(a))

```
function [ Eeff ] = ScaleEffect(X2,X3,X4,X5 )
%-------------------------------------------------------------------------
% Konrad J.Krakowiak 21.07.2010
%-------------------------------------------------------------------------
% ScaleEffect - function used to follow the homogenization or separation of
% of scales for biphasic materials, fiber board model, effective modulus
% follows the law of mixtures (Figure III.17(a))
%-------------------------------------------------------------------------
%Input Parameters:
% X2 - number of the fiber cells                (j)
% X3 - size of the unit cell                    (Dc)
% X4 - diameter of the fiber                    (Df)
% X5 - size of the observation window           (d)

% Create the fiber board jxj

CENTERSF=gridtop(X2,X2);
XCG=CENTERSF(1,:)*X3+X3/2;    % Equally Spaced Centers
YCG=CENTERSF(2,:)*X3+X3/2;    % Equally Spaced Centers

% Construct the observation window

WXB=[0  0 X2*X3 X2*X3 0];       % Board of size X2*X3
WYB=[0 X2*X3 X2*X3 0 0];         % Board of size X2*X3

% Choose randomly the center of the observation window

a=0.5*X5;
b=X2*X3-0.5*X5;
```

```
OXW = a+(b-a).*rand(1,1);
OYW = a+(b-a).*rand(1,1);

% Construct the observation window

WX=[OXW-0.5*X5  OXW-0.5*X5 OXW+0.5*X5 OXW+0.5*X5]; % Rectangle of size X5
WY=[OYW-0.5*X5  OYW+0.5*X5 OYW+0.5*X5 OYW-0.5*X5]; % Rectangle of size X5

% Draw the board and the fibers

for i=1:size(XCG,2)
    t=0:0.01:2*pi;
    XF{i}=0.5*X4*cos(t)+XCG(i);  % X coord. of the fiber locus
    YF{i}=-0.5*X4*sin(t)+YCG(i); % X coord. of the fiber locus
end

%--------------------------------------------------------------------------
% Graphics module
%--------------------------------------------------------------------------

    figure(1)
    set(gcf,'Color','w')
    axis off
    hold on
        for k=1:size(XF,2)
            plot(XF{k},YF{k})              % plot the fibers on the board
        end
    axis equal
    patch(WX,WY,[1 1 1 1],'FaceAlpha',0.6) % plot the observation window
    plot(WXB,WYB)                          % plot the outline of the board

%--------------------------------------------------------------------------

% Module to enhance the calculation of the intersection areas of the fibers
% with the interaction window of size d

% Consider only these fibers which are in close proximity to the center of
% the interaction window [OXW,OYW], limit is set for three times the actual
% size of the interaction window 3X3

counter=1;
```

```
for i=1:size(XCG,2)
    if XCG(i)>=(OXW-0.5*X5-3*X3) & XCG(i)<=(OXW+0.5*X5+3*X3)
        XC1(counter)=XCG(i);
        YC1(counter)=YCG(i);
        counter=counter+1;
    end
end

counter=1;
for i=1:size(XC1,2)
    if YC1(i)>=(OYW-0.5*X5-3*X3) & YC1(i)<=(OYW+0.5*X5+3*X3)
        XC(counter)=XC1(i);
        YC(counter)=YC1(i);
        counter=counter+1;
    end
end

% Define the boundaries of the fibers which are left after the filtering
% procedure above

for i=1:size(XC,2)
    t=0:0.01:2*pi;
    XF1{i}=0.5*X4*cos(t)+XC(i);  % X coord. of the fiber locus
    YF1{i}=-0.5*X4*sin(t)+YC(i); % X coord. of the fiber locus
end

% Calculate the area of the intersections

for j=1:size(XC,2)

    [XI,YI]=polybool('intersection',WX,WY,XF1{j},YF1{j});    % calc.overlap
    INTAREA(j)=polyarea(XI,YI);

%--------------------------------------------------------------------------
% Graphics Module
%--------------------------------------------------------------------------

% Add Intersection Regions to the graphics

    [fI, vI] = poly2fv(XI,YI);
    patch('Faces', fI, 'Vertices', vI, 'FaceColor',[0.9,0.2,0.4],...
```

```
       'EdgeColor', 'none');

%-------------------------------------------------------------------------

end

% Define the mechanical properties of the fiber Ef and matrix phase Em

Ef=260;
Em=120;

% Calculate the actual surface fraction of fiber material within the
% interaction window

cf=sum(INTAREA)/(X5^2);

% Calculate the effective modulus (Voigt)

Eeff=Ef*cf+Em*(1-cf);


end
```